RICE UNIVERSITY

Carbon nanotube conditioning: ab initio simulations of the effect of interwall interaction, defects and doping on the electronic properties of carbon nanotubes.

by

Matias Soto Castillo

A THESIS SUBMITTED
IN PARTIAL FULFILLMENT OF THE
REQUIREMENTS FOR THE DEGREE

Doctor of Philosophy

APPROVED, THESIS COMMITTEE

Dr. Enrique V. Barrera, Chair
Professor of Materials Science and NanoEngineering

Dr. Walter G. Chapman
William W. Akers Professor of Chemical and Biomolecular Engineering, Associate Dean for Energy, George R. Brown School of Engineering

Dr. Rouzbeh Shahsavari
Assistance Professor of Civil and Environmental Engineering

Dr. Robert Vajtai
Senior Faculty Fellow, Materials Science and NanoEngineering

HOUSTON, TEXAS
May 2017

ABSTRACT

Carbon nanotube conditioning: ab initio simulations of the effect of interwall interaction, defects and doping on the electronic properties of carbon nanotubes.

by

Matias Soto Castillo

Using carbon nanotubes for electrical conduction applications at the macroscale has been shown to be a difficult task for some time now, mainly, due to defects and impurities present, and lack of uniform electronic properties in synthesized carbon nanotube bundles. Some researchers have suggested that growing only metallic armchair nanotubes and arranging them with an ideal contact length could lead to the ultimate electrical conductivity; however, such recipe presents too high of a cost to pay at the present time. A different route is to learn to manage the defects, impurities, and the electronic properties of carbon nanotubes present in bundles grown by current state-of-the-art reactors, so that the electrical conduction of a bundle or even wire may be enhanced. In our work, we have used first-principles density functional theory calculations to study the effect of interwall interaction, defects and doping on the electronic structure of metallic, semi-metal and semiconducting single- and double-walled carbon nanotubes in order to gain a clear picture of their properties. The electronic band gap for a range of zigzag single-walled carbon nanotubes with chiral indices (5,0) – (30,0) was obtained. Their properties were used as a stepping stone in the study of the interwall interaction in double-walled carbon nanotubes, from which it was found that the electronic band gap depends on the chirality of the inner and outer tubes, average diameter, and interwall distance. The effect of vacancy defects was also studied for a range of single-walled carbon nanotubes. It was found that the electronic band gap is reduced for the entire range of zigzag carbon nanotubes, even at vacancy defects concentrations of less than 1%. Finally, interaction potentials obtained via first-principles calculations were generalized by developing mathematical models for the purpose of running molecular dynamics simulations of the adsorption doping of diatomic iodine. An ideal adsorption site was found using a stochastic approach and with an adsorption energy higher than other values in the literature. It was also found that the interaction with other iodine molecules leads to stronger adsorption energies.

Acknowledgments

I would like to dedicate this thesis work to the Author of all knowledge, the Creator of the Universe, the Sustainer of all things, and the Reason of all things; to the Almighty God.

The support and guidance provided by my advisor, Dr. Enrique V. Barrera from Rice University must also be acknowledged. I thank him for the many conversations and meetings that helped me steer my thesis work in the right direction.

Also, I would like to thank all of the thesis defense committee members and acknowledge their contribution to this work: Dr. Walter G. Chapman, Dr. Rouzbeh Shahsavari, and Dr. Robert Vajtai.

A couple of postdoctoral researchers that guided a portion of my work as part of our research group and that should be acknowledge are Dr. Santoshkumar Biradar and Dr. Liehui Ge.

The financial support provided by different agencies is also acknowledged: this work was partially funded by the Department of Energy's Research Partnership to Secure Energy for America (RPSEA) Project no. ES014625; partial funding was also received from CONACyT Scholarship 314419 from the Mexican Federal Government and the State of Nuevo León (I^2T^2); computational resources were partially provided by the Data Analysis and Visualization Cyberinfrastructure funded by NSF under grant OCI-095909.

Finally, I must mention the role that my family has played throughout the years and that has culminated in the achievement of this thesis work. I thank my parents for instilling in me a desire to excel in all the things I do and to put God in first place at all times. I thank my sisters and brother-in-law for supporting me and providing financial help when needed throughout the many years I have been in school. And finally I thank my wife for being a true companion and partner during my doctoral studies. They all truly deserve my full acknowledgement of their invaluable contribution to my life.

Table of Contents

List of Figures

List of Tables

Nomenclature

CNT	Carbon Nanotube
SWCNT	Single-Walled Carbon Nanotube
DWCNT	Double-Walled Carbon Nanotube
MWCNT	Multi-Walled Carbon Nanotube
DFT	Density Functional Theory
LDA	Local Density Approximation
GGA	Generalized Gradient Approximation
vdW	van der Waals
vdW-DF	van der Waals Density Functional
MD	Molecular Dynamics
SIESTA	Spanish Initiative for Electronic Simulations with Thousands of Atoms
LAMMPS	Large-scale Atomic/Molecular Massively Parallel Simulator
TB	Tight Binding
PAO	Primitive Atomic Orbital
DOS	Density of States
PBC	Periodic Boundary Conditions
FDF	Flexible Data Format
LJ	Lennard-Jones

Chapter 1

Electronic Structure of Single-Walled Carbon Nanotubes

1.1 Introduction

Since their discovery [1] carbon nanotubes (CNTs) have attracted a lot of attention because of their intrinsic mechanical, thermal, and electrical properties, making them suitable for interesting applications such as transistors [2], storage devices and field emission [3], and nanoscale machines [4]. In particular, double-walled carbon nanotubes (DWCNTs) possess interesting properties. They behave somewhat like single-walled carbon nanotubes (SWCNTs) in their physical properties, but are more sturdy mechanically [5], meaning that they are expected to have higher values of mechanical stiffness and tensile strength, and exhibit higher chemical and thermal stability than SWCNTs (under inert conditions, they can survive 2000 ^{o}C without reaction) [3], making them good candidates for macroscopic carbon nanotubes fibers, similar to those made with SWCNTs [6]. Also, DWCNTs are the simplest example of multi-walled carbon nanotubes (MWCNTs), providing the ideal model for studying the influence of interlayer interaction on the physical properties of nanotube systems [3].

1.1.1 Structure of Carbon Nanotubes

Carbon nanotubes have been grouped into three main categories: armchair, zigzag, and chiral (Figure 1). These three types of CNTs appear from the direction of the rolling vector of the graphene sheet. Figure 2 shows that if the graphene layer is rolled along the x-direction the CNT is categorized as armchair; if instead the graphene layer is rolled along the direction of the a_1 vector then the CNT is considered zigzag; finally, if the graphene layer is rolled along a direction other than the two previously mentioned, then the CNT is categorized as chiral.

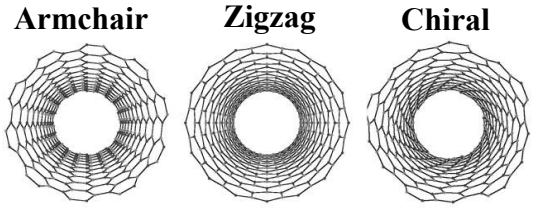

Figure 1. Three types of SWCNTs [7].

1.1.2 Electrical Properties of Carbon Nanotubes

The electrical properties of SWCNTs have been predicted to depend on the direction of the chiral vector, as characterized by the chiral index (n, m). From theoretical calculations reported in [8–11], all armchair SWCNTs (n, n) are considered metallic, zigzag SWCNTs (n, 0) have two types of behavior: metallic when $n = 3k$, k being an integer, and semiconducting otherwise, and chiral SWCNTs (n, m) also have two distinct types of behavior: metallic properties when $(2n + m) = 3k$, and semiconducting otherwise.

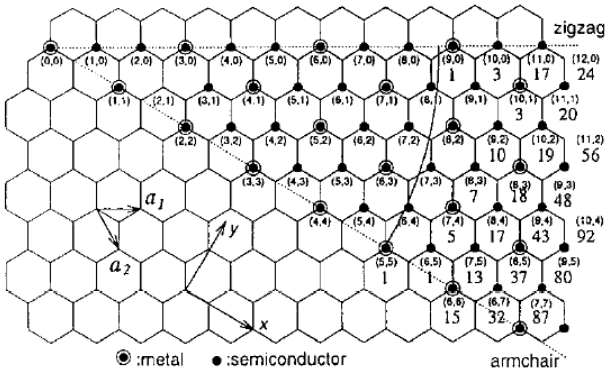

Figure 2. Graphene layer with directions of carbon nanotube classification [9].

However, tight-binding (TB) calculations by Hamada *et al.* [12] and both tight-binding and density functional theory (DFT) calculations using the local density approximation (LDA) by Blase *et al.* [13] of small radius zigzag SWCNTs show a small band gap at the Γ point for tubes originally considered metallic, such as the (9, 0). Other cases are shown in Table 1, from which it can be seen that zigzag CNTs with chiral index $n = 3k$, k being an integer, do show a small band gap at the Γ point, which reduces with increasing tube diameter. This band gap can be attributed to the effect of curvature, and in the case of DFT-LDA calculations, the inclusion of orbital hybridization in the model for the calculations of the electronic structure of SWCNTs has a significant impact on the resulting predictions for small radius tubes [13].

Table 1. Band gaps of zigzag CNTs with chiral index *n = 3r, r* being an integer. Units of eV.

SWCNT	TB [12]	TB [13]	DFT-LDA [13]	DFT-LDA [14]	DFT-LDA [15]
(9,0)	0.04	0.07	0.17	0.096	
(12,0)				0.04	
(15,0)				0.023	0.08
(18,0)				0.013	0.04

1.1.3 Outline of Dissertation

Using carbon nanotubes for electrical conduction applications at the macroscale has been shown to be a difficult task for some time now, mainly, due to defects and impurities present, and lack of uniform electronic properties in synthesized carbon nanotube bundles. Some researchers have suggested that reaching ultimate conductivity may require the synthesis of all-armchair SWNTs, a consistent synthesis of large quantities (gram amounts or higher) of defect-free CNTs with control on length, diameter, and chirality [16]; and at the microscopic level, fine manipulation must be performed so that every junction of armchair CNTs possesses the optimal length, then the whole fiber could achieve the conductivity as high as that of a single CNT [17]; yet the author of the latter reference acknowledges the impossibility of doing so for millions of junctions as suggest that being able to synthesize mostly metallic armchair CNTs would be the solution to increase the electrical conductivity of a CNT bundle or wire. Even though both of these solutions present a possible methodology to increase the conductivity of CNT wires, and despite recent efforts to synthesize all-armchair CNTs [18], a different approach may be used to improve the electrical properties of carbon nanotubes.

The concept of carbon nanotube conditioning comes from the experience in the world of materials engineering. Over the last one hundred years or so, materials engineering has evolved significantly, and one of the lessons learned is that imperfections in the materials structure can actually be used to modify the properties of the material. Taking such experience from materials engineering, we have identified some conditioning factors that could modify some of the properties of carbon nanotubes.

The electronic properties of double-walled carbon nanotubes and the effect of interwall interaction on such properties has been studied previously [15,19–21]. Based on these previous reports, we made the assumption that some relationships may be found that explain the effect of interwall interaction as a function of the atomic structure of the CNT molecules or other parameters.

Adding vacancy defects to the structure of carbon nanotubes to study their effect has also been reported previously [22–24]. These reports show how vacancies affect the electronic properties of some cases of armchair and zigzag carbon nanotubes. Based on them, we also made the assumption that using vacancy defects on different types of carbon nanotubes could help modify their properties and endeavor to study such effects for an entire range of SWCNTs and one case of DWCNT.

Finally, adsorption doping has been another conditioning aspect that has been studied both experimentally [25–28] and theoretically [29,30]. Experimentally, promising results have been obtained that show iodine as a good candidate to modify the electrical properties of carbon nanotubes. However, theoretical studies have fallen short in providing a better understanding in the physical phenomena that underlies the effect of iodine doping on the electrical properties of carbon nanotubes. Our assumption in regards to iodine doping was that it can be used to modify some of the properties of carbon nanotubes.

Overall, this study has gathered data using ab initio density functional theory and molecular dynamics simulations of the electronic structure and electronic band gap, the total energy of structurally-relaxed molecules (e.g. SWCNTs, DWCNTs, etc.), the relaxed structure (energy minimization) of molecules or configuration of interacting systems, and even the electronic charge transfer. Using this data, we discuss how the different conditioning aspects mentioned modify the electronic band gap of carbon nanotubes, the atomic structure, and the configuration of interacting systems. Based on this, some conclusions have been made as to the effect of interwall interaction, defects and doping on the electronic structure of carbon nanotubes.

1.2 Methodology

The SWCNT configurations studied were armchair with chiral indices between (3,3) and (15,15), and zigzag tubes with chiral indices between (5,0) and (30,0). The range of diameters for the armchair and zigzag nanotubes is 0.41-2.04 nm and 0.40-2.35 nm, respectively. According to experimental observations and literature regarding the structure of carbon nanotubes, the minimum and maximum diameters of SWCNTs exhibited are 0.4 nm and 2.0 nm, respectively [31–33]. The study of zigzag CNTs was extended to diameters larger than experimentally observed because some interesting electrical properties needed to be understood more clearly for the regions of large-diameter zigzag carbon nanotubes. Chiral CNTs were not included in our current study due to the need of having a small unit cell with translational symmetry for the density functional theory code to run efficiently. Recently, the group of Susumu Saito developed a method based on the helical symmetry and real-space DFT method to calculate the energies and electronic band structure of chiral CNTs [34]. Future work includes the study of chiral carbon nanotubes following the method of Kato *et al.* [34].

The computational calculations were carried out using the SIESTA method and software [35], which makes use of density functional theory [36] under the Kohn-Sham auxiliary system [37]. The SWCNTs were modeled as a single unit cell inside a supercell. The carbon-carbon distance used to generate the geometry is that of graphite hexagonal lattice, 1.42 Å [9]. An example of a zigzag and armchair unit cell is shown in the figure below. Figure 3a shows the unit cell of a (10,0) zigzag CNT, and Figure 3b shows the unit cell of a (6,6) armchair CNT. The lattice vector along the tube axis was set for one unit cell as 4.26 Å and 2.46 Å for zigzag and armchair CNTs, respectively. The length of the lattice vectors in the CNT radial directions were found from convergence studies that looked to minimize the interaction of the infinitely-long SWCNT with its images in adjacent supercells, while at the same time maintaining computational efficiency.

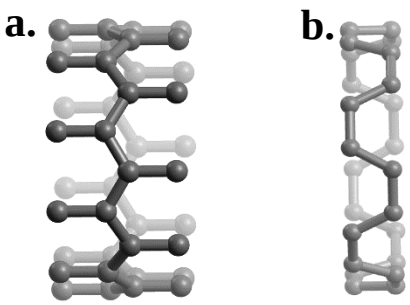

Figure 3. Example of a unit cell used for DFT simulations of a) zigzag and a b) armchair CNT.

Atomic orbitals for carbon atoms were defined by a localized basis set using a double-zeta basis using the split-valence scheme, which allows the electron density to adjust its spatial extent appropriately, in contrast with a minimal or single-zeta basis which is fixed. The cutoff radii for orbital confinement was set by the PAO.EnergyShift parameter in the SIESTA code[38]. This parameter was found to converge at a value of 0.005 Ry and chosen as 0.05 eV in order to compare with the calculations by Reich et al.[39].

Local density approximation, Ceperley-Alder flavor, was chosen for exchange-correlation potential, which allows us to compare the results of our calculations against other works that have used DFT-LDA either with plane-wave or localized basis set approximations for the atomic orbitals. Recently developed approximation such as van der Waals-corrected density functionals (vdW-DF) [40] or the Grimme method[41] may be employed in future work to assess the effect of long-range dispersion forces in the band gap calculations for SWCNTs.

The pseudopotential used for the Carbon atom was constructed according to the Troullier-Martins scheme, grouping core electrons into one orbital and allowing for four orbitals for the valence electrons of carbon atoms (2s, 2p, 3d, 4f). The file was obtained from the SIESTA pseudopotential database [42] and tested for energies and eigenvalues variation in different orbital configurations. Energy bands were calculated by taking 20 points from the Γ to the X point. The static configuration of each armchair and zigzag CNT was relaxed using a maximum force criterion of 0.04 eV/Å.

The convergence studies were carried out by varying a certain parameter and calculating the free energy per atom and electronic band gap at each parameter variation. The free

energy per atom and electronic band gap were compared to the final value for each change in the parameter. The convergence criteria was set as a difference of ≤ 1 meV/atom in free energy and ≤ 5 meV in band gap with respect to the final value. A list of converged parameters and the final value used for comparison is shown in the table below.

A larger SWCNT, (24,0) zigzag, was also used for convergence studies in order to test the size dependency of the parameters. It is important to note that the lattice vectors for the two directions perpendicular to the tube axis converged for a value that provided about 10 Å of empty space on each side of the nanotube. This fact was adopted as the convergence criteria for SWCNTs and later for DWCNTs of all sizes. The kgrid parameter was also found to be dependent on the nanotube diameter size. The range of appropriate values is listed in Table 2.

Different basis sets were tested to find the appropriate set of parameters to define it. The SIESTA basis set database [43] has three different files available for the carbon element. It was found that the electronic band gap of (7,0) SWCNT varies significantly within the values obtained using the three basis set from the database (between 1.11 and 0.50 eV), and it comparison to previous works [13–15]. Additionally, using the default values in SIESTA for the basis set of carbon atom a band gap of 0.52 eV was obtained for the (7,0) CNT. Testing the basis sets from the database and the default configuration in SIESTA on all the other CNTs in order to assess their behavior would require a lot of effort and time. Instead, our basis set was modeled after the work by Reich *et al.* [39], which was done in collaboration with one of the developers of the SIESTA code, P. Ordejón [35,44]. A double-zeta setting was chosen for the number of orbitals per atom. The rule of thumb for the energy shift (also known as the ΔE_{PAO}) is approximately 100 meV, but in our work, the PAO.EnergyShift parameter was converged with a criteria of ≤ 10 meV/atom in free energy and ≤ 5 meV in electronic band gap to a value of 68 meV. A more precise value of 50 meV was chosen, following the work of Reich *et al.* [39]. Using this value, an electronic band gap of 0.21 eV was obtained, which is in closer agreement to previous works [13–15].

A sample input file, known as a Flexible Data Format (FDF) file, is shown in Appendix A. This sample FDF file is for the energy minimization using SIESTA of a zigzag (8,0) SWCNT with one unit cell, at is named *filename.fdf*. For more information regarding the

specific keywords used in the FDF file, please refer to the SIESTA 3.2 manual [38]. The coordinate of all the single-walled carbon nanotubes were generated using a program called *Nanotube Modeler* [45]. As seen on Appendix A, the band structure was also obtained using the SIESTA calculations. After the system minimized the energies and the atomic forces were all below the chosen threshold (Table 2), SIESTA generated a file with all the band structure data, named *filename.bands*. A utility that is part of the SIESTA packaging converts this file to a data file readable by *gnuplot* [46]. Once converted, the band structure is plot for a range in energies using *gnuplot*. In our case, the Fermi energy was subtracted from all the energies when plotting the band structure.

Table 2. Converged parameters used in the DFT simulations of SWCNTs.

Parameter	Converged Value	Final Value
PAO.EnergyShift	50 meV	0.00005 Ry
kgrid	1,1,25 – 1,1,40	1,1,50
MD.MaxForceTol	40 meV/Å	1 meV/Å
MeshCutoff	300 Ry	1000 Ry
Electronic Temperature	300 K	50 K
DM.Tolerance	$1x10^{-4}$	$1x10^{-6}$
LatticeConstant	25.5 – 40.3 Å	About 10 Å larger

1.3 Results and Discussion

In order to validate our methodology, the first step is to check if our results are in agreement with previous literature and theory. To that effect, the difference in energy per atom with respect to a graphene sheet was calculated and shown in Figure 4. The difference in energy goes to zero as the SWCNT diameter increases, because the curvature of the carbon nanotube decreases. This is consistent according to [47]; in this discussion they commented that the total energy of nanotubes is higher than that of a flat graphene sheet due to a bond-bending energy loss.

The parameters shown in Table 2 were converged following the procedure mentioned in the previous section; however, some of them were modified in order to match those used in a previous report [39] of the electronic structure calculations of carbon nanotubes using SIESTA code package. The results obtained by Reich et al. using numerical atomic orbitals, as it is done in the SIESTA code package, were compared to results obtained using other codes that make use of plane waves in order to describe the valence electrons in the electronic configuration of each element. We have confidence in their results, and have chosen to compare to the band structure they calculated for the (10,0) single-walled carbon nanotube (Figure 5). As seen in the figure below, the main signatures of the band structure are replicated by our results when compared to those by Reich et al. [39]; the band gap also shown also seems to be in agreement between the two band structures.

Also, the electronic band structure was obtained from the Γ to X point, as noted in the diagram in Figure 6. The electronic band gap was calculated at the Γ point from the electronic structure of each SWCNT by taking the difference in energy between the lowest point of the conduction band and the highest point of the valence band. As a reference, the band structure of all the other SWCNTs are shown in Appendix B. The plot of the electronic band gap as a function of chiral index is shown in Figure 7, from which it can be observed that our results are consistent with previous DFT calculations that used the local density approximation [13–15,47–49], yet fall below the experimental values [50]. It is important to mention the fact that DFT-LDA underestimates the absolute values of the band gap of SWCNTs when compared to other approaches and experimental measurements [51–53]. This can already be observed in Figure 7. Additionally to this, using DFT-LDA

approach, Zólyomi *et al.* [14] have found an unphysical dependence of the band gap on the diameter of zigzag SWCNTs with (3k,0) indices, where k is a positive integer. They found that the band gaps of such DWCNTs follow the function $\Delta = C_2/d^2 + C_4/d^4$ with a C_4 factor larger than experimental value. The overestimation of this factor may be due to the lack of many-electron corrections in the DFT calculations, and it affects the band gap calculations of DWCNTs containing a (3k,0) nanotube.

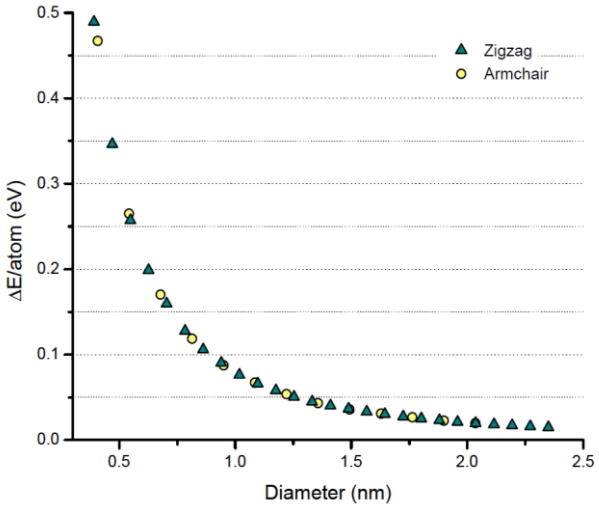

Figure 4. Difference in energy/atom with respect to a graphene sheet for zigzag and armchair SWCNTs.

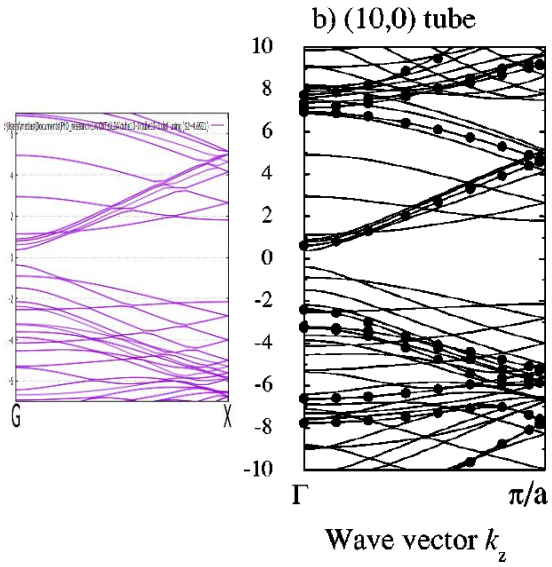

Figure 5. Band structure of the (10,0) zigzag SWCNT calculated by a) the methodology outlined in the previous section and b) by Reich *et al.* [39].

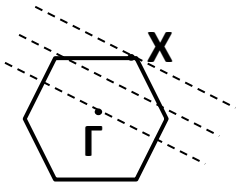

Figure 6. Diagram of the path used for band structure calculations.

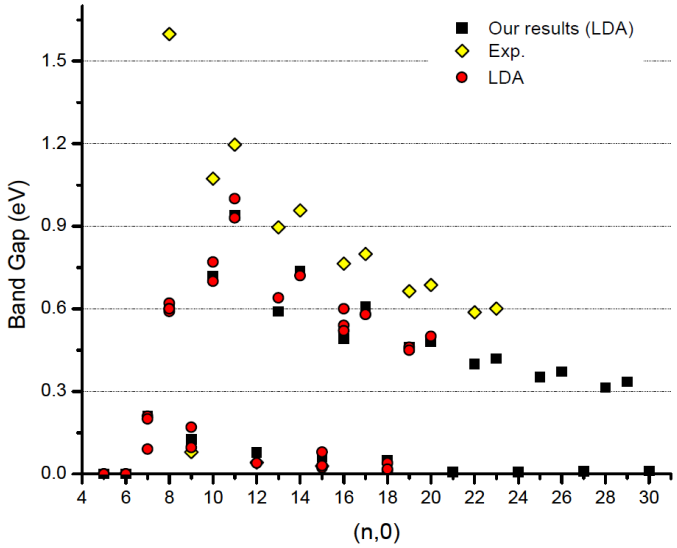

Figure 7. Band gap as a function of chiral index for our calculations and compared to other DFT-LDA calculations and experimental measurements found in the literature.

Further comparing our results to other works that used the generalized gradient approximation (GGA) [54–56] and other hybrid schemes (GGA+HF) [56–58], we see (Figure 8) that LDA underestimates the band gap calculations with respect to experimental measurements [50] and hybrid exchange-correlation functionals, as has been reported before [51–53]. However, we are able to observe a close relation to band gap calculations obtained using GGA functionals.

Although some hybrid functionals provide results which are closer to the experimental values, it's not entirely clear they will also give a smaller error than LDA when calculating the electronic structure of CNTs doped with other chemical elements. Because LDA provides a basic assessment of the properties of materials using DFT, we will use LDA functionals throughout this thesis work in order to obtain a basic understanding of the trends and general effects caused by interwall interaction, vacancy defects, and iodine doping.

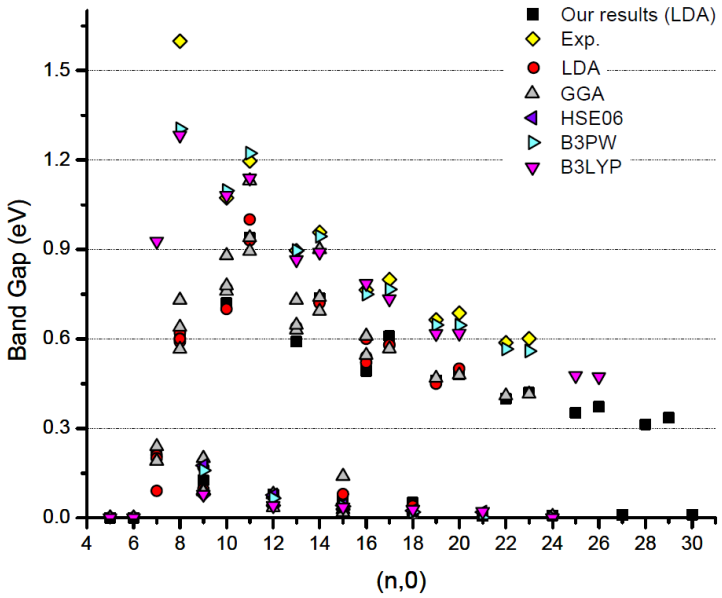

Figure 8. Comparison of our band gap calculations with other exchange-correlation functionals and experimental measurements found in the literature.

We may summarize the results obtained according to the chiral index of each zigzag CNT and the average band gap (Table 3). According to zone-folding, SWCNTs with a chiral index $n = 3k$ (k being an integer) should have zero band gap; per our DFT-LDA calculations this average band gap results in 0.039 eV, which is still higher than the energy due to room temperature (0.026 eV), so that these SWCNTs remain narrow band gap semiconductors even at room temperature. For both cases of SWCNTs with chiral indices $n = 3k+1$ and $n = 3k+2$, the prediction from zone-folding approximation is also confirmed by our DFT-LDA calculations, which show that both type of zigzag SWCNTs are semiconductors with an average band gap of 0.44 and 0.50 eV, respectively.

Table 3. Summary of average band gaps according to the chiral index.

Chiral index (n,0)	Zone-folding (ZF)	DFT-LDA, average band gap (eV)
n = 3k	Metallic	0.039
n = 3k+1	Semiconductor	0.44
n = 3k+2	Semiconductor	0.50

If instead the band gaps are grouped according to their diameter and sectioned in groups, the average band gap for each diameter range can be calculate to summarize its behavior. According to the table below, the larger SWCNTs have the smallest average band gaps overall, which increases as the diameter decreases, except for the smallest diameter range (0.4-1.0 nm). If the (5,0) and (6,0) SWCNTs are excluded from the averaging then the average band gap for the diameter range of 0.4-1.0 nm is 0.45, and the trend remains for the entire diameter range.

Table 4. Summary of average band gaps according to the SWCNT diameter.

Diameter (nm)	Average band gap (eV)	Average band gap (eV)
0.4-1.0 nm	0.34	0.45 (ignoring (5,0),(6,0) CNTs)
1.0-1.5 nm	0.43	
1.5-2.0 nm	0.28	
2.0-2.5 nm	0.21	
OVERALL	0.32	

1.4 Conclusions

The methodology used for the simulation of the electronic properties of armchair and zigzag carbon nanotubes within the local density approximation (LDA) agrees well with previous DFT-LDA results. The calculated values of energy per atom of both armchair and zigzag CNTs approaches that of a graphene layer as the CNT diameter increases, which agrees with previous reports. It was confirmed that the electronic band gap at the Γ point, calculated using DFT-LDA, underestimates the values obtained with experimental measurements and hybrid exchange-correlation functionals calculations for the zigzag CNTs with chiral indices $n = 3r+1$ and $n = 3r+2$ (r being an integer). For the zigzag CNTs with chiral indices $n = 3r$, there is much closer agreement between our results and experimental measurements or DFT calculations using hybrid functionals. We were able to extend our study to zigzag nanotubes of large diameter up to a (30,0) CNT. Those additional data points confirm the trends previously identified for the three groups of zigzag single-walled carbon nanotubes.

Chapter 2

Effect of Interwall Interaction on the Electronic Properties of Carbon Nanotubes

2.1 Introduction

Theoretical calculations by Saito *et al.* [21] of the electronic properties of metal-metal (m@m), metal-semiconductor (m@s), and semiconductor-metal (s@m) DWCNTs predicted that almost all multilayer tubules are metallic if there is at least one metallic constituent monolayer carbon nanotube. However, just as hybridization effects in small radius SWCNTs can change the electronic band structure from that obtained by simply "folding" the graphite sheet band structure [13], the electronic structure of DWCNTs is also affected by the introduction of hybridization effects in the theoretical model. Additionally, the interlayer or interwall interaction between atomic orbitals is limited by the assumed model in any theoretical calculation. This is the case of the work by Saito *et al.*, in which the interlayer interaction is limited to atoms with a certain level of commensurability.

The results of calculations with more complex models are reported by Song *et al.* [15] and Zólyomi *et al.* [19]. Song *et al.* [15] performed DFT-LDA calculations for the (7,0)@(15,0), (7,0)@(18,0), (8,0)@(16,0) and (4,2)@(10,5) DWCNTs. They concluded that π-π stacking interaction causes band reconstruction of the inner tube. Meanwhile, Zólyomi *et al.* [19] performed DFT-LDA and intermolecular Hückel (IMH) model calculations of some DWCNTs and MWCNTs, and concluded that the interaction between layers combined with orbital mixing can in some cases lead to a semiconductor-to-metal transition of a DWCNT. Although focused on only a few DWCNT configurations, these results are important because they help us gain a better understanding on the physics that affect the electronic structure of DWCNTs in general.

Two works that expanded their studies to more DWCNT configurations are those of Okada *et al*. [20] and Liang *et al.* [59]. Okada *et al.* [20] reported total-energy electronic-structure calculations using the local density approximation in the density-functional theory for zigzag-zigzag (n, 0)@(m, 0) DWCNTs for n = 7, 8, and 10, and m = 15 - 20. In their calculations, DWCNTs with a (7, 0) inner tube were found to be metallic while those with (8,0) or (10,0) inner tube remain semiconducting. They concluded that the metallization of the DWCNTs is a consequence from the subtle balance between the curvature difference of the constituent tubes and the σ-π rehybridization of the inner tube. This implies that the distance between the walls in a DWCNT configuration affects its electronic structure near

the Fermi level. But in order to obtain a more comprehensive study of the effect of interwall distance on the electronic structure of DWCNTs, additional systems must be modelled and their electronic properties calculated.

One approach to a comprehensive study of the electronic properties of DWCNT is using tight-binding calculations. In their work, Liang *et al.* [59] used tight-binding calculations to study the effect of interwall coupling strength and average diameter ($D = (D_{inner} + D_{outer}) / 2$) on the electronic band structure of DWCNTs. They found that the energy band gap of s@s tubes decreases with the increase of interwall coupling and average diameter (at a constant interwall coupling, $t_p = 0.25$eV), with the gap vanishing completely for $D > 1.5$ nm, while the metallic property of the m@m tubes does not change with the interwall coupling and the diameter of DWCNTs. These results are limited to the interwall coupling chosen, and although the study was fairly comprehensive, it does not incorporate all the physical interactions in DWCNTs because it leaves out orbital hybridization effects and does not extend to more s@s DWCNTs with $D \leq 1.5$ nm.

Although the study by Saito *et al.* [21] of the electronic properties of DWCNTs comprehends all DWCNT configurations, as mentioned before, the model does not account for orbital mixing. A comprehensive study of several DWCNTs configurations that analyzes the effect of orbital mixing and interwall interaction on their electronic properties has not been reported in the literature to date.

2.2 Methodology

The DWCNT configurations studied were selected based on the interlayer distance and diameter of inner and outer tube found by theoretical and experimental studies. Pfeiffer *et al.* [3] reports calculations by Charlier *et al.* [60] of the interwall distance between inner and outer tubes and found it to vary between 0.33 and 0.41 nm, with an ideal separation of 3.39 Å. Endo *et al.* [61] found a diameter distribution of highly purified DWCNTs based on high-resolution TEM observations to fall between 0.4 and 1.3 nm for inner tubes and 1.0 and 2.2 nm for outer tubes (see Figure 9). Based on those measurements the chiral indices of zigzag inner tubes may range from (5,0) to (17,0), while the corresponding zigzag outer tube is set by choosing the indices of tubes that will not greatly exceed the interwall distances reported by Charlier *et al.* [60]. All the DWCNT configurations chosen for this study are zigzag-zigzag combinations.

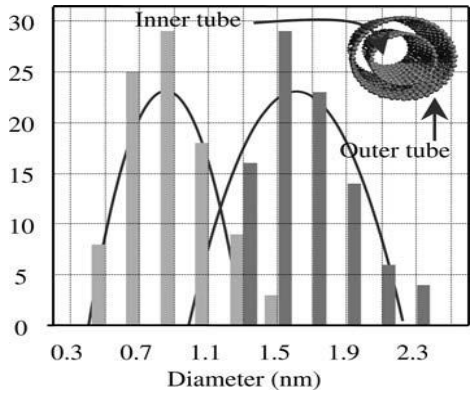

Figure 9. Diameter distribution of highly purified DWCNTs measured with high-resolution TEM [61].

The DWCNTs were modeled as a single unit cell by realizing their translational symmetry. Figure 10. A long zigzag@zigzag DWCNT is modeled in DFT code by using a single unit cell with translational symmetry. Figure 10 shows the example of a long zigzag@zigzag DWCNT being modeled as a single unit cell. For this example, both the inner and outer tubes have the same translational symmetry because they are both zigzag CNTs.

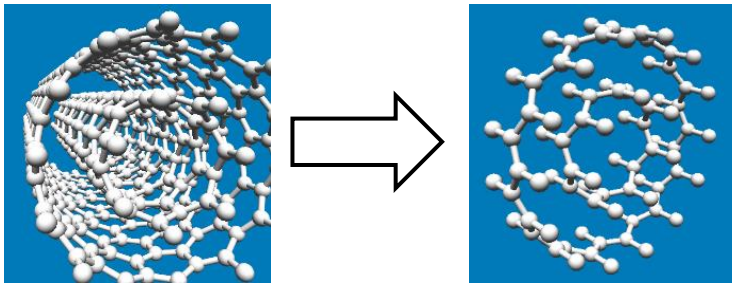

Figure 10. A long zigzag@zigzag DWCNT is modeled in DFT code by using a single unit cell with translational symmetry.

Similar to the methodology used when doing first-principles simulations of SWCNTs, the computational calculations were carried out using the SIESTA method and software [35], which makes use of density functional theory [36] under the Kohn-Sham auxiliary system [37]. Local density approximation, Ceperley-Alder flavor, was chosen for exchange-correlation potential. The pseudopotentials used were constructed according to the Troullier-Martins scheme, grouping core electrons into one orbital and allowing for four orbitals for the valence electrons of carbon atoms (2s, 2p, 3d, 4f). Energy bands were calculated by taking 20 points from the Γ to the X point.

The parameters for the DFT calculations were found by doing convergence tests in a similar fashion as the procedure used in the previous chapter for SWCNTs. The convergence criteria used was energy/atom ≤ 1 meV/atom and bandgap ≤ 5 meV for all the parameters, except PAO.EnergyShift, for which the same value as the basis set of SWCNTs was used. The tests were done with a (7,0)@(16,0) and a (15,0)@(24,0) DWCNT, for which the optimal parameters for both DWCNTs along with the comparison values for convergence are found below (Table 5). The lengths of the lattice constants in the CNT radial directions were determined by allowing an empty space of 10 Å on both sides of the DWCNT.

As was done for the case of SWCNTs, the Flexible Data Format (FDF) file used for one of the energy minimizations of a DWCNT is shown in Appendix A. This sample FDF file is for a zigzag@zigzag (8,0)@(16,0) DWCNT with one unit cell. The atomic coordinates of all the double-walled carbon nanotubes were generated using a program called *Nanotube Modeler* [45]. As seen in Appendix C, the band structure was also obtained using the SIESTA calculations. After the system minimized the energies and the atomic forces

were all below the chosen threshold (Table 5), SIESTA generated a file with all the band structure data, named *filename.bands*. A utility that is part of the SIESTA packaging converts this file to a data file readable by *gnuplot* [46]. Once converted, the band structure is plot for a range in energies using *gnuplot*. In our case, the Fermi energy was subtracted from all the energies when plotting the band structure.

Table 5. Converged parameters used in the DFT simulations of DWCNTs.

Parameter	Converged Value	Final Value
PAO.EnergyShift	50 meV	0.00005 Ry
kgrid	1,1,40	1,1,65
MD.MaxForceTol	20 meV/Å	5 meV/Å
MeshCutoff	400 Ry	700 Ry
Electronic Temperature	200 K	100 K
DM.Tolerance	$1x10^{-4}$	$1x10^{-6}$
LatticeConstant	34 – 43 Å	About 10 Å larger

2.3 Results and Discussion

Two cases were studied for DWCNTs: the electronic structure of the static configurations obtained by simply folding the graphene sheet, and the electronic structure of the relaxed configurations obtained by performing energy minimization within the DFT code until a value of MD.MaxForceTol ≤ 20 meV/Å was reached.

2.3.1 Static Structure Calculations of DWCNTs

The results of zigzag-zigzag DWCNTs with inner tube indices ranging from (7,0) to (15,0) are presented first. For the DWCNTs (7,0)@(m,0) where m = 15,16,17,18, the resulting electronic band structure shows an overlap of the conduction and valence bands at the Γ point, which means that these DWCNTs have metal-like behavior. This is consistent with previous DFT-LDA calculations by [15,20]. As explained in [15], the band reconstruction of the inner tube of (7,0)@(15,0) DWCNT is reasonably attributed to the interlayer π-π stacking interaction. In the same work, the overlap of the bands at the Γ point for the (7,0)@(18,0) is attributed to interlayer interaction, although the spacing is larger [15]. Meanwhile in [20] they explain that the metallization of the (7,0)@(16,0) and (7,0)@(17,0) is due to the overlap between the conduction band of the inner tube and the valence band of the outer tube.

The results of the calculations of zigzag-zigzag DWCNTs with inner tubes ranging from (8,0) to (15,0) are discussed according to their previously known electronic behavior [8–11]. Zigzag-zigzag DWCNTs in which their inner tubes are considered metallic from theoretical calculations show an interesting relation between interwall distance and band gap. Figure 11 shows the plot of band gap as a function of interwall distance for the m@s DWCNTs. It can be seen that the band gap increases as the interwall distance increases for the DWCNTs with (9,0) and (12,0) inner tube. This may seem counterintuitive because if the inner tube is considered metallic, as the interwall distance increases and the effect of interwall interaction is reduced the inner tube should regain its intrinsic metallic property. However, as shown in previous LDA calculations [13], hybridization effects in small radius nanotubes contributes to the creation of a band gap at the Fermi level. For example, Blasé *et al.* [13] obtained a band gap of 0.17 eV for a (9,0) SWCNT and Zólyomi *et al.* [14] obtained

0.096 eV, compared to 0.14 eV band gap from our DFT-LDA calculations. According to these results, the (9,0) SWCNT inner tube initially has a small band gap at the Fermi level which is closed by the lowest conduction band overlapping 0.035 eV (shown as negative value in plot) below the Fermi level when combined with a (17,0) outer tube. The band gap increases as a function of interwall distance until it approaches the value of 0.14 eV at the highest interwall distance, which is the band gap of the individual (9,0) SWCNT.

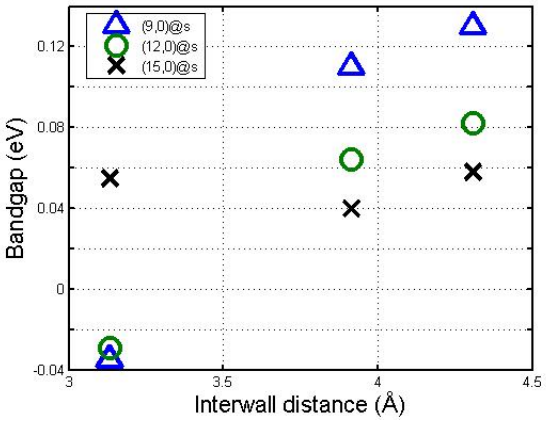

Figure 11. Plot of electronic band gap as a function of interwall distance for m@s DWCNTs.

The hybridization effect in individual nanotubes is reduced as the radius increases because curvature effects are tube-size dependent [13]. However, for the (12,0) and (15,0) SWCNTs a band gap remains from DFT-LDA calculations, although reduced to 0.09 and 0.055 eV, respectively. For comparison, Zólyomi *et al.* [14] calculated a band gap of 0.04 and 0.023 eV for the (12,0) and (15,0) SWCNT, respectively, while Song *et al.* [15] calculated a band gap of 0.08 eV for the (15,0) SWCNT. For the DWCNTs with (12,0) inner tube the lowest conduction band overlaps 0.029 eV (shown as negative value in plot) below the Fermi level when combined with a (20,0) outer tube, corresponding to the same interwall distance of the (9,0)@(17,0) of 3.13 Å; the band gap increases with increasing interwall distance, although this increase is less pronounced than the DWCNT with (9,0) inner tube. But similarly to the case of DWCNT with (9,0) inner tube, the band gap increase until it approaches the value of 0.090 eV calculated for the (12,0) SWCNT. Further evidence of the tube-size dependence of the effect of curvature on the orbital hybridization is seen for the case of DWCNT with (15,0) inner tube. A smaller band gap of the SWCNT, found from DFT-LDA calculations to be 0.055 eV, remains virtually constant when combined

with (23,0), (25,0), and (26,0) outer tubes. For the case of zigzag-zigzag m@s DWCNTs, it can be seen that interwall distance dependence only applies those with D < 1.4 nm, where $D = (D_{inner} + D_{outer})/\,2$. This difference in behavior between m@s DWCNTs of larger average diameter can be attributed to the reduction of the effect of curvature on the orbital hybridization of the inner tube, which in turn has an effect on the interwall interaction when combined in DWCNT configurations. This particular type of DWCNT configurations could be used when band gap tuning is desired.

For the cases where the inner tube is considered semiconductor from theoretical calculations, a marked difference can be observed in the band gap between the s@m and s@s DWCNTs. As shown in Figure 12a, the band gap of s@m DWCNTs varies between values less than 78 meV and overlaps of -66 meV, while the band gap of s@s DWCNTs varies between 0.31 and about half eV (Figure 12b). For comparison, Song *et al.* obtained a 0.35 eV band gap for a (8,0)@(16,0) DWCNT using a plane-wave LDA approach [15], Okada *et al.* obtained a 0.26 eV band gap for a (8,0)@(19,0) DWCNT and about half eV for (10,0)@(19,0) and (10,0)@(20,0) DWCNTs also using a plane-wave LDA approach [20], while Zólyomi *et al.* calculated the band gap of a (8,0)@(17,0) DWCNT as 0.2 eV using a localized basis set LDA approach [19]. Neither s@m nor s@s DWCNTs shows any clear dependence of the band gap on interwall distance, but only on the type of outer CNT. The group of s@m DWCNTs shows narrow gap semiconductor and semimetal behavior while s@s DWCNTs remain semiconductors. Additionally, the band gap of s@s DWCNTs did not decrease as the average diameter increases (Figure 13), contrary to the results published by Liang *et al.* [59] using tight-binding calculations.

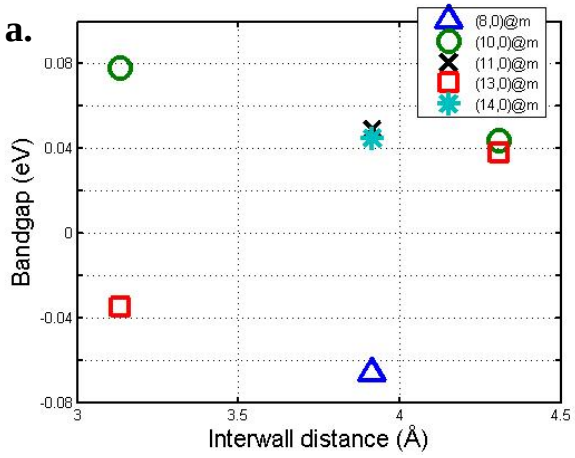

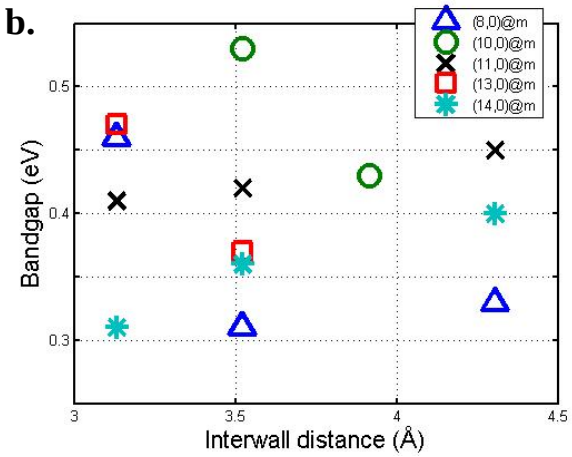

Figure 12. Band gap values from LDA calculations as a function of interwall distance for a) s@m DWCNTs and b) s@s DWCNTs.

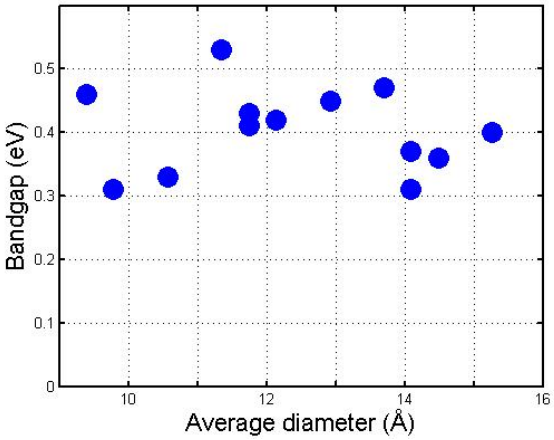

Figure 13. Band gap in eV as a function of average diameter for s@s DWCNTs.

Lastly, the m@m DWCNTs show a narrow band gap with values between 2.2 and 18 meV. This range of values is lower than the band gaps of s@m DWCNTs, except for the cases with overlap at the Γ point, which makes the m@m DWCNTs in general more suitable for better conductance applications over any of the other possible combinations of zigzag DWCNTs. For the case of zigzag nanotubes, using DWCNTs for conductance purposes seems advantageous over SWCNTs. Of all the zigzag-zigzag DWCNTs with chiral indices (n, 0)@(m, 0) for n = 7 - 15, and m = 15 – 26 studied, over 60% have a band gap ≤ 0.14 eV, which puts them in the range of metals, semimetals, or narrow band gap semiconductors. For comparison, of all the SWCNTs used in the DWCNT combinations

studied, only 30% have a band gap ≤ 0.14 eV. Also, of all the DWCNTs studied with at least one constituent metallic SWCNT from theoretical calculations, only 29% of them were found to have a zero or overlap band gap, contrary to the prediction by Saito *et al.* [13].

2.3.2 Relaxed Structure Calculations of DWCNTs

According to our DFT calculations of zigzag@zigzag double-walled carbon nanotubes, the change in energy per atom with respect to graphene increases as the diameter of the outer tube becomes smaller for interwall distances between 0.31 and 0.43 nm, as seen in Figure 14. Also it can be seen that the energy difference per atom with respect to graphene decreases as the outer tube diameter increases and should approach zero in the limit that the curvature of the outer tube becomes negligible. It is important to note that for most of the inner@outer tube configurations, the lowest energy corresponds to an interwall distance of 0.35 nm, which is within the range of previous calculations [60]. However, for three DWCNTs in the small diameter range the difference in energy per atom with respect to graphene continues to decrease as the interwall distance increases. This is an interesting result, which points to the possibility that the (5,0), (6,0), and (7,0) carbon nanotubes do not interact well with an outer tube at a distance between 0.31 and 0.43 nm, and there exists another preferable DWCNT configuration.

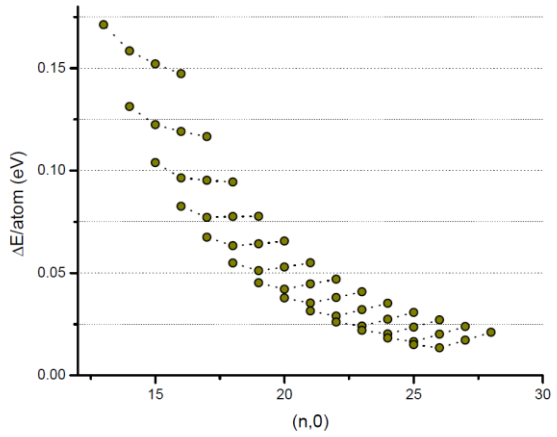

Figure 14. The difference in energy/atom with respect to a graphene sheet for zigzag@zigzag DWCNTs.

When comparing the energy per atom with pristine SWCNTs, there are three ways to do so. First one is to make the comparison using the chiral indices of the outer tube in the DWCNT configuration, as it is shown in Figure 15. This comparison shows that for outer tubes with indices (13,0) to about (18,0) there is an increase in energy change with respect to graphene, and a close match in energy for indices (19,0) to (28,0). This would indicate that SWCNTs are more stable than DWCNTs for tubes smaller than the (19,0) zigzag tube. The second type of comparison would be to use the chiral indices of the inner tube within the DWCNT configuration instead. By doing this we see that the ΔE/atom decreases with respect to the pristine SWCNTs (Figure 16). Finally, the third approach is to compare the DWCNTs with the SWCNTs using the average diameter of the DWCNT configuration. In Figure 17 we see that using this type of comparison shows a closer match in ΔE/atom with respect to graphene between the SWCNTs and DWCNTs. This indicates that DWCNTs could be considered to be one single system, as opposed to thinking of them in terms of inner and outer tubes concentrically arranged. This is a result of the interwall interaction between the two tubes.

It is also noticeable that the DWCNTs with the larger average diameters are most stable energetically than their SWCNT counterparts, as shown in Figure 17. This could be explained by looking at the binding energy between the inner and outer tubes as a function of average diameter. Figure 18 shows a significant increase in binding energy for larger diameter DWCNTs. This interaction between the two tubes makes this type of system more stable than SWCNTs. Additionally, Figure 18 shows that the ideal interwall distance is about 3.5 Å, which differs slightly for the value previously reporter [60].

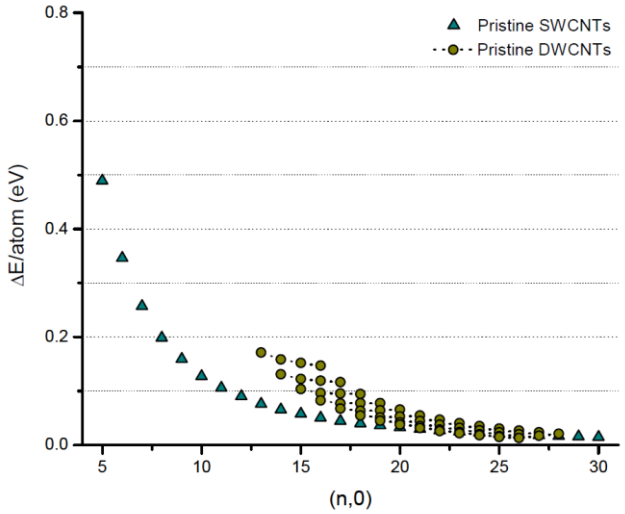

Figure 15. Comparison of difference in energy/atom with respect to a graphene sheet for pristine SWCNTs and DWCNTs as a function of the chiral index of the outer tube.

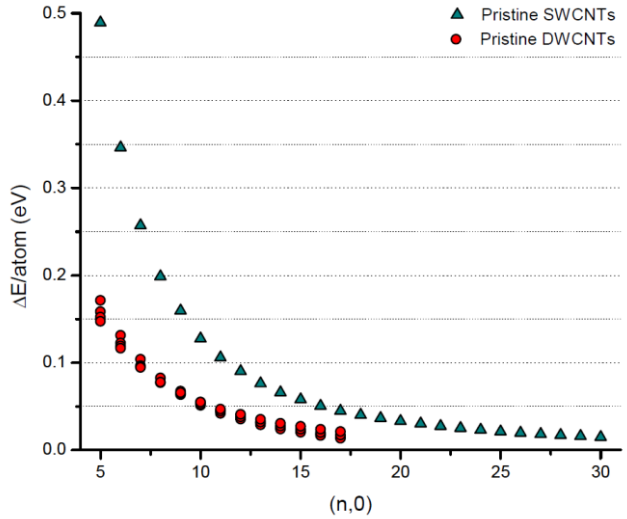

Figure 16. Comparison of difference in energy/atom with respect to a graphene sheet for pristine SWCNTs and DWCNTs as a function of the chiral index of the inner tube.

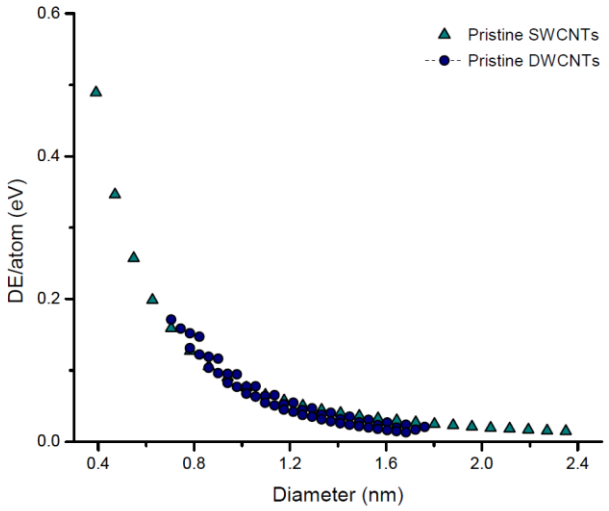

Figure 17. Comparison of difference in energy/atom with respect to a graphene sheet for pristine SWCNTs and DWCNTs as a function of the average diameter.

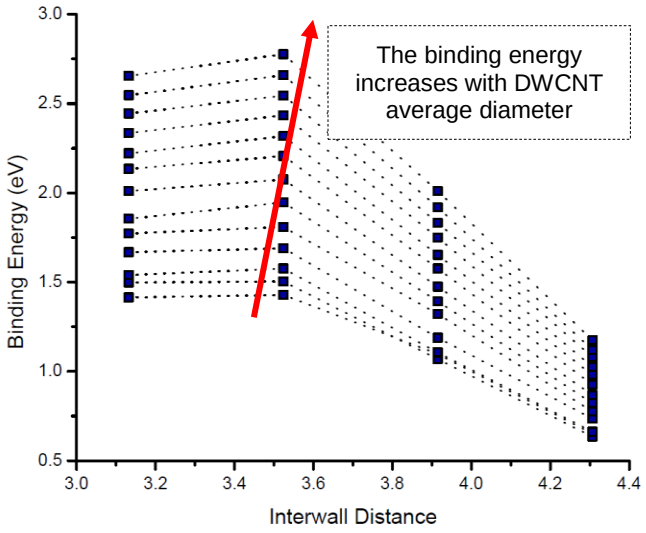

Figure 18. Binding energy between the inner and outer tubes in a DWCNT configuration as a function of the interwall distance.

The band structure was calculated between the Γ and X points, as shown in

Figure **6**. An example of a band structure obtained with DFT-LDA calculations is shown below in Figure 19 for the (16,0)@(25,0) DWCNT. The band gap was found by calculating the difference in energy at the Γ point (labeled as G in the figure) at the Fermi level between the lowest point of the conduction band and the highest point of the valence band. The band

structure plots for all the other DWCNTs considered in this work are shown in Appendix D.

The DWCNTs combinations have been categorized according to their chiral indices. Per theoretical analysis, zigzag nanotubes with leading chiral indices $n = 3k$ (k being an integer) are considered metallic. As has been mentioned before, the curvature induces a band gap in in these CNTs; however, in this section of this thesis work, they will be referred as *m-type* tubes for "metallic". Similarly, the DWCNTs with leading chiral index $n = 3k+1$ or $n = 3k+2$ (k being an integer) are considered semiconductor from previous theoretical predictions [8–11] and will be referred here as *s-type* for "semiconductor". The different combinations of DWCNT configurations will be referred as m@m, m@s, s@m, and s@s.

Figure 19. Band structure of the (16,0)@(25,0) DWCNT.

Some DWCNT configurations were compared to the literature before jumping into the analysis of the all the results. The DWCNT configurations with (7,0), (8,0) and (10,0) inner tube are some of the few which have been studied before regarding the electronic structure. The table below shows a comparison of their results and ours. It can be seen that our calculations were able to reproduce the behavior of the DWCNTs with (7,0) inner tubes, but there are some discrepancies in the results with the other cases in Table 6. All of the DFT-LDA calculations cited below used plane-waves for the basis set; this differs from the SIESTA method which uses numerical atomic orbitals to represent the basis set of the carbon atom [38]. As was mentioned before, band gap calculations are especially sensitive to the choice of basis set, which explains why our results may differ from others that used a different mathematical approach to the description of the valence electron orbitals.

Table 6. Comparison of the band gaps for some of the values reported in the literature to our work. Units of eV.

DWCNT	DFT-LDA [20]	DFT-LDA [15]	DFT-LDA [19]	Our work
(7,0)@(15,0)	Metallic	0		0
(7,0)@(16,0)	0		0	0
(7,0)@(17,0)	Overlap			0
(7,0)@(18,0)	Metallic	0		0
(8,0)@(16,0)		0.35		0.46
(8,0)@(17,0)			0.2	0.13
(8,0)@(19,0)	0.26			0.15
(10,0)@(19,0)	~0.5			0.54
(10,0)@(20,0)	~0.5			0.25

The first group is the m@m DWCNTs. For such type of combination, the band gap is zero at the Fermi level. Excepting the (6,0) CNT, all the m-type SWCNTs have been found to have non-zero band gaps due to the effect of curvature, as shown in Figure 7. However, when arranged in a DWCNT configuration and their structures relaxed as explained in the Methodology section, their bands are shifted enough to close the gap at the Fermi level. This suggests that the interwall interaction has an effect on the electronic properties of m@m DWCNTs.

The band gap of the group of m@s DWCNTs shows a dependency on the average diameter for the combinations with inner tube (9,0) and above, as shown in Figure 20. The case of inner tube with chiral index (6,0) shows a zero band gap. Also, we observe that the band gap seems to be dominated by the outer tube for the cases with inner tube with chiral index of (9,0) and above. We come to this conclusion by noting that the (9,0), (12,0), and (15,0) SWCNTs have band gaps of 0.13, 0.079, and 0.061; such values are only approximated when the interwall distance is 0.31 nm, after which the band gap increases for interwall distances of 0.39 and 0.43 nm. Therefore, the inner tube is able to affect the band structure for small interwall distance by maintaining the gap similar to that of the lone inner tube (Figure 21). Once the interwall distance increases, the inner tube cannot affect the band structure, which is actually dominated by the semiconductor properties of the outer tubes (Figure 21).

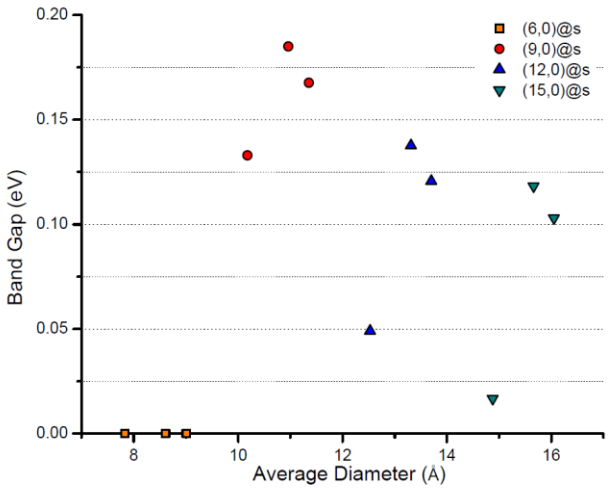

Figure 20. Band gap as a function of average diameter of relaxed m@s DWCNTs.

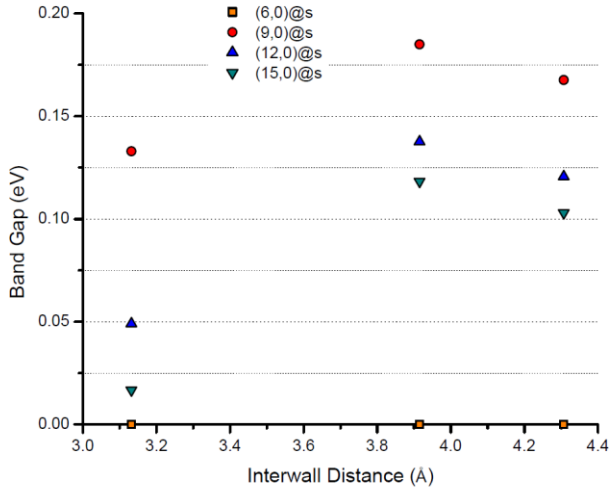

Figure 21. Band gap as a function of interwall distance of relaxed m@s DWCNTs.

The third group, being the s@m, case shows band gaps that are also dependent on the average diameter of the DWCNT (Figure 22). This group also shows a dominance of the outer tube with either zero or narrow band gaps characteristic of zigzag CNTs with index n = 3k (n being an integer). Figure 23 shows a clear proportional dependence of the band gap on the interwall distance, with quite a few DWCNTs showing zero band gap behavior. This is interesting because it means that the band gap can be tuned even within this narrow band gap region. It is also important to mention that at 300 K the thermal energy is equivalent to 26 meV, which is larger than all the band gaps of the s@m DWCNTs. Therefore, for room temperature applications, the thermal energy in the surroundings could

provide energy for the electronic to overcome the electronic band gap and transition to the conduction band.

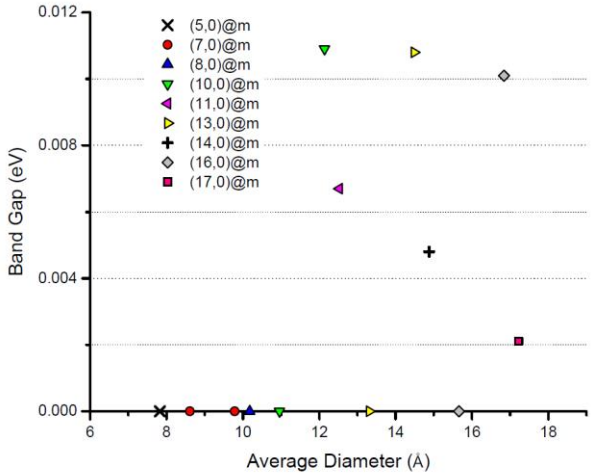

Figure 22. Band gap as a function of average diameter of relaxed s@m DWCNTs.

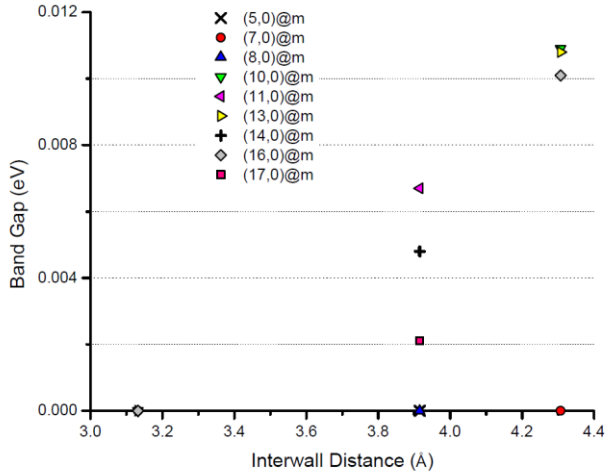

Figure 23. Band gap as a function of interwall distance of relaxed s@m DWCNTs.

Lastly, the case of s@s DWCNTs also shows a clear dependence of the electronic band gap on the average diameter (Figure 24), with the exception of the DWCNTs with (5,0) and (7,0) inner tubes, which have a zero band gap. The band gaps of these group of molecules stay between 0.15 and 0.48 eV, with the aforementioned exceptions. And also for the s@s DWCNTs, the band gap is a function of interwall distance, as seen in Figure 25.

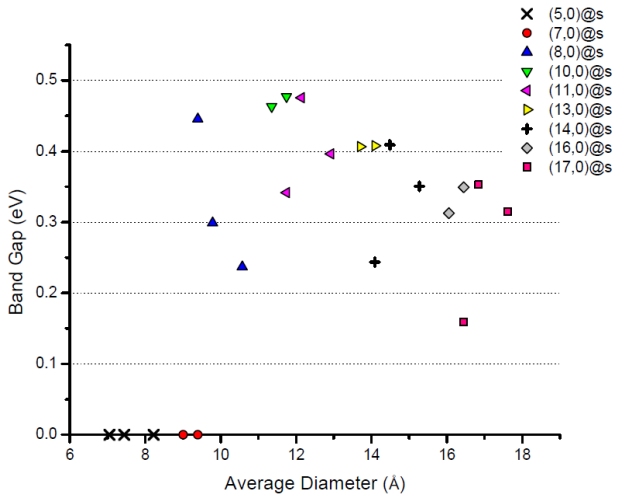

Figure 24. Band gap as a function of average diameter of relaxed s@s DWCNTs.

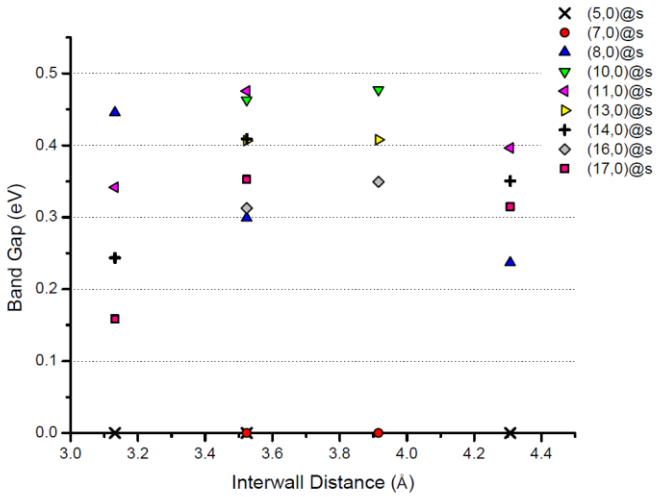

Figure 25. Band gap as a function of interwall distance of relaxed s@s DWCNTs.

Finally, Figure 26 shows all four combinations of nanotubes and their behavior as a function of interwall distance. This figure clearly shows the four specific regions of band gap that can be obtained using DWCNTs, which can be named as: zero band gap region (not shown), narrow band gap region (green region on insert), small band gap region (blue region), and medium band gap region (pink region). When attempting to tune the band gap of a carbon nanotube, zigzag@zigzag DWCNTs offer not only the possibility to make a choice based on the type of inner and outer tubes, but also to choose a region first, and then tune that choice within the region itself.

The dependence of the electronic band gap of all the zigzag@zigzag DWCNTs with respect to average diameter is shown in Figure 27. Previous work [59] predicted the band gap of s@s DWCNTs to be inversely proportional to the average diameter. Such tendency was shown above in Figure 24 and it is also seen to be the case for s@m and m@s DWCNTs. Also in Figure 27, the band gaps found in previous works [15,19,20] are shown. It can be observed that previous DFT calculations are limited to few zigzag@zigzag DWCNTs and mostly those of small average diameter. Our work is able to expand the study of DWCNTs by doing DFT-LDA calculations in a systematic way.

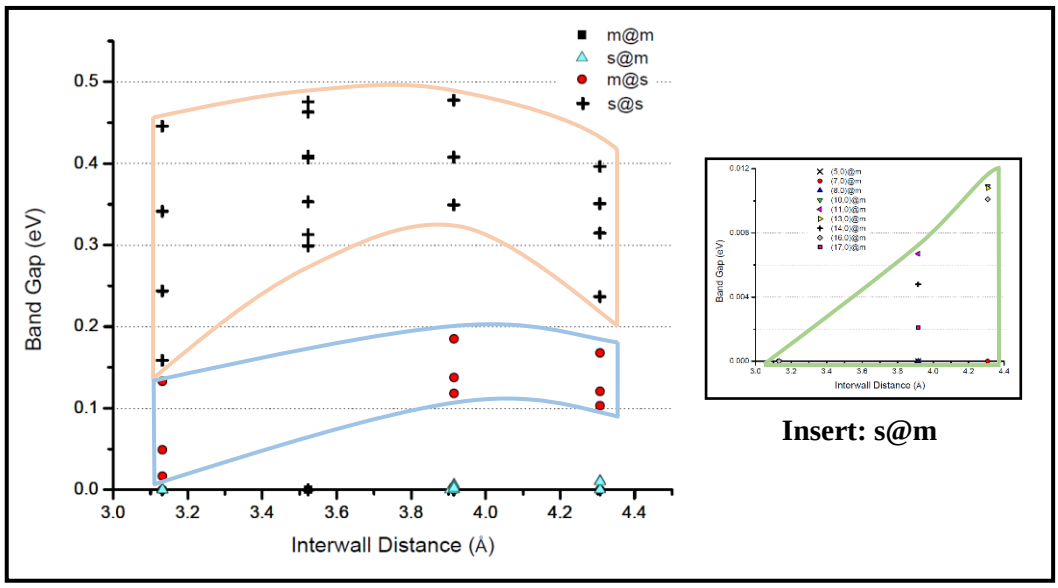

Figure 26. Band gap as a function of interwall distance of all relaxed zigzag@zigzag DWCNTs.

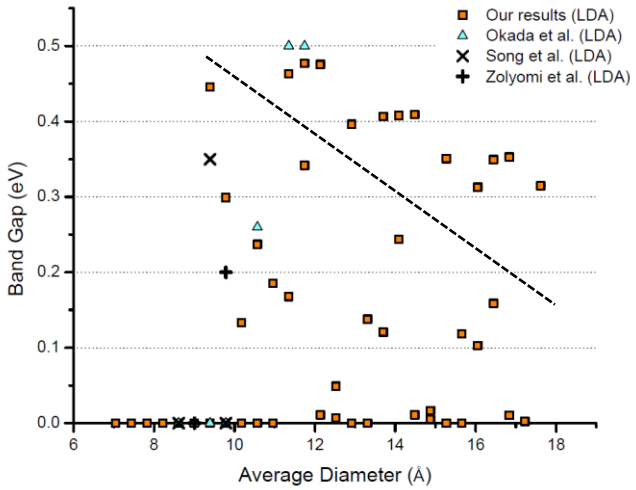

Figure 27. Band gap as a function of average diameter of all relaxed zigzag@zigzag DWCNTs.

We may draw comparisons in terms of band gap between the results obtained for single- and double-walled carbon nanotubes. As previously done, the range of diameters corresponding to the chiral indices chosen in our study were divided into four. According to this sectioning, the larger diameter SWCNTs have the smallest average band gap (Table 7). For the DWCNTs, each molecule may be assigned to a diameter range based on its average diameter or on the diameter of the outer tube. When considering the average diameter of the DWCNT, those with the smaller diameters have the smallest average band gap and corresponds to the case of average diameter between 0.4 and 1.0 nm. If the outer diameter is used instead when arranging the DWCNTs, the diameter range of 1.0-1.5 nm has the smallest average band gap. Either way, the average diameter is smaller for the DWCNTs for all diameter ranges, and overall the average band gap is reduced by about 50%.

Table 7. Average band gap of SWCNTs and DWCNTS as obtained from DFT calculations.

	SWCNTs	**DWCNTs**	
Diameter (nm)	Average band gap (eV)	Average band gap-av.dia. (eV)	Average band gap-out.dia. (eV)
0.4-1.0 nm	0.34	0.053	
1.0-1.5 nm	0.43	0.18	0.096
1.5-2.0 nm	0.28	0.17	0.18
2.0-2.5 nm	0.21		0.19
OVERALL	**0.32**	**0.15**	**0.15**

2.4 Conclusions

For the case of static structure calculations, it was observed that the electronic band gap of the DWCNTs depends on the interwall distance only for metallic-semiconductor configurations and on the intrinsic properties of the constituent tubes in all other combinations. It was also observed that the calculated band gap for most of the metallic-metallic DWCNTs was smaller than semiconductor-metallic, metallic-semiconductor, and semiconductor-semiconductor configurations. Metallic-semiconductor DWCNTs were found to be desirable for band gap tuning applications because of their dependence on interwall distance, opening up the possibility of using such systems in electronic devices applications, such as transistors. Other applications include the use of DWCNTs in macroscopic carbon nanotube conducting wires, for which metallic-metallic and semiconducting-metallic zigzag-zigzag DWCNTs were found to be the most desirable configurations due to their small band gaps [62].

When considering the relaxed structure of zigzag@zigzag DWCNTs, novel phenomena appears. The binding energy of the DWCNTs increases with average diameter. The electronic band gap depends on the interwall interaction for the metallic-semiconductor, the semiconductor-metallic and the semiconductor-semiconductor combinations. Four specific regions of band gap that can be obtained using DWCNTs, which can be named as: zero band gap, narrow band gap, small band gap, and medium band gap region. When attempting to tune the band gap of a carbon nanotube, zigzag@zigzag DWCNTs offer not only the possibility to make a choice based on the interwall interaction, but also to choose a region of interest first based on the chiral indices of the inner and outer tubes, and then tune that choice within the region itself. The downward tendency of the value of the band gap with respect to the average diameter has been made clear for the calculations of the relaxed structures of semiconducting-semiconducting DWCTNs. But also the metallic-semiconducting and even, to a small degree, the semiconducting-metallic combinations show a downward tendency of the electronic band gap as a function of average diameter.

For applications of electrical conduction, such as an electrical wire, the m@m and s@m DWCNTs are the most desirable because they are in the zero and narrow band gap regions. The most important parameter is the chirality, because the chiral index determines to a

greater degree the electronic band gap of the single- and double-walled carbon nanotube. The average diameter of the DWCNT is the second most important parameter when determining the electronic band gap. The interwall distance does not affect the electronic band gap as much as the chiral index and average diameter, but it has the capacity of fine-tuning the band gap. On average, the electronic band gap of the DWCNTs studied is about 50% smaller than that of the SWCNTs studied in this work.

2.5 Future Work

Other DWCNT configurations such as chiral@chiral and armchair@armchair need to also be studied in order to more fully understand the effect of interwall interaction on the electronic structure of all DWCNTs. Studying chiral@chiral DWCNTs poses a challenge because of the amount of possible combinations; perhaps some generalizations could be made from studying a few chiral@chiral combinations in light of the results shown in this work. It is possible that the electronic band gap for chiral@chiral DWCNTs is also dependent on the electronic properties of the individual inner and outer tubes for the most part, and that it also shows some dependence on the interwall distance as well as the average diameter.

Extending this type of study to other multi-walled carbon nanotubes (MWCNTs) poses even greater challenges because of the amount of tube combinations. Perhaps the results of this work could be used to make some predictions regarding the electronic properties of MWCNTs, such as the fact the outer tube usually dominates the behavior of the electronic band gaps in DWCNTs.

Chapter 3

Effect of Vacancy Defects on the Electronic Properties of Carbon Nanotubes

3.1 Introduction

In general, defects can modify the properties of carbon nanotubes depending on the method used to generate them, their concentration, and the type of nanotubes. In some cases, defects can help increase the adhesion of carbon nanotubes to a polymer matrix [63,64], when mixing them to create a composite material. This could be beneficial to both the mechanical and electrical behavior of polymer nanocomposites that use CNT as fillers. Also, defects could improve the properties of carbon nanotube bundles by helping create defect-mediated covalent bonds between SWCNTs [65,66] in bundles or between shells of MWCNTs [67]. In carbon nanotubes, defects can be generated by irradiation [65,66,68] or by chemical treatment [69], or can appear during growth or purification [70,71]. Particularly, vacancies can give rise to deterioration of the axial mechanical properties, as was found by molecular dynamics simulations and continuum theory [72]. Additionally, experimental work has shown that small dose of irradiation improves the mechanical properties of CNT bundles because of the irradiation-induced inter-tube links, while a high-dose irradiation results in decrease of their mechanical characteristics due to the generation of vacancy defects in the atomic structure [72,73].

As mentioned in the two previous chapters, the electronic properties of carbon nanotubes were predicted by early theoretical works to depend on their diameter and chirality [8–11]. For zigzag nanotubes, the metallic-like properties of the tubes with chiral indices (n,0) with n = 3r (where r is an integer) were found to be modified due to orbital hybridization caused by the nanotube curvature. However, both the theoretical predictions and the computational calculations using DFT approach assume a perfect CNT structure. Imperfections can be present in carbon nanotubes (due to different reasons, as mentioned above) and could also change their properties. According to J.-C. Charlier [24], these imperfections can be classified into four main groups: topological (introduction of ring sizes other than hexagons), rehybridization (ability of carbon atom to hybridize between sp^2 and sp^3), incomplete bonding defects (vacancies, dislocations, etc.), and doping with other elements.

Of particular interest to this work is the effect of vacancies on the structure and properties of carbo nanotubes. The removal of carbon atoms from the structure of of SWCNTs has been observed to cause surface reconstructions and drastic dimensional changes [74]. This

behavior has also been studied via molecular dynamics simulations [24]. It was found that the dangling bonds surrounding a vacancy in the structure caused the system to become energetically unstable; such instability was mended by the rearrangement of the structure in which two-coordinate carbon atoms try to recombine to form three-coordinate network [24]. After removal of about half the atoms of a pristine (10,10) armchair SWCNT , the defective nanotube is composed of mainly five-, six-, and seven-membered rings (Figure 28). Additional to the surface reconstruction, the introduction of vacancies into the structure of an armchair CNT caused an increase of the density of states (DOS) close to the Fermi level. That can be clearly observed in the DOS plot for the pristine (Figure 29a) and defective (Figure 29b) cases, respectively.

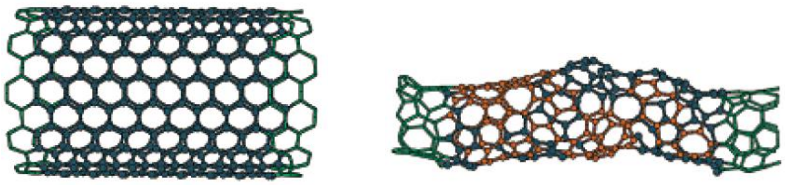

Figure 28. Molecular dynamics simulations of the surface reconstruction of a) a (10,10) single-walled carbon nanotube b) after random extraction of about half the atoms [24].

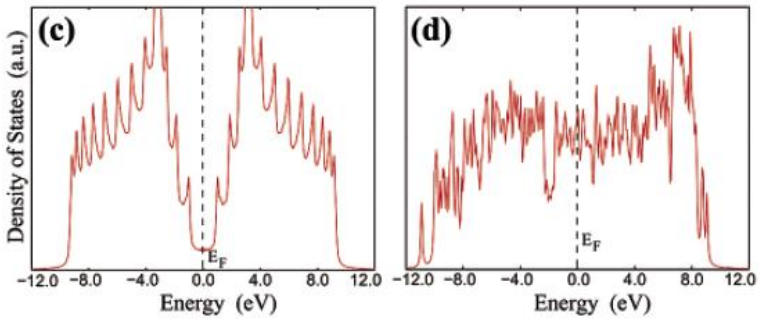

Figure 29. Density of states of a) a pristine (10,0) zigzag single-walled carbon nanotubes and b) the same tube after removal of about half of its atoms.

Following the idea of the increase in the DOS near the Fermi level, one may envisioned the effect vacancy defect could have on the electronic properties of not only metallic armchair nanotubes, but also on some of the intrinsically semiconductor zigzag nanotubes. This idea was undertaken by Orellana *et al.* [23] using DFT calculations within the generalized gradient approximation (GGA) and a computational method similar to the one used in this work. In their study of armchair CNTs with chiral indices (6,6) and (8,8), and

zigzag CNTs with chiral indices (10,0) and (14,0). Using the SIESTA code, they relaxed the structure of all CNTs using the conjugate gradient algorithm using a convergence criterion of 50 meV/Å maximum atomic force. For armchair CNTs, their results show that adding a vacancy to an (6,6) or (8,8) nanotube modifies its electronic state near the Fermi level but the metallic behavior is maintained (Figure 30). This corresponds to vacancy concentrations of 0.83 and 0.63 %, respectively. Similarly, their results of the (10,0) and (14,0) zigzag nanotubes show modifications to the DOS near the Fermi energy, and a reduction in the electronic band gap of the (10,0) CNT from about 0.8 eV to 0.1 eV (Figure 30). The vacancy concentrations used in their calculations correspond to 0.83 and 0.60 %, respectively. It was also observed that when the vacancy concentration of the (10,0) CNT was reduced from 0.83 to 0.42 %, the band gap increase by about twice its value to 0.2 eV.

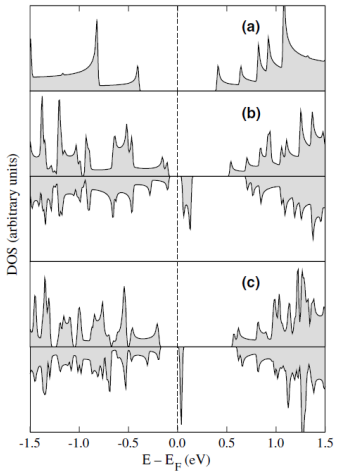

Figure 30. Spin-resolved density of states of a) the pristine (10,0) CNT, b) with vacancy concentration of 0.83% and, c) with vacancy concentration of 0.42 %. Taken from [23]**.**

Looking back at Figure 7, we notice that the band gap behavior depends on the chirality and the diameter of the zigzag nanotube, as found from DFT-LDA calculations. Previous works already mentioned focus on the behavior of a few CNTs (2 armchair and 2 zigzag), however, it's not clear whether the same behavior will be followed by other zigzag CNTs, or perhaps the behavior is chirality-dependent within the range of zigzag nanotubes studied in *Chapter 1*. In this chapter we have undertaken to study the effect of vacancy defects on the electronic properties of a range of zigzag carbon nanotubes at different vacancy concentrations.

3.2 Methodology

The computational simulations were carried out using the same method mentioned in Chapter 1 for single-walled carbon nanotubes. The parameters for the DFT simulations in SIESTA are shown in Table 2.

3.2.1 Single-walled carbon nanotubes

In order to model the vacancy defects in single-walled carbon nanotubes, two cases were selected: one vacancy per unit cell (referred to as 1v/1uc from this point on) and one vacancy per two unit cells (referred to as 1v/2uc from this point on). In order to achieve these two models, the geometries of all the SWCNTs simulated in Chapter 1, zigzag CNTs with chiral indices (5,0) – (30,0) were modified by removing one carbon atom from the unit cell. The 1v/1uc defective geometry is shown in Figure 31a. For the range of SWCNTs mentioned, the vacancy concentration of 1v/1uc corresponds to 5.26 – 0.84%. This vacancy concentration is much larger for SWCNTs with small diameter. In order to study the effect of vacancies at smaller concentrations, the case of one vacancy per unit cells (Figure 31b) was also studied for zigzag CNTs with chiral indices (5,0) – (18,0). Larger diameter zigzag nanotubes (chiral index of (19,0) and above) with two unit cells were not able to be simulated using DFT method due to computational cost constraints. The case of 1v/2uc for the chiral indices mentioned correspond to a range of vacancy concentration of 2.56 – 0.70%.

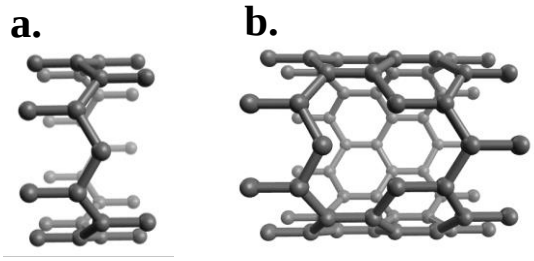

Figure 31. Geometry used for the study of vacancy defects with a) one vacancy per one unit cell (1v/1uc) and b) once vacancy per two unit cells (1v/2uc).

The defective geometry for both cases was then relaxed using energy minimization algorithm (conjugate gradient) in the SIESTA code to a maximum force of 40 meV/Å. Energy bands were calculated by taking 40 points from the Γ to the X point. The energy bands were analyzed by converting the file with .BANDS file extension to a data file using

a SIESTA utility called *gnubands*, which was plotted using a computer program called gnuplots [46].

3.2.2 Double-walled carbon nanotubes

Additional to the study of vacancy defects on single-walled carbon nanotubes, the effect on the structure and electronic properties of double-walled carbon nanotubes was studied too. In order to do this, the (8,0)@(16,0) DWCNT was chosen as a case scenario. First, the structure of the molecule was relaxed by minimizing the energy and the atomic forces using the conjugate gradient (CG) algorithm in SIESTA until the maximum force was found to below the convergence criterion.

Similar to the methodology used for the study of other CNTs, the (8,0)@(16,0) DWCNT was modeled as an infinitely-long carbon nanotube isolated from interacting with any other molecules by using simulation box with the length of two unit cells along the tube axis, and at least five times the length of two unit cells in the two directions perpendicular to the tube axis. In the figure below, two views of the supercell used for the simulation of the (8,0)@(16,0) DWCNT. As seen on the right image, a carbon atom has been removed from the surface of the outer tube prior to structural relaxation and energy minimization process in SIESTA.

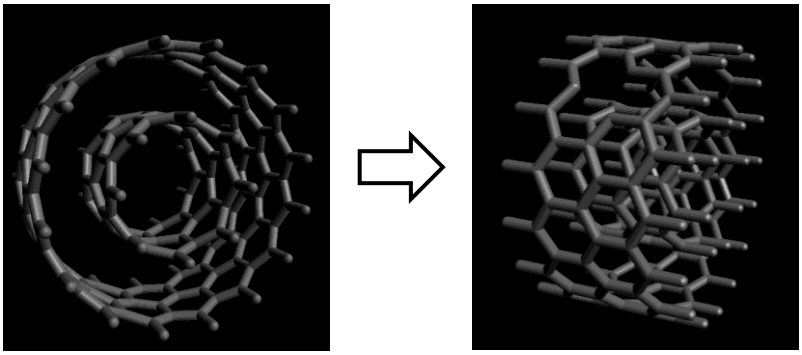

Figure 32. Supercell used for the simulation of vacancy defects in DWCNTs.

3.3 Results and Discussion

3.3.1 Effect of vacancy defects on SWCNTs

The unit cells shown above were relaxed according to the parameters mentioned in *3.2 Methodology* section. The relaxed structures are shown in Figure 33a-b, from which a clear rearranging of the atomic positions near the vacancy defect can be observed. For the structural relaxation of the case with one vacancy defect per one unit cell, the atoms labeled 1 and 2 in Figure 33a move closer towards each other to form a pentagonal shape. Similarly, Figure 33b shows atoms 1 and 2 being rearranged towards each other and forming a pentagonal shape, for the case of one vacancy per two unit cells (referred to as 1v/2uc from this point on). Atom 3, as shown Figure 33a-b, also experiences a repositioning. This can be observed more clearly in Figure 34, where it is shown how the carbon atom moves up from the tube surface for the 1v/2uc case. This side view also shows that the rearrangements of atoms 1 and 2 is not only towards each other but also downward, which causes an inward bending of the nanotube surface. The rearrangement of the atoms around the vacancy defects coincides with previous computational simulations (MD) of the structural modification of carbon nanotubes due to vacancies [74].

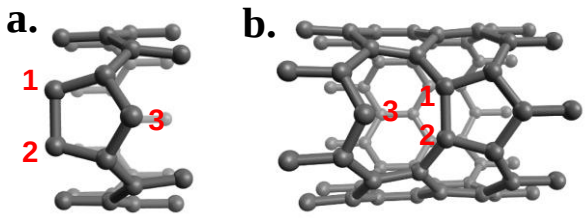

Figure 33. Rearranged geometry after structure relaxation for the case of a) one vacancy per one unit cell (1v/1uc) and b) one vacancy per two unit cells (1v/2uc).

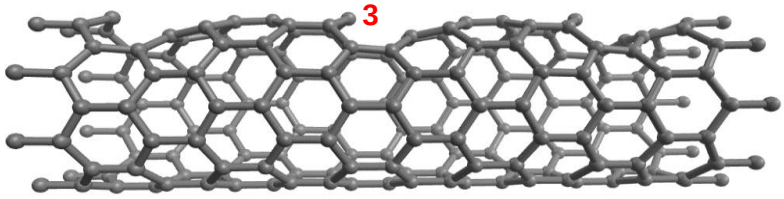

Figure 34. Sideview of three periodic unit cells of the relaxed structure of the case of one vacancy per two unit cells (1v/2uc).

The loss of a carbon atom on the otherwise pristine cylindrical honeycomb lattice of the carbon nanotube causes the structure to suffer some changes, as shown above. The

difference in energy per atom with respect to graphene was calculated for all the SWCNTs with chiral index from (5,0) – (30,0) for the case of 1v/1uc, and from (5,0) – (18,0) for the case of 1v/2uc. As seen in Figure 35, the rearrangement of the atoms brings the structure to a less table energy configuration. Creating a vacancy per one or two unit cells increases the energy difference per atom with respect to graphene. Similar to the pristine nanotubes, this energy difference decreases as the chiral index (or diameter) of the zigzag nanotube increases.

The rearrangement of the structure due to the loss of a carbon atom per one or two unit cells causes a change on the electronic cloud surrounding the carbon atoms. This change on the electronic orbitals in turn causes a change on the electronic band structure of the zigzag single-walled carbon nanotubes. The electronic band gap also suffers modification for the defective cases with respect to the pristine nanotubes, from which the band gaps were calculated (see Figure 36). It can be observed that a significant reduction of the band gap occurs for all zigzag CNTs.

The band gap of the pristine (5,0) and (6,0) SWCNTs is zero and remains unchanged for 1v/1uc or 1v/2uc. For zigzag tubes with chiral index n = 3k (except the already mentioned (6,0) CNT), the narrow band gap that appeared due to curvature, disappears for both 1v/2uc and 1v/1uc. The band gap of zigzag tubes with chiral index n = 3k+1 reduces depending on the vacancy defect concentration. For 1v/2uc, the band gap reduces from 0.21-0.72 eV down to 0.10-0.19 eV, and by increasing the vacancy concentration for 1v/2uc the band gap further reduces to zero. There are only two exceptions, the (22,0) and the (25,0) CNTs, for which the band gap reduces with respect to the pristine case, but it does not go completely to zero, as seen in Figure 36. Finally, the group of zigzag tubes with chiral index n = 3k+2 shows similar behavior, for which the band gaps reduces for 1v/2uc from 0.61-0.94 eV to values within 0.21 and 0.36 eV. Increasing the vacancy concentration to 1v/1uc closes the band gap for all of them, except for the (29,0) CNT. The exceptional cases of the non-zero band gap CNTs with 1v/1uc have in common their larger diameter, all of them above 1.7 nm; however, not all zigzag CNTs with chiral index $n = 3k+1$ or $n = 3k+2$ and a diameter larger than 1.7 nm have a non-zero band gap when a vacancy per unit cell is added to the structure.

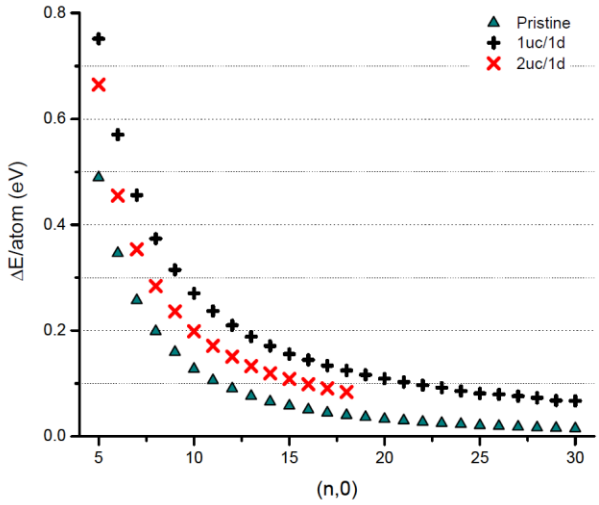

Figure 35. Comparison of the difference in energy/atom with respect to a graphene sheet of pristine and defective SWCNTs.

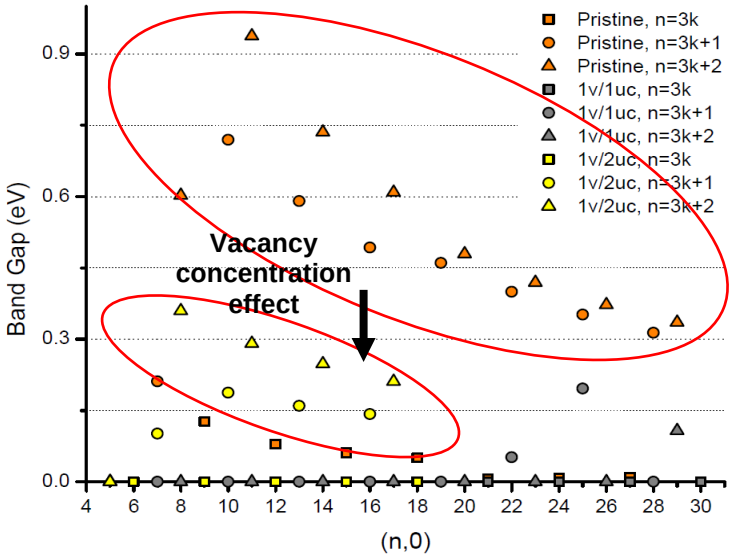

Figure 36. Comparison of the band gap as a function of chiral index of pristine and defective SWCNTs.

3.3.2 Effect of vacancy defects on DWCNTs

The structural relaxation of the (8,0)@(16,0) DWCNT can be observed in Figure 37a-b below. The outer tube, which is the one with the vacancy defect, is seen to rearrange its atomic structure in the vicinity of the vacancy. After the vacancy was generated, the three surrounding carbon atoms that were bonded to the atom removed become two-coordinated. However, after structural relaxation, two of the three atoms around the vacancy become

three-coordinated and form a pentagonal ring, while the third carbon atom remains two-coordinated and sticking up above the surface. This same behavior observed here for the outer tube in the DWCNT configuration is observed on all of the SWCNTs that were previously modeled and simulated with vacancy defects.

The effect on the electronic structure of the (8,0)@(16,0) DWCNT can be observed by plotting the band structure and density of states (DOS) from the data simulated using SIESTA. The band structure of the pristine DWCNT is shown below in Figure 38a, from which a band gap can be clearly appreciated. From the previous chapter, the s@s DWCNT configuration corresponds to the medium band gap region. In particular, the (8,0)@(16,0) DWCNT has a band gap of ~0.5 eV. The atomic rearrangement caused by the structural relaxation after the vacancy defect is introduced causes a change in the band structure as well. The band gap at the Γ point reduces by about half of its original value for the pristine DWCNT after structural relaxation of the defective tube (see Figure 38b).

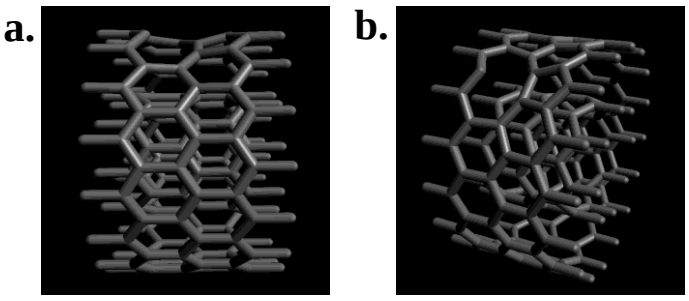

Figure 37. (8,0)@(16,0) DWCNT after structural relaxation and energy minimization in SIESTA.

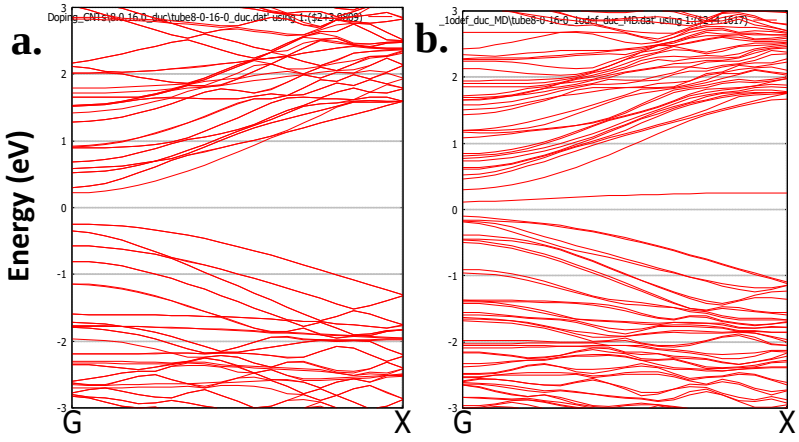

Figure 38. Band structure of the a) pristine (8,0)@(16,0) double-walled carbon nanotube and b) the same with a vacancy defect on the outer tube.

Additionally, the density of states also suffers alteration after the structural relaxation of the outer tube in the defective DWCNT. Figure 39a below shows the density of states of the pristine case. The DOS drops to zero at the fermi energy level, from which an energy gap may be inferred. In comparison, the DOS at the fermi energy level is nonzero (Figure 39b); the DOS in the vicinity of the fermi energy level is also modified to values slightly higher than those for the pristine DWCNT. This change signifies an increase in energy states near the fermi level that reduces the electronic band gap of the molecule, thus creating the possibility of electrons to transition from the valence to the conduction band with a smaller energy input.

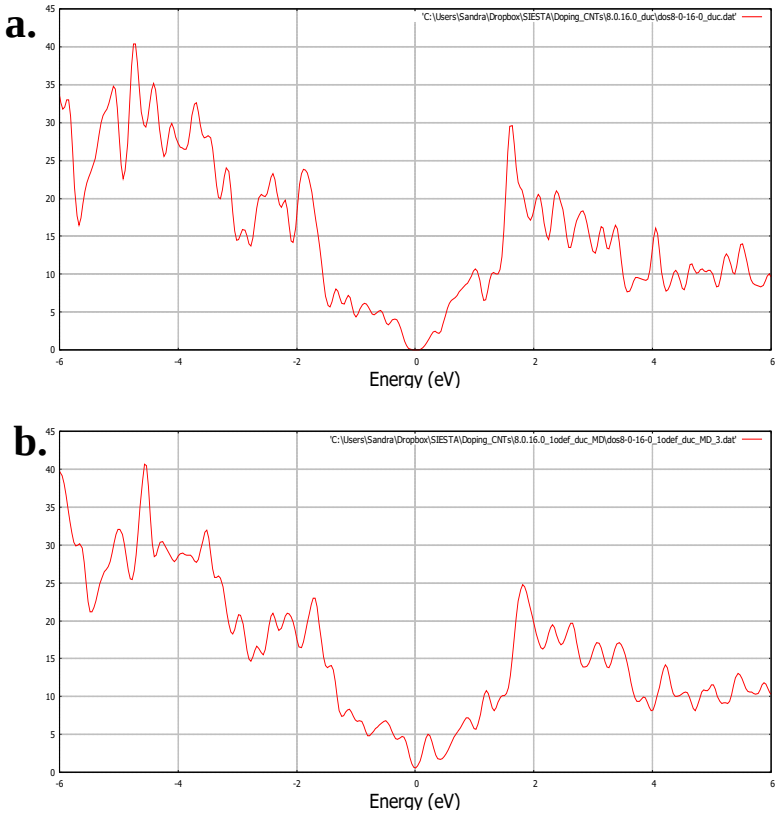

Figure 39. Density of states of the a) pristine (8,0)@(16,0) DWCNT and b) the same with a vacancy defecto n the outer tuve.

3.4 Conclusions

Introducing vacancy defects into the atomic structure of single-walled carbon nanotubes causes a rearrangement of the atoms upon relaxation that agrees well with previous theoretical and experimental results. Upon structure modification, a SWCNT becomes less stable energetically. This is shown by the increase in energy per atom with respect to a pristine SWCNT. Additionally, the electronic band structure also suffers modifications; in particular, the band gap is reduced when vacancy defects are introduced. For the case of 1v/2uc, the resulting band gaps simply shift down from their previous value for zigzag nanotube with chiral indices (n,0), $n = 3k+1$ and $n = 3k+2$ (k being an integer). For narrow band gap zigzag nanotubes with chiral index (n,0) for $n = 3k$, the band gap completely vanishes. Also, for the case of 1v/1uc, the band gap completely vanishes for all the zigzag SWCNTs, except for the (22,0), (25,0), and (29,0).

From this work we can see that adding vacancy defects to carbon nanotubes is one way to reduce the electronic band gap of zigzag CNTs. The reduction in band gap is dependent on vacancy concentration and chiral index. Vacancy defects can be introduced at low concentrations and cause a significant change in the electronic band gap. It can be envisioned that coupling of the interwall interaction (*Chapter 2*) and vacancy defects could be used to control the electronic band gap to a greater degree. This could be useful in applications that require band gap control, such as transistors. However, it is important to note that although the vacancy defects are able to modify the electronic band gap, they could have a negative effect on the conductance of individual CNTs, as has been shown previously for the case of armchair SWCNTs [75].

Finally, adding vacancy defects to zigzag SWCNTs (1-2% defect concentration) will create an average band gap lower than pristine SWCNTs and DWCNTs, assuming a uniform distribution of only zigzag CNTs.

3.5 Future Work

The study of vacancy defects undertaken in this work is limited to the study of the effect of vacancies on individual SWCNTs and on the outer tube of a DWCNTs. This type of study sheds light on the effect vacancies have on the electronic properties of carbon nanotubes, but it doesn't show exactly show how it would affect an CNT bundle with a certain diameter and chirality distribution. A larger-scale study would require a different methodology in order to be able to obtain results with current state-of-the-art computational resources.

A solution would be to use a multi-scale approach to the study of the electrical properties of CNT bundles with vacancy defects distributed at a certain concentration. In this approach, atomistic simulations can be used to obtain the electrical properties of individual carbon nanotubes with and without vacancy defects; knowing those properties, a finite element-like stochastic methodology can be used to obtain the electrical properties of a carbon nanotube network, in a similar fashion to the work done previously by the author of this work [76]. Such an approach would predict the electrical properties of a CNT bundle while at the same time making use of the electronic properties calculations obtained for each individual CNT at the atomic scale. Additionally, the same procedure could be used to move up the scale, from CNT bundles to a CNT wire. A stochastic finite element-like methodology could be employed that models the CNT bundles as a finite element that interacts with other bundles to form a wire; from which the electrical properties of a CNT wire could be obtained.

Additional to the proposed methodology outlined above, the properties of individual carbon nanotubes with different chiralities and number of vacancies need to be studied to obtain their electrical properties. Because of the limitations in the number of atoms when performing DFT simulations, studying CNTs with more atoms, as it is required for chiral CNTs with one unit cell or when studying zigzag and armchair CNTs with several unit cells, atomistic simulations may not always be the most suitable methodology. Instead it may be useful to follow the methodology outlined in the report by Domínguez-Rodríguez *et al.* [77] of an atomistic resistor model of SWCNTs for the calculation of the electrical resistance of a SWCNT.

Chapter 4

Effect of Iodine Doping on the Electronic Properties of Carbon Nanotubes

4.1 Introduction

Adsorption doping of iodine molecules has been shown to modify the properties of CNTs, including electronic structure and electrical resistance. Additionally, the effect on junction resistance has been studied for transition metal dopants. The changes in properties are significant and also serve as motivation to engage in the study of the causes, dopant-substrate interaction, charge transfer, and so on, in order to seek the possibility of learning to tune the macroscopic properties through the modification of the nanostructure.

4.1.1 Effect on the Electronic Structure

Even though the effect of adsorption doping on the electronic structure of carbon nanotubes has been amply reported [78–82], to our knowledge, not much work has been done with regards to the effect of iodine adsorption doping on the electronic structure of carbon nanotubes. This is not to say that no other works have studied iodine doping on CNTs, however, such studies focused mainly on the interaction between dopant and substrate and not on the effect of such interaction on the electronic structure.

One of the studies that undertakes this question is that of Choi *et al.* [30]. They performed first-principles density functional theory calculations, under LDA Ceperley-Alder flavor functional, of a semiconducting (10,0) CNT with an iodine trimer (I_3) inside. First, the configuration was allowed to relax structurally, then they constructed simulated scanning tunneling microscopy (STS) data with the projected density of states (PDOS) along the CNT axis. Their results – via Mulliken population analysis – indicate that charge transfer occurs even after structural relaxation. The charge transfer brings about acceptor-like states in the semiconducting CNT above the valence band, as shown in Figure 40. These states appear spatially in the region where the iodine trimer is located and energetically in the band gap, above the valence band. Such results suggest that the band gap may be reduced due to the charge transfer from the CNT to the iodine trimer, but only in the spatial region near the encapsulated dopant, as the acceptor-like states are bound to the iodine trimer and not uniformly distributed over the entire system.

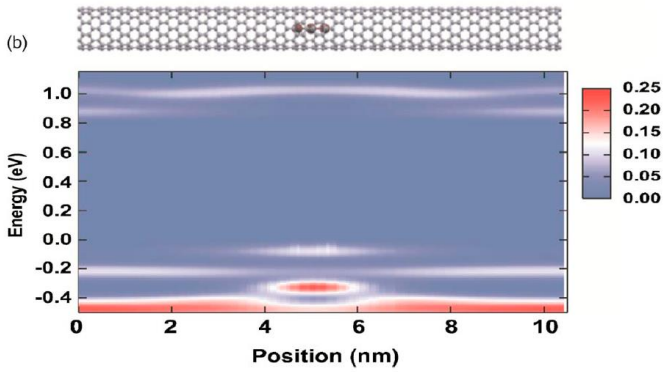

Figure 40. Two-dimensional map of simulated STS of a (10,0) CNT encapsulating an iodine trimer (I_3) and its model structure. The Fermi level is set to zero [30].

Because the purpose of the work by Choi *et al.* was to observe the effect of a single iodine trimer, in their study the authors use a large unit cell, containing between 800 – 1000 carbon atoms and one iodine trimer, which helps diminish the interaction between the neighboring images due to the periodic boundary conditions in the direction along the tube axis. It should be noted that studies of doping with a smaller unit cell do allow for the interaction of the dopant with its neighboring images; doing so simulates the effect of a higher dopant coverage over a continuous carbon nanotube.

4.1.2 Effect on Junction Resistance

Not only does doping has the potential to modify the electronic structure of the host molecule but also, when dealing with carbon nanotube networks, the interaction between tubes plays an important role on the electron transport from one tube to another. This interaction can be modified by attaching single molecules between two carbon nanotubes' ends [83,84] or by sidewall functionalization [85]. Ultimately, attaching a molecule between tubes creates a junction for electronic transport by reducing the role of electron tunneling as the only mechanism of transport. However, special attention must be put when designing CNT junctions as many functionalized SWCNT networks have shown reduction in electrical conductivity by 2 to 3 orders of magnitude due to the interruption of π-conjugation in the tubes, among other effects [85].

The study by Li & Mazari [85] using first-principles calculations gives an insight into the effect of transition metals on the junction quantum conductance. Figure 41 shows the

quantum conductance near the Fermi level for a (5,5)-CNT junction connected by a 3d transition metal. For the same junction, the transition metal was removed from the configuration to observe the conductance contribution of electron tunneling and is shown in the figure as “no TM”. An increase in conductance is shown for all the 3d transition metals on the figure below. A few of the transition metal junctions, such as Ti, V, and Cr, show quantum conductance of about 0.8 G_0 (quantum conductance of a pristine armchair is 2 G_0) near the Fermi level, which is an dramatic improvement which respect to the essentially zero conductance without any junction.

With respect to the effect of junction formation, orbital mixing and charge transfer by iodine adsorption, additional studies must be undertaken to comprehend the physicochemical mechanisms associated with it. Some challenges remain such as: the effect of an encapsulated trimer on a metallic CNT, and also the relation to diameter and curvature conditions; the effect of iodine dimer or trimer adsorbed in different surface positions and for different tube chiralities and diameters and with regards to the electronic structure of the CNT as well as its role as a sidewall junction; and also the effect on the electronic structure of iodine doping in the interstitial region of CNT bundles.

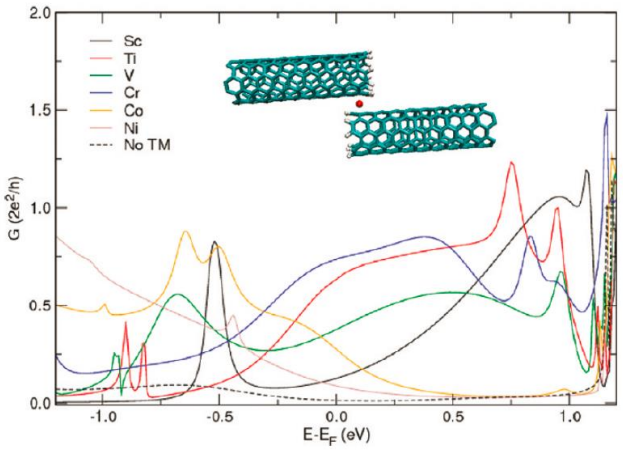

Figure 41. Quantum conductance near the Fermi level of a (5,5)-CNT junction connected by a 3d transition metal [85].

4.1.3 Effect on Electrical Resistance

Only a few publications were able to measure the electrical resistance and its change due to dopant adsorption; nevertheless, the different doping processes all showed a significant decrease in electrical resistivity of their samples from the iodine dopant adsorption. Using molten iodine to dope SWCNTs, the electrical resistance (measured by 4-probe) was seen to decrease over the entire temperature range of 10 – 300 K, with a reduction of a factor of ~40 at T = 300 K upon saturation doping [25]. The resistivity (or conductivity) was not calculated for their samples. Two reports [26,86] that doped their samples using an iodine-ethanol solutions measured the change in electrical conductivity. A dependence on temperature was observed [26] in the 20 – 300 K range when measuring conductivity with a four-probe method, and an increase of 15 % after doping the sample of SWCNTs with I_2. Within the temperature range used, the resistivity measurements are ~10^{-2} Ω-cm. Khoerunnisa *et al.* [86] also performed four-probe measurements, and found a decrease in resistivity by a factor of 10 when doping SWCNHs with iodine-ethanol solution. The value of resistivity at a maximum coverage of 0.18 was measured at ~$17x10^{-5}$ Ω-cm, and showed a clear dependence on iodine coverage. Such an improvement over the previous solution doping of SWCNTs can be in part explained by the oxidation step used to open the SWCNH's ends to allow adsorption inside the tubes.

Iodination from gaseous phase of SWCNTs also brings about a change in electrical resistance over the temperature range of 20 – 300 K. The resistance of pristine films is seen to decrease by one order of magnitude at 300 K [27]. For the case of DWCNT ropes doped with iodine gas, the decrease in resistivity is also seen to be significant. From their data [28] it is not possible to estimate the exact change in resistivity; however, we may use the minimum values given for raw and doped cables of ~$5x10^{-5}$ Ω-cm and ~$1.5x10^{-5}$ Ω-cm, respectively. This supposes a reduction by a factor of ~3 in resistivity. It should also be noted also that doping the DWCNT cables has shown to improve the temperature stability of the cable in the range of 200 – 400 K, with a variation in resistance at 200 and 400 K of ±9 % with respect to the value at 300 K, as seen in Figure 42. For copper the variation for the same temperature range is ±43 %.

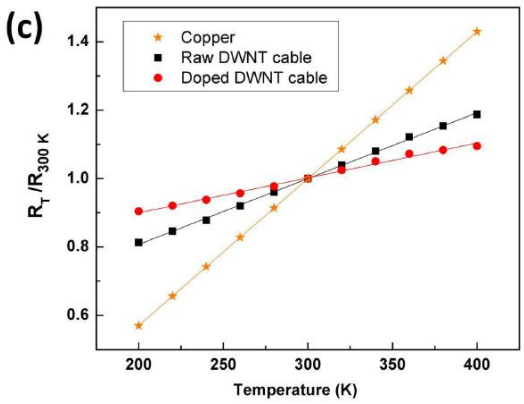

Figure 42. Relative resistance as a function of temperature [28].

4.1.4 Iodine Species

First to note is the nature of iodine molecules for each type of process. According to [87], the molecular structure of iodine depends on its state, whether as a solute in a solvent, molten or gaseous. Iodine molecules in molten iodine tend to dissociate into highly reactive iodinium (I^+) and polyiodide $(I_3)^-$ species, while iodine gas contains only nondissociated iodine molecules which are less chemically active.

The earliest works with iodine doping on CNT substrates used molten iodine by immersing SWCNTs, DWCNTS, or MWCNTs into it for several hours [25,87,88] or several days [89,90] at 140 °C and inside an evacuated quartz tube. Grigorian *et al.* [25] found linear iodine chains in the interstitial channels of the SWCNT rope by Z-contrast scanning transmission electron microscopy (STEM). Raman scattering confirmed the existence of iodine molecular chains and found that the Raman peaks belonged to $(I_5)^-$ and $(I_3)^-$ linear chains complexes. No peaks were observed for $(I_2)^0$ molecule in their Raman studies; however, it is important to note that the SWCNT mats were heated at 60-80 °C for 2-4 hours after immersion in molten iodine in order to remove physisorbed species, which could had removed other species that were weakly adsorbed on the surface or grooves of the CNT ropes.

Fan *et al.* [87] followed the same doping procedure from [25] and were able to observe charged polyiodide chains inside SWCNTs by Z-contrast STEM. They also found that the chains have a helical structure in three dimensions with a periodicity adapted to the

nanotube wall chirality, and even a double helix was observed (similar to the structure model of Figure 43). Additionally, first-principles calculations showed that the interatomic spacing of curved graphene sheets better match the preferred I-I spacing in iodine chains, contrary to the case of the interatomic spacing of I_2 molecule, which does not correlate with any spacing of basal plane of graphite. From their computational model they were able to suppose the feasibility of incorporating up to five spirals of iodine with a 5 nm period inside a SWCNT. Another of the studies [91] dealing with SWCNTs also followed the doping process previously developed [25], and via Raman spectroscopy determined the formation of $(I_5)^-$ and $(I_3)^-$ chains. This was later confirmed from x-ray and neutron experiments and numerical calculations.

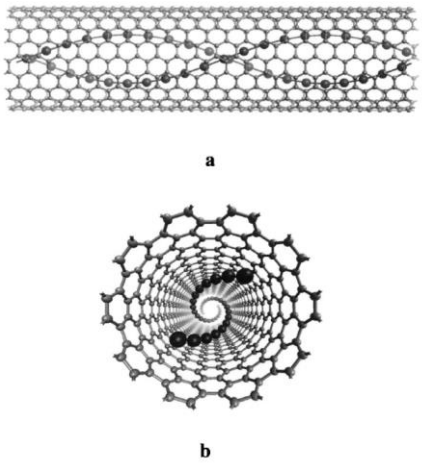

Figure 43. Structure model obtained by extrapolating a 5 nm helix used for computational calculations to a full scale (10,10) nanotube, (a) side view and (b) top view [87].

A Raman study [88] of doped DWCNTs with molten iodine also showed the existence of Raman peaks previously [92] assigned as resonant modes of polyiodide anions, mainly $(I_3)^-$ and $(I_5)^-$. For the case of MWCNTs, two studies [89,90] have shown similar results. The work of Zhou *et al.* [89] intercalated MWCNTs by immersing them into molten iodine inside an evacuated quartz tube at a temperature of 140 °C for about one week. Previously, the MWNCTs had been oxidized in air at 700 °C for about 1 h to open ended nanotubes, which was confirmed by scanning electron microscopy (SEM) and transmission electron microscopy (TEM). The comparison of Raman spectra led to attribute the peaks found to charged $(I_5)^-$ and $(I_3)^-$ linear chain complexes. Michel *et al.* [90] also immersed MWCNTs into molten iodine for several days. Raman spectra of their doped DWCNTs and MWCNTs

showed peaks generally attributed to the presence of $(I_n)^-$ chains, although only the innermost and outermost surfaces were intercalated. However, their X-ray absorption spectroscopy (XAS) experiments found I_2 molecules, which were assumed to be adsorbed on the sample's surface. After being characterized, these neutral iodine molecules were washed away with ethanol, which was confirmed by XAS data analysis. The coexistence of both $(I_n)^-$ chains and I_2 molecules is possible according to its phase diagram. Under atmospheric conditions, iodine is in liquid phase from about 114 °C to 184 °C, and the liquid-gas boundary in this temperature range can be approximated by a linear function with a positive slope. Therefore, under evacuated conditions and 140 °C temperature, it's possible for liquid and gaseous phases to coexist for a specific set of pressure and temperature parameters.

The previous experimental results suggest that polyiodide chains dominate the doping process under molten iodine doping conditions. More recent iodine doping experiments [26,86] have used adsorption from solution (ethanol), which was seen as a promising method [26] due to its simplicity and efficiency [93,94]. Hayakawa *et al.* [26] used adsorption from solution by dissolving iodine in an ethanol solution at different concentrations (0.05-50 mg/L) at room temperature, afterwards adding SWCNTs to the solution and ultrasonically dispersing them. In their case, x-ray photoelectron spectroscopy (XPS) analysis of the doped samples found evidence of I_2 molecules adsorbed on the surface of SWCNTs, specifically on the conjugated π-electron system through the charge transfer interaction.

Iodine doping by gaseous state has also been done experimentally. One of the early works [95] used iodine gas at 320 K (46.86 °C) inside a quartz vacuum vessel; however, the authors did not characterize the resultant iodine species. Kissell *et al.* [96] doped the SWCNT sample by sublimation of iodine at about 100 °C for 1 h inside a closed vessel. XPS showed I_2 molecules, which indicates that I_2 did not react with SWCNT to form C-I bonds, but it's adsorbed by the substrate.

Jung *et al.* [97] doped SWCNTs via vapor-phase reaction of the iodine at 250 °C for 3 days with the substrate inside an evacuated quartz tube. According to their Raman studies, iodine species in their I-SWCNT sample were not stabilized as polyiodide chain molecules. Also, they argue against a previous report [25] claiming the existence of negatively charged

polyiodide ions in I-SWCNT via molten iodine used I 3d XPS analysis, which is not a suitable tool for probing the existence of partially-charged polyiodide chains. Instead, the peak attributed to the negatively charged polyiodide chains is within those accepted for neutral I_2, according to Ref. [96]. However, the doping process cited [96] is via sublimation of the iodine as opposed to molten iodine doping as used by Grigorian *et al.* [25]*;* and, as previously mentioned in another work [87], highly reactive iodinium (I^+) and polyiodide $(I_3)^-$ species are found in molten iodine, while iodine gas contains only nondissociated iodine molecules. Such difference in iodine phase during the doping process could be one of the reasons of the dispute over the actual iodine species. Another work that has also mistakenly assumed that the iodine species deposited on the CNTs via vapor phase process are the same as those from molten iodine is that of Zhao *et al.* [28]. Even though they observed the iodine molecules via Gatan imaging filter elemental mappings, the iodine species was not characterized. Tonkikh *et al.* [27] were able to observe the iodine molecules inside the SWCNTs by high-resolution transmission electron microscope (HRTEM) and assumed, from theoretical calculations [98], to be polyiodide chains.

Finally, it is worth mentioning the work by Guan *et al.* [99], in which they studied iodine doping of SWCNT by transmission electron microscope (TEM). Their report does not specifies the nature of the iodine phase during the doping process. It is only mentioned that a mixture of SWCNT bulk powder and iodine in an evacuated glass tube were heated at 150 °C for 24 h, and washed with ethanol in order to remove excess iodine remaining on the SWCNT surface. Their TEM imaging revealed single, double and triple helical iodine chains, with a non-constant helical pitch inside the SWCNTs; the number of chains was found to depend on the host's diameter. Additionally, no positive correlation was found between the helical structure of iodine atomic chains and the nanotube helicity, which is contrary to previous theoretical predictions [87]; and no four or more iodine chains were successfully produced in this experiment.

4.1.5 Iodine Adsorption Sites

From the aforementioned investigations, we may also find information regarding the location of the iodine dopants. From the experiments that used molten iodine as a doping process, continuous, linear iodine chains were determined to be located in the interstitial

channels between nanotubes and acting as a "chemical wedge" [25]. Other works [87] have found the polyiodide chains located inside SWCNTs (Figure 43), although not all tubes were intercalated, which suggests substantial iodine is also incorporated in the interstitial positions between tubes in a bundle. Zhou *et al.* [89] found polyiodide chains inside the innermost tube of MWCNTs, and did not find these chains intercalated into the graphene multishells. For the case of DWCNTs doped with molten iodine, it was found [88] that the polyiodide anions are adsorbed on the surface of the outer tubes of the DWCNTs. Similarly, a more recent study [90] found no intercalation of iodine with DWCNTs and MWCNTs when doped with molten iodine, only weak surface adsorption. Finally, the study by Bendiab *et al.* [91] using x-ray and neutron diffraction investigations along with a numerical study of their patterns determined that after doping with molten iodine, the polyiodide anions are mainly located inside the tubes, but some are also inserted into the interstitial channels of the triangular lattice, as shown in Figure 44.

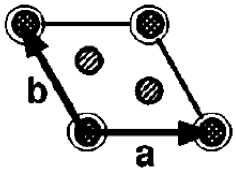

Figure 44. The iodine chains are represented by filled cylinders inside the triangular lattice as indicated in the unit-cell drawing [91].

Dripping a solution of iodine and ethanol onto carbon substrates may also lead to different adsorption sites including internal tubes spaces and interstitial spaces for the case of SWCNH [86], or interstitial pores in SWCNT bundles [26]. From the results of doping with iodine in gaseous phase, one of the reports [96] claims that variable-temperature XPS found that the only positive species that were released when heating from 200-800 °C were $(I_2)^+$ and I^+ (surface-adsorbed species), and an atomic percent of iodine remaining at 400 °C, which is consistent with internally-loaded I_2. The work by Jung *et al.* [97] found from powder X-ray diffraction (PXRD) analysis that the iodine intercalation commonly suppresses diffraction peaks corresponding to the hexagonal lattice of the pristine SWCNTs, indicant that the iodine molecules deposited via sublimation are intercalated in the interstitial channels, acting as a chemical wedge. Surface adsorption of iodine in gaseous phase onto DWCNTs is claimed by Zhao *et al.* [28], in which Gatan imaging filter

(GIF) elemental mappings for carbon and iodine reveled the iodine is uniformly present within the cable, presumably homogeneously adsorbed on the surface of DWCNTs (Figure 45). The experiments of Tonkikh *et al.* [27], in which sublimated iodine was mixed with carbon nanotube substrate, found iodine species inside SWCNTs from their HRTEM images; however, their samples were thermally cleaned during 4 h after iodination, which helped eliminate surface adsorbed iodine.

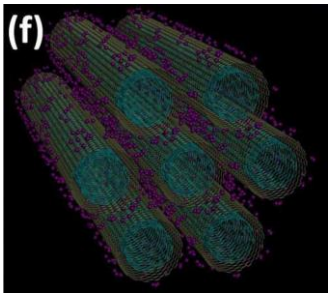

Figure 45. A schematic illustrating the speculated model for iodine doped DWCNT bundle. The iodine atoms are decorating the surface of the nanotubes [28].

Finally, the TEM images of Guan *et al.* [99] shows three scenarios for the location of iodine chains after the iodine doping process was carried out according to the conditions specified in their article: the single iodine chain of Figure 46a is inside a SWCNT with a diameter of about 1.05 ± 0.05 nm; a SWCNT with a 1.30 ± 0.05 nm diameter contains two helical chains of iodine atoms, as shown in Figure 46b; and a triple iodine chain in a SWCNT with diameter of about 1.40 ± 0.05 nm is shown in Figure 46c.

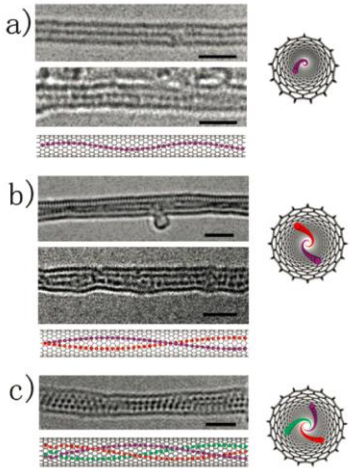

Figure 46. HR-TEM images of the atomic chains sheathed with SWCNTs and their schematic illustrations. (a) A single iodine chain. (b) A double iodine chain. (c) A triple iodine chain [99].

4.1.6 Charge Transfer

Raman studies [25] of the doped SWCNTs via molten iodine phase showed a sizable up-shift of some modes in the spectra, which was correlated with the doping level and found to be reversible after de-intercalation. The up-shift induced by iodine doping was attributed to electron transfer from the SWCNTs to the iodine chains, $(I_3)^-$ and $(I_5)^-$. An analogy was also made to acceptor-intercalated graphite compounds, in which a transfer of carbon π-electrons to the intercalant is expected to induce a contraction of the hexagonal rings along the cylindrical wall of the SWCNTs, up-shifting the observed tangential mode frequencies. Another study of iodine doping (molten phase) of SWCNTs [87] using Raman spectroscopy found a charge transfer to the iodine to be typically around 0.33 eV/iodine or 0.2 eV/iodine, which corresponds to $(I_3)^-$ and $(I_5)^-$ species. Additional to their experimental findings, first-principles calculations of iodine chains over a bent graphene sheet led them to conclude that charge transfer from the tube wall to the iodine chain stabilizes the I chains. Bendiab *et al.* [91] arrived at a similar conclusion from their studies of iodine doped (molten phase) SWCNTs: characterization of the samples by Raman spectroscopy confirms the charge transfer between CNTs and polyiodide chains.

The reversible intercalation of iodine with CNTs via molten phase doping has also been shown in the case of MWCNTs, along with the characterization of the iodine species in the form of linear $(I_3)^-$ and $(I_5)^-$ molecules intercalated into the innermost tubes of different diameters [89]. The existence of these iodine chains shows an exchange of electrons with the inner tube walls. For the case of Raman spectroscopy studies [88] of only DWCNTs doped with molten iodine, it was found that only the outer tubes are involved in charge transfer. This seems to be in contradiction to the previous study [89] on MWCNTs in which the same doping process was followed; however, an oxidation step was also done in the case of Zhou *et al.* [89] for the purpose of opening ended nanotubes. Perhaps adding an oxidation step before doping of DWCNTs could also lead to a charge transfer from the inner tube, as was the case with the MWCNTs. Finally, Michel *et al.* [90] also found a weak interaction (surface adsorption) between iodine and DWCNTs and MWCTNs after being doped with molten iodine during several days to achieve saturation. In their experiments,

SWCNTs were found to have stronger interactions with the iodine chains, which were able to penetrate the inner cavity of SWCNTs.

SWCNTs doped from iodine-ethanol solution are also observed to have charge transfer. According to their Raman spectroscopy and XPS studies, the I_2 molecules are adsorbed on the conjugated π-electron system through charge-transfer interaction [26]. Khoerunnisa *et al.* [86] also arrives at the conclusion that their SWCNHs have experienced charge transfer with the I_2 molecule, however, this conclusion is inferred from the increase in electrical conductivity of their sample. Neither of these studies was able to characterize quantitatively the charge transfer between substrate and dopant, and did not extend to MWCNTs.

Doping SWCNTs with gaseous phase iodine was shown to achieve even the tuning of the electron transfer so that the Fermi level (E_F) coincides with a specific band of the density of states (DOS) of semiconducting and metallic nanotubes [95]. In this study, the charge transfer was found to be reversible for the case of I_2 interacting with SWCNTs, and it affects predominantly the electronic states of semiconducting SWCNTs by filling specific bands. Tonkikh *et al.* [27] also found some changes in the DOS due to iodine doping in gaseous form. From their ultra-violet (UV) via visible (vis) to near infrared (NIR) measurements it was concluded that a strong electron acceptor such as iodine intercalated with SWCNTs induced a charge transfer from nanotubes to the polyiodide species formed inside the tubes.

The previous studies are in contrast with another work [96] in which SWCNTs doped with gaseous iodine are seen to liberate $(I_2)^+$ and I^+ during variable-temperature XPS, implying a possible charge transfer from the dopant to the SWCNTs. I L-edge X-ray absorption near-edge structure (XANES) analysis was used to quantify the charge transfer during gaseous-phase iodine doping of SWCNTs. This study [97] found that a small amount of electrons (0.08-0.1 e^- per iodine) is transferred from iodine to the SWCNT. This is explained by the lower electronegativity of iodine, which lifts its lowest unoccupied molecular orbital (LUMO) above the Fermi level or valence band positions of the SWCNT, therefore preventing the SWCNT from donating electrons to the iodine. Instead, an increase in the energy of the highest occupied molecular orbital of iodine induces electron transfer from the iodine to the SWCNT. Furthermore, the author explains that the oxidation of iodine

enhances the matching of bonds by shortening the I-I bonds due to the decrease in electron density in antibonding π^* (I 5p). This study concludes that iodine acts as a weak electron donor for SWCNTs, contrary to the case of CNTs doped via molten iodine and even some of the studies that used gaseous iodine in their doping process [27,95].

The only case of MWCNTs being doped with iodine in gaseous phase is the work of Zhao *et al.* [28]. From their experimental work, they found that gaseous-phase iodine doping of DWCNTs creates a change in inter-layer spacing via X-ray diffraction spectra, which could be a direct indication of charge transfer and covalent bond formation [28]. Nevertheless, the amount of charge transfer was not quantified in the aforementioned experimental analysis.

It's also interesting to study the interaction of halogen dopants with carbon nanotube substrates using computational calculations from density functional theory (DFT). According to a computational study by Ghosh *et al.* [29], the adsorption energy of an I_2 molecule on a (5,5) and (8,0) CNTs is 1.09 and 1.54 eV, respectively, which is in the order of physisorption. They also found a Fermi energy shift upon the adsorption of the halogen dopant and that follows the trend of the electron donating capability of the halogen species, with I_2 being greater than IBr, Br_2, and ICl molecules. This is explained by the fact that as electrons are added to the conduction band, there should be an upward shift of the Fermi level. Therefore, I_2 having less ionization energy, can donate more electrons to the nanotube and shift the Fermi energy upward. Another result of this study worth mentioning is the trend found for adsorption energy, which was found to increase when going from semiconducting to semi-metal and to metallic CNTs. The other computational study already mentioned in this document also found a charge transfer exists by the dopant to the CNT, in this case, an iodine trimer encapsulated inside a (5,5) metallic armchair nanotube.

Additional computational calculations must be undertaken to understand charge transfer between iodine dimers and other type of CNTs.

4.1.7 Dopant Concentration

A few of the past reports on iodine doping included the measurement of the iodine concentration, or surface coverage. Some report an average composition close to IC_{12} from weight uptake [25,91] and TGA experiments [25], which is about 7.7 % atomic ratio. Fan *et*

al. [87] takes this further and explores possible iodine concentrations based on their experimental observations with high-resolution Z-contrast imaging. Two continuous strands of iodine with a 5 nm period would give a composition of IC_{20}, and incorporating up to five spirals of iodine with the same period would give a composition of IC_8. A pair of spirals with a shorter period of 1.5 nm would have a concentration of IC_{15}. These possible compositions based on different helical structures average to the concentration measured before [25], however, both of the experiments aforementioned removed the physisorbed surface iodine by heating the sample. Also from reported [89] TGA experiments on molten iodine doped MWCNTs, the composition was estimated to be IC_{200}, for an atomic ratio of about 0.5 %. The significant reduction in atomic ratio with respect to the two previous study is because MWCNTs can only intercalate iodine chains in the innermost tube (the sample was also heated to remove physisorbed surface iodine).

The concentration of iodine after doping of CNTs with an iodine-ethanol solution was characterized as a surface coverage. The adsorption isotherm of I_2 on SWCNTs was found to be Langmuirian. At a saturated concentration, the surface coverage was estimated at 0.06 assuming a single molecular adsorption of I_2, which was found to be located in the interstitial pores of the CNT bundle. A much higher surface coverage, also measured at a saturated adsorption condition, was found to be 0.18, for the case of SWCNHs doped from a liquid solution of iodine and ethanol. The increase in coverage can be explained by the fact that the tubes were opened before adsorption by oxidation at 823 K in Ar/O_2 atmosphere [86].

From the work of Kissell *et al.* [96], their XPS analysis showed an atomic ratio of 5.3 % iodine (36 wt. %) using gaseous phase doping. After a process in which most of the weakly adsorbed surface iodine was removed, the atomic ratio was reduced to 2.8 % (22 wt. %). A value of 3.3 % atomic ratio after gaseous phase doping was obtained by Zhao *et al.* [28], and reduced to 2.1 % atomic ratio after washing and sonicating in ethanol, which is similar to the value obtained by Kissell *et al.* [96] and mentioned above.

4.2 Methodology

In general, the study of the iodine doping was done by combining density functional theory and molecular dynamics methods. DFT was used to obtain the interaction energy between iodine atoms, and between carbon and iodine; and also to obtain electronic band structure calculations. Molecular dynamics was used to study the interaction of iodine with carbon nanotubes at a larger scale (more than 100 atoms) and for many iterations (more than 1000 runs).

4.2.1 Convergence Tests

Convergence tests were carried out to find the optimal parameters for the DFT simulations of single-walled carbon nanotubes, as explained in previous chapters. Separate convergence tests were carried out for the study of iodine-iodine interaction. The converged parameters are shown in Table 8 along with the final reference value. Convergence criterion used was 1 meV/atom for all parameters except for the value of PAO.EnergyShift, which was converged to a 10 meV/atom difference.

Table 8. Converged parameters used in the DFT simulations of iodine.

Parameter	Converged Value	Final Value
PAO.EnergyShift	0.0001 Ry	0.00005 Ry
MD.MaxForceTol	40 meV/Å	1 meV/Å
MeshCutoff	100 Ry	1000 Ry
Electronic Temperature	300 K	1000 K
DM.Tolerance	$1x10^{-4}$	$1x10^{-6}$
LatticeConstant	15 Å	40 Å

4.2.2 Interaction Potentials

Density functional theory simulations were used to study the atomic and molecular interactions of iodine and carbon. First, the interaction between two iodine atoms was studied in order to develop an interatomic potential. For this purpose, the total energy of a single iodine atom inside a simulation box was calculated first, then the total energy of two iodine atoms alone inside a simulation box was calculated at several separation distances. The iodine atoms were placed at a separations distance of 10 or more angstrom, then the separation was reduced in steps of 1 Å or less (Figure 47), depending on the precision

needed within a given region of the interaction energy data, and the total energy of the systems was calculated. The interaction energy, E_i, was determined as following,

$$E_i = E_d - 2E_s \tag{4.1}$$

where E_d is the total energy of the diatomic system and E_s is the total energy of a single iodine atom.

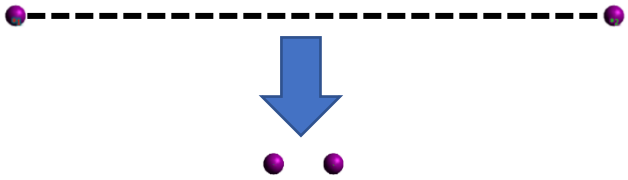

Figure 47. The distance between two iodine atoms was changed to calculate the interaction energy.

The interaction energy as a function of the distance between the two iodine atoms is shown below in Figure 48 as the data points labeled "y vs. x". In order to find a curve fit to the data, a Morse potential equation was used, such that,

$$V(R) = D_e(1 - e^{-\beta(R-R_e)}) \tag{4.2}$$

for the interaction energy V as a function of the distance, R, where R_e is the equilibrium distance, D_e is the interaction energy at the equilibrium distance (or the energy well depth), and β is a fitting parameter. Using the cftool utility in Matlab, the data points were fitted using equation (4.2), for which the β parameter was found to be 1.432 (1.421, 1.443) 95% confidence interval, with a value of R^2 of 0.998. All the values for the Morse potential are shown in the table below:

Table 9. Parameters for I-I interaction using the Morse potential of equation (4.2).

Parameter	Value
D_e	3.092 eV
β	1.432
R_e	2.578 Å
Cutoff	8 Å

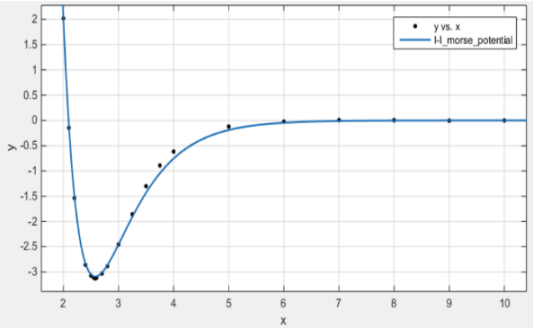

Figure 48. Data fit using Morse potential of equation (4.2).

The development of a potential for the interaction between an iodine and a carbon atom followed a different process. The pairwise interaction between iodine and carbon within a diatomic iodine molecule and a carbon nanotube is affected by the surrounding atoms in the system. In order to capture the effect of other atoms in the pairwise interacting potential between iodine and carbon, the distance between a diatomic iodine molecule and a (8,0) SWCNT was varied and the total energy was calculated at each separation. Four unit cells of the (8,0) CNT per diatomic iodine were used in this case, as shown in Figure 49.

Similar to equation (4.1), the interaction energy was calculated using the following equation,

$$E_i = E_{sys} - (E_{CNT} + E_d) \tag{4.3}$$

where E_{sys} is the total energy of the systems composed of the (8,0) CNT and the diatomic iodine molecule, E_{CNT} is the total energy of the (8,0) CNT alone, and E_d is the total energy of the diatomic iodine molecule.

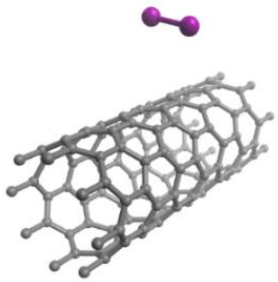

Figure 49. Unit cell used for diatomic iodine adsorption study.

The data obtained using the aforementioned process was fitted using a 10-5 Lennard-Jones potential, such that,

$$V(R) = 4\varepsilon\left(\left(\frac{\sigma}{R}\right)^{10} - \left(\frac{\sigma}{R}\right)^{5}\right) \quad (4.4)$$

where R is the distance between the CNT and the iodine molecule, ε is the depth of the potential well, and σ is the distance at which the interaction potential is equal to zero. The curve fitting was done using cftool in Matlab, for which a value of R^2 of 0.98 was obtained. This curve is shown below (Figure 50) with the legend name I_2-CNT interaction.

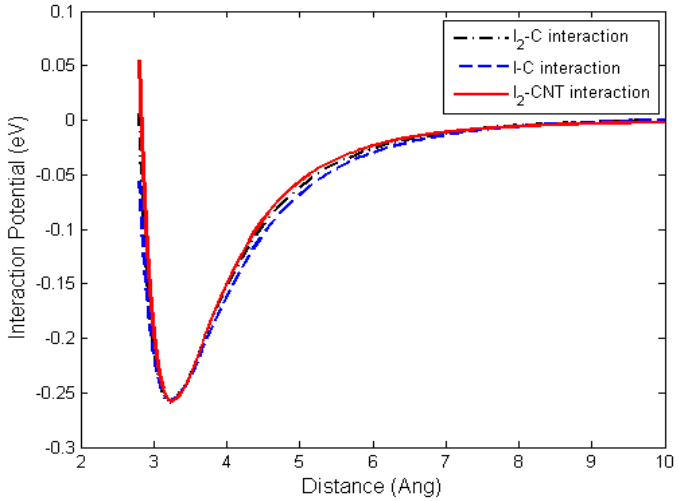

Figure 50. Data fit using Lennard-Jones equation of the interaction of I_2-CNT (solid red line), I_2-C (black dotdash line), and I-C (blue dashed line).

In order to implement the interaction potential in a molecular dynamics environment, a pairwise interaction needed to be determined. This was done by using an equation proposed by Allen *et al.* [100], which assumes that the sum of all the pairwise interactions within a cutoff are equal to the global coarse-grained interaction, such that,

$$V_{AB}(R) = \sum_{i\epsilon A}\sum_{i\epsilon B} v(r_{ij}) \quad (4.5)$$

where *v(r)* is the pairwise interaction energy between atoms *i* and *j* as a function of the distance *r* between them, and summed over all the pairwise interactions between atoms in molecules *A* and *B*. This double sum is equal to the coarse-grained interaction noted by the left-hand side of the equation; where $V_{AB}(R)$ is the interaction energy between molecules *A* and *B*. In our case these two molecules are the (8,0) CNT and the diatomic iodine.

Using equation (4.5), an interaction potential can be formulated first for the interaction between the diatomic iodine molecule and each carbon atom in the carbon nanotube. The

data was fitted to a 12-6 Lennard-Jones potential with a cutoff of 10 Å, and the parameters σ and ε where found using cftool in Matlab, and it is shown above in Figure 50 (black dotdash line). Similarly, the true pairwise interaction potential for the I-C interaction energy was determined using equation (4.5), a 12-6 Lennard Jones potential for the pairwise interaction energy of the right-hand side of equation (4.5), and a cutoff of 10 Å, such that,

$$V(R) = 4\varepsilon\left(\left(\frac{\sigma}{R}\right)^{12} - \left(\frac{\sigma}{R}\right)^{6}\right) \tag{4.6}$$

where the variables in equation (4.6) are the same as explained above in equation (4.4). For each distance between the diatomic iodine molecule and the (8,0) carbon nanotube, the total interaction energy was calculated for each pairwise interaction between iodine and carbon atoms and plotted in Figure 50 (blue dashed line) with the legend "I-C interaction". As shown in Figure 50, there is a close agreement between the coarse-grained interaction energy calculated directly from the DFT simulations and the pairwise 12-6 Lennard-Jones interaction potential developed using equation (4.6). The parameters of the pairwise C-I interaction are summarized in the table below:

Table 10. Parameters for I-C interaction using the Lennard-Jones potential of equation (4.6).

Parameter	Value
ε	0.0109 eV
σ	3.4 Å
Cutoff	10 Å

Finally, the interaction between the carbon atoms was modeled using the reax/c pairwise interaction potential, which computes the ReaxFF potential of van Duin, Goddard and co-workers. ReaxFF uses distance-dependent bond-order functions to represent the contributions of chemical bonding to the potential energy. There is more than one version of ReaxFF. The version implemented in LAMMPS uses the functional forms documented in the supplemental information of the following paper [101]. The version integrated into LAMMPS matches the most up-to-date version of ReaxFF as of summer 2010 [102].

Some testing was performed in order to verify that the parameters found for the I-I interaction using the Morse potential and for the C-I interaction using the Lennard-Jones potential provided results that are comparable to simulated and experimental values obtained previously. The diatomic iodine molecule was positioned on the surface of a (8,0) SWCNT on top of a carbon atom chosen arbitrarily, but kept as the same location in LAMMPS and SIESTA. In both simulated environments, the system was energetically minimized under a relaxation criterion. Table 11 shows the distances between the iodine atoms and also between the diatomic iodine molecule and the surface of the (8,0) carbon nanotube for both simulations. It can be seen that there is agreement (2% difference or less) between the distances that resulted using a DFT-LDA simulation and a MD simulation with interaction potentials derived from DFT-LDA.

Table 11. Comparison of results obtained using LAMMPS and SIESTA for the I_2-CNT interaction.

Distance at arbitrary location	LAMMPS	SIESTA
I-I dist (Å)	2.58	2.57
I_2-CNT dist (Å)	3.32	3.39

Also, the results provided from LAMMPS simulations were tested to assess their precision. First, an arbitrary location near the tube surface and with the parameter from Table 11 in mind was chosen and the I_2-CNT system relaxed in LAMMPS. From this relaxation, an equilibrium position was determined. Next step, the I_2-CNT and I-I distances were increased by 10% of their equilibrium position and the system was again relaxed. Similarly, the I_2-CNT and I-I distances were decreased by 10% of their equilibrium position and the system was again relaxed. The results are summarized in the table below (Table 12). The I-I equilibrium distance was fully recovered after both tests were performed. The I_2-CNT distance was not exactly replicated after relaxation of the distorted systems, however both cases differ in final distance by less than 1% of the equilibrium value.

Table 12. Testing of precision of LAMMPS simulation of diatomic iodine adsorption on CNT.

	I_2 at an arbitrary location near surface		**10% increase from equilibrium position**		**10% decrease from equilibrium position**	
	Initial Distance (Å)	Final Distance (Å)	Initial Distance (Å)	Final Distance (Å)	Initial Distance (Å)	Final Distance (Å)
I-I	2.57	2.58	2.83	2.58	2.32	2.58
I_2-CNT	3.30	3.23	3.63	3.26	2.97	3.21

4.2.3 LAMMPS Implementation

The Large-scale Atomic/Molecular Massively Parallel Simulator (LAMMPS) [103,104] molecular dynamics code was used to simulate the diatomic iodine doping of a carbon nanotube. This was implemented in LAMMPS through a script using command and keywords. For reference, this input script is shown in Appendix E.

The script initializes by defining the type of units, type of atomic description, dimensions, and boundary conditions. In our case, the boundary conditions of the simulation box were set as finite in the two directions perpendicular to the tube axis and periodic in the direction parallel to the tube axis, as shown in Figure 51. Then, the atomic coordinates are defined for a (8,0) CNT with four unit cells using a data file (see Appendix F). The simulation box lengths, total number of atoms, atoms types and the atomic coordinates are all defined in the data.txt file, which is shown in Appendix F. For the atom style being used (charge), in the data file it is necessary to define the following attributes: atom ID, atom type, electronic charge, and atomic coordinates [105]. The atom style charge is being used because it is required for charge equilibration.

The molar mass is set for each element as 12.0107 g/mol and 126.905 g/mol for carbon and iodine, respectively. The interactions potentials were set using the parameters found from DFT calculations, as explained in the previous section *4.2.2. Interaction Potentials*, and shown in Table 9 and Table 10.

Using the reax/c force field requires charge equilibration to be performed during the minimization run using the fix qeq/reax command. In our run we found that charge equilibration could be done 50 steps with a tolerance of $1.0x10^{-8}$. More information on the other parameters of the fix qeq/reax command can be found online [106]. The neighbor command is used to build pairwise neighbor lists for all atoms within a cutoff distance equal to their force cutoff plus additional distance called the *skin* distance [107].

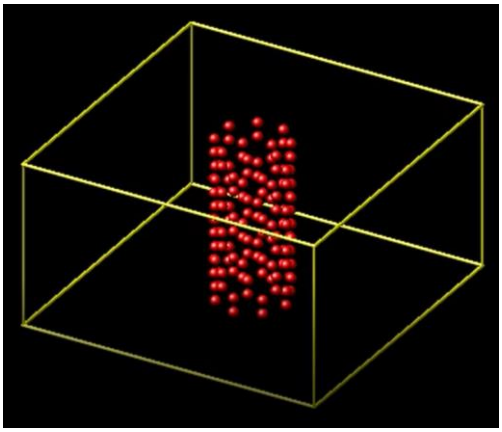

Figure 51. Carbon nanotube inside simulation box used for molecular dynamics simulations.

The script also uses some commands to generate some post-processing data, such as position coordinates of all atoms or only of the iodine dopant at a certain number of simulation steps, image of the simulation box every number of steps, and a movie in AVI format of the simulation box to visualize the change in position of all the atoms during the energy minimization run.

Finally, the minimize command performs an energy minimization of the entire system by adjusting the atomic positions iteratively until a stopping criterion is met [108]. In our doping simulations, a force tolerance of 0.1 eV/Å was used as the energy minimization run stopping criterion. The minimization style used is the Polak-Ribiere (PK) version of the conjugate gradient (CG) algorithm. The PR variant is thought to be the most effective CG choice for most problems [109].

4.2.4 Iodine Doping Algorithm

The previous section explains the implementation in a molecular dynamics code to minimize the structure of a (8,0) CNT doped with a diatomic iodine molecule. In order to

find the ideal doping site, an algorithm was developed and implemented using Matlab. The algorithm, shown Figure 52, performs as following: a random number generator is used to get the x, y, and z coordinates of an iodine atom within the simulation box (Figure 51) and near the surface of a (8,0) carbon nanotubes, and a second iodine atom is created within the iodine interatomic distance; then the program writes the data file needed for the LAMMPS run; the program calls LAMMPS to execute the minimization run for the (8,0) CNT and the diatomic iodine molecule; calculates the adsorption energy of the iodine molecule for the final location after energy minimization; finally, the program stores the initial and final coordinates of the iodine molecule and its adsorption energy at the final site. This cycle is repeated N times.

In order to improve the performance of this doping site algorithm, the range of possible values for the location of the iodine molecule were limited to a minimum distance of 1.0 Å and a maximum distance of 5.0 Å between the surface of the carbon nanotube and either one of the iodine atoms in the diatomic system.

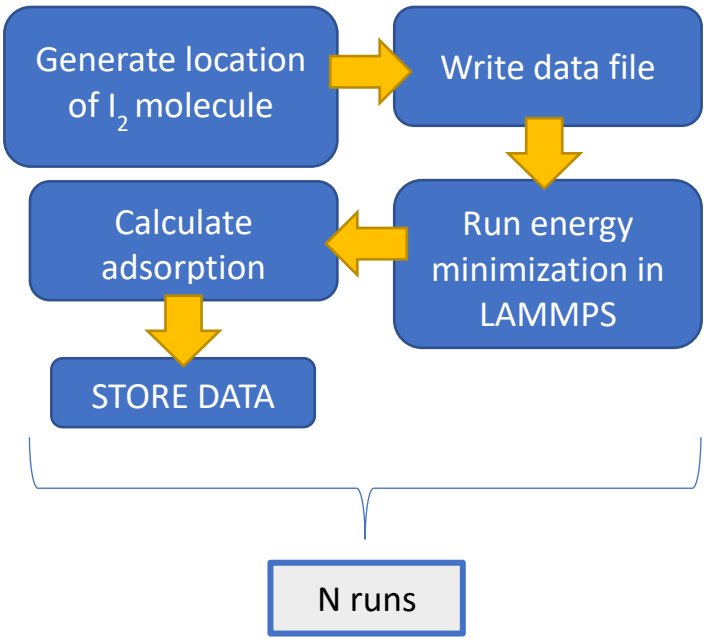

Figure 52. Diagram of the iodine doping algorithm implemented in Matlab.

It is common to analyze the behavior of a mean value in order to estimate the number of runs needed for convergence. In our case, the values that can be analyzed are the x and y coordinates being generated stochastically. After generating a certain number of x and y

coordinates, the mean value should converge to a value within some percent error criterion. However, in our case the x and y coordinates have a bimodal distribution which tends to vary greatly even after averaging over many values. Instead, the modes were analyzed to determine the number of runs needed to obtain a representative distribution of the x and y coordinates.

In order to analyze the number of runs, a certain number of random numbers were generated as the x and y coordinates of the iodine atoms within the 1.0-5.0 Å region around the (8,0) CNT surface. After which, the two modes are found for bins of 10 iterations. An example of a histogram showing the mode for bins of 10 iterations is shown below in Figure 53 for 5000 random numbers generated. The bimodal distribution for both x (Figure 53a) and y (Figure 53b) coordinates can be observed. These modes are then used to calculate the average mode for each successive bin for a certain number of runs.

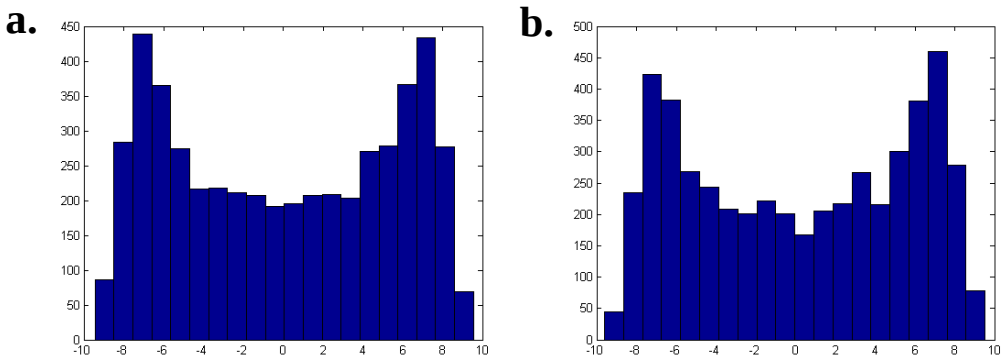

Figure 53. Histograms of values generated randomly of a) the x-coordinate of the iodine position and b) the y-coordinate of the same atom. Plots shows a bimodal distribution.

Using a convergence criterion of 5% for the average mode, the number of runs needed for convergence by normalizing both modes of the bimodal distributions for x and y coordinates and noting the exact number of runs for which the normalized average mode has an error of less than 5% with respect to the final average mode. An example of this is shown in Figure 54a for 5000 x coordinates generated stochastically. The normalized average modes are plotted as a function of the number of runs. Zooming into the graph (Figure 54b) shows that it takes more than 500 runs to converge to a value within the 5% criterion for mode2.

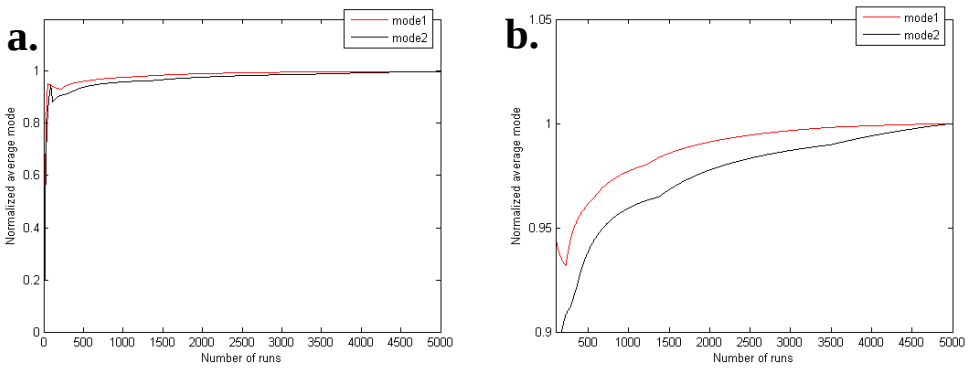

Figure 54. Analysis of the number of runs needed for convergence of the modes. a) Normalized average mode as a function of the number of runs. b) Zoomed into graph of the normalized average mode as a function of the number of runs that shows values converge to an error less than 5% after more than 500 runs.

In order to test the dependency of this convergence methodology on the number of runs, we decided to generate different amounts of random x coordinates of iodine atoms. The result of this test is shown in the table below:

Table 13. Number of runs needed for convergence for different amount of random iodine locations.

Total number of random iodine locations	Runs needed for convergence (5% criterion)
50,000	~2,900
100,000	~2,650
200,000	~3,300
500,000	~2,450

From this it was determined that with 3,500 randomly-generated iodine locations we could obtain a bimodal distribution with both modes within 5% error of a bimodal distribution with 500,000 randomly-generated iodine locations. This means that the data obtained from 3,300 runs is representative of the data obtained with 500,000 runs.

4.3 Results and Discussion

The previous study conducted by Ghosh *et al*. [29] was used as a starting point for the work in this chapter. In their work, a (5,5) armchair and (8,0) zigzag CNTs were doped with a diatomic iodine molecule with one diatomic molecule per unit cell. Using DFT calculations, they relaxed the structure and found the adsorption energy and the electronic band gap for the two aforementioned cases. Their results are shown in Table 14, from which we can see that the adsorption energy for both carbon nanotubes is enough to be considered chemisorption. However, the adsorption energy they found in their studies does not correspond to that of a single diatomic iodine molecule because of the size of their unit cell. Using periodic boundary conditions along the tube axis, in their work [29], Ghosh *et al.* have the case of a diatomic iodine molecule that is also interacting with its periodic image along the tube axis, for an adsorption doping atomic concentration of about 3%. This interaction seems to enhance the adsorption energy of the iodine molecule itself by forming a chain of diatomic iodine molecules.

Table 14. Results of the DFT calculations by Ghosh et al.[29].

CNT	Adsorption energy (eV)	Band gap (eV)
(5,5)	1.09	0
(8,0)	1.54	0.28

In order to obtain the adsorption energy of a single diatomic iodine molecule, it is needed to use a larger unit cell. For such purpose we performed DFT simulations, using the SIESTA package, of the adsorption energy of a diatomic iodine molecule at the same adsorption site used by Ghosh *et al.*, as shown in Figure 55, which corresponds to a much lower doping atomic concentration of about 1.5%. Our simulations showed an adsorption energy of 0.29 eV at a I_2-CNT distance of 3.29 Å, which is a significant difference with respect to Ghosh et al. We can conclude that the adsorption energy of a single diatomic iodine molecule on the (8,0) CNT is in the range of physisorption, and not in the range of chemisorption, as it could be incorrectly concluded from previous work [29].

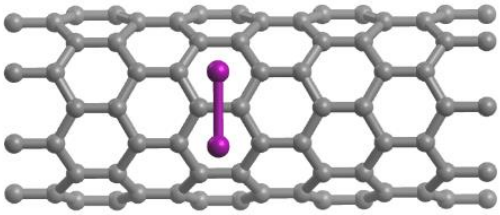

Figure 55. Unit cell including iodine dimer at the adsorption site studied by Ghosh et al.

Following the procedure outlined in section *4.2.4 Iodine Doping Algorithm*, and implemented in a Matlab programming environment, doping sites with a higher adsorption energy of that of the Ghosh *et al.* were found. After running 3,500 simulations with initial coordinates generated randomly within a region above the CNT surface, and minimizing the energy for each simulation, the top five sites with the largest adsorption energy were found. An example of 100 diatomic iodine molecules adsorbed separately on the surface of the (8,0) CNT is shown in Figure 56. This figure shows that the adsorption energy of the diatomic iodine molecules on the CNT surface is dependent on the distance and orientation with respect to the CNT.

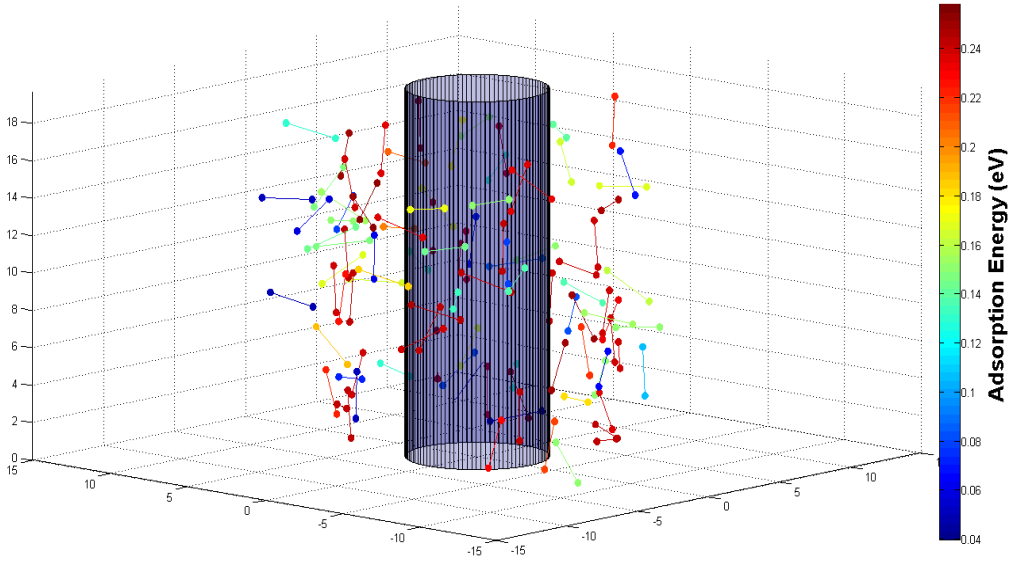

Figure 56. Example of 100 diatomic iodine molecules adsorbed independently on a (8,0) CNT (shown as a cylinder here).

The top five adsorption sites in term of the adsorption energy can be seen in Figure 57, which shows that all of the top adsorption sites are for diatomic iodine molecules oriented

diagonally with respect to the carbon nanotube axis, and with iodine atoms above the center of a hexagonal ring (although not perfectly centralized within the hexagonal ring). The top site can be seen in Figure 58. The adsorption energy found from using the stochastic approach is 0.33 eV, which is about 14% higher than at the doping location used by Ghosh *et al.*, and at a I_2-CNT distance of 3.39 Å. The doping concentration remains the same, about 1.5%.

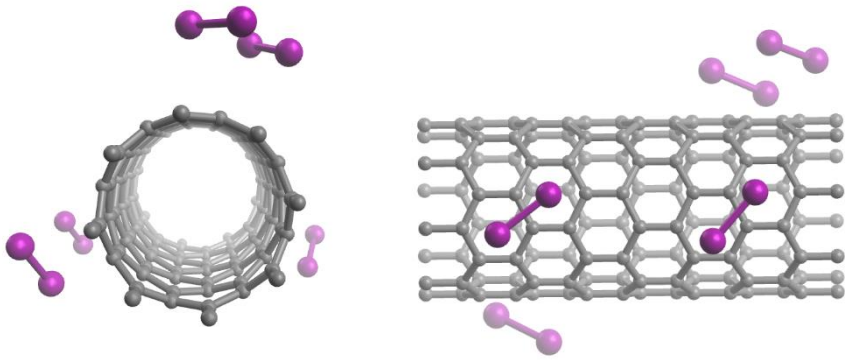

Figure 57. Top five doping sites found using a stochastic approach. a) Frontview and b) Sideview.

The effect of the iodine adsorption doping on the electronic band gap is shown below (Figure 59), for an adsorption concentration of about 1.5%. The electronic band gap does not change significantly after the adsorption of an iodine dimer at the site shown in Figure 58, varying down to 0.59 eV from an original value of 0.60 eV.

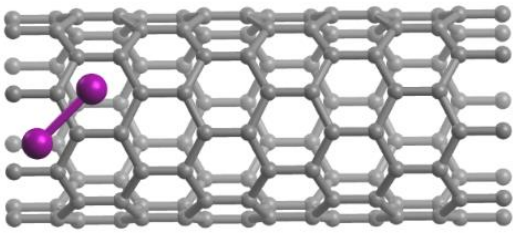

Figure 58. Unit cell with ideal adsorption site found using MD stochastic approach.

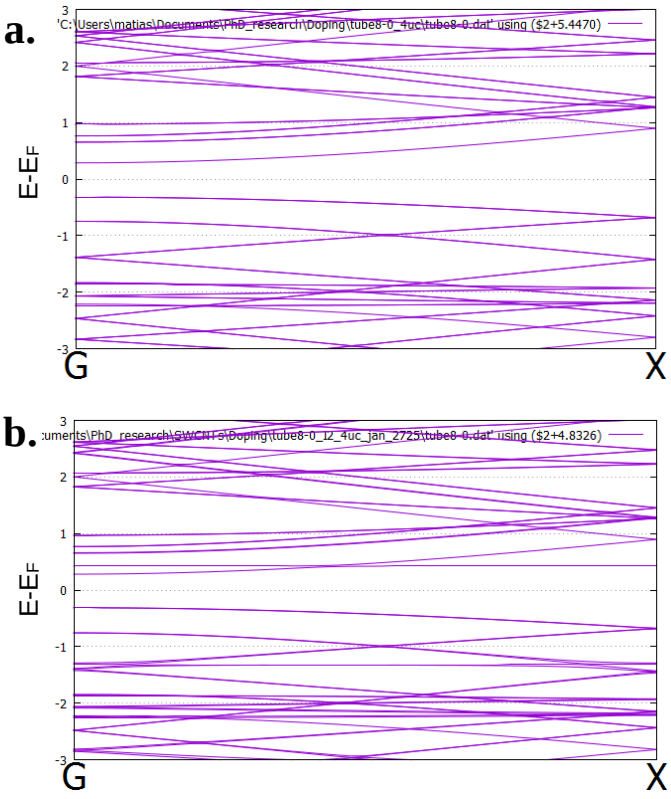

Figure 59. Band structure of the a) pristine (8,0) CNT and b) iodine-doped (8,0) CNT at ideal doping site. Label G represents the Γ point.

The doping concentration was increased for the case of diagonal orientation of the diatomic iodine molecule by reducing the nanotube supercell from four to two unit cells. The adsorption energy and electronic band gap was calculated for both the perpendicular and diagonal orientations for iodine atomic concentrations of 1.5 and 3.0 % (Table 15). The diagonal orientation has a higher adsorption energy at the lower doping concentration (1.5%); the comparison reverses at the higher doping concentration (3.0%) for which the adsorption energy of the perpendicular orientation is in the chemisorption region. In terms of the electronic band gap, the lower doping concentration (1.5%) has a negligible effect on it. A higher doping concentration (3.0%) reduces the electronic band gap by about 5 and 50% with the iodine diatomic molecule oriented diagonal and perpendicular to the tube axis, respectively.

The difference in adsorption energy of the concentration at 1.5 and 3.0 % has to do with the fact that at the higher doping concentration the supercell only has two unit cells with a lattice length along the tube axis of 8.5 Å; based on calculations of diatomic iodine in a

simulation box with a lattice constant of 8.5 Å in one direction and about 50 Å in the other two orthogonal directions and periodic boundary conditions, the DFT calculation acknowledges this system as a chain, which signifies interaction between the diatomic iodine molecules. This interaction or chaining of the diatomic iodine molecules when located near the surface of an infinitely-long carbon nanotube helps increase the adsorption energy of the dopant; the increase in adsorption energy due to chaining of the dopants is more significant for the iodine molecules oriented perpendicular to the tube axis.

Table 15. Adsorption energy and band gap of diatomic iodine adsorbed on a (8,0) CNT at different concentrations.

I_2 orientation	Adsorption energy (eV) 3.0% conc.	Band gap (eV)	Adsorption energy (eV) 1.5% conc.	Band gap (eV)
Perpendicular	**1.54 [53]**	**0.28 [53]**	**0.29**	**0.60**
Diagonal	**0.44**	**0.57**	**0.33**	**0.59**

The reduction in band gap for the diatomic iodine molecule oriented perpendicular to the tube axis at a concentration of 3.0% coincides with the reduction in resistivity of about 67% found experimentally when doping a carbon nanotube sample with gaseous iodine with a 3.3% atomic concentration, as previously reported [28].

4.4 Conclusions

Density functional theory calculations were used to determine the interaction energies of I-I and I_2-CNT at different separation distances. We were able to use these energies to formulate an interaction energy model based on the Morse potential for the I-I interaction and on the Lennard-Jones potential for the I-C interaction. The pairwise I-C interaction was modeled by assuming a cutoff of 10 Å and a pairwise sum equal to the coarse-grain I_2-CNT interaction for any separation distance between the iodine dimer and the CNT. Using the formulated interaction potentials in MD simulations, we were able to reproduce the behavior of a diatomic iodine and its interaction with the surface of a carbon nanotube from DFT-LDA simulations.

Adsorption of an iodine diatomic molecular on the surface of a (8,0) carbon nanotube can be studied using a stochastic approach for the generation of iodine dimers near the surface of the CNT, and energy minimization using molecular dynamics. Such approach was successful in identifying the ideal adsorption site of the iodine dimer on the CNT surface. Diatomic iodine doping preferred site (for single molecule) is diagonally oriented with respect to CNT axis and with iodine atoms in the center of hexagonal rings.

First-principles DFT simulations calculated the adsorption energy of the ideal site found using the stochastic approach to be ~14% higher than the adsorption energy at the site previously studied by Ghosh et at. The adsorption doping concentration of one iodine dimer per four unit cells of a (8,0) CNT does not cause a significant change in the electronic band gap of the CNT. This corresponds to a doping concentration of 1.5%. A higher doping concentration of about 3% is needed to bring about a significant decrease in the electronic band gap of a semiconductor SWCNT. Interaction with nearby diatomic iodine molecules (which also increases the doping concentration) increases the binding energy; also the electronic band gap decreases with respect to iodine dopants that are isolated from interaction with their periodic images along the tube axis. The interaction between diatomic iodine molecules is also dependent on their orientation with respect to each other. This signifies that iodine doping coupled with I_2-I_2 interaction can affect the electronic properties of a carbon nanotube more than iodine doping alone.

4.5 Future Work

The study of the effect of doping on the electronic properties of carbon nanotubes was limited to iodine doping in gaseous phase and diatomic molecular arrangement. As discussed in *4.1 Introduction* section, iodine can also exist in longer chains that may be more reactive when interacting with CNTs. The study of iodine doping in chain-like configuration could also provide interesting insight into the effect on the properties of carbon nanotubes. Following the methodology outlined in this chapter, it would be possible to simulate the interaction of an iodine chain with a carbon nanotube.

It is also interesting to know how the iodine dopant behaves when near the surface of a nanotube bundle. As was found in this work, the adsorption energy of a diatomic iodine molecule on an individual CNT increases when interacting with another iodine molecule in the vicinity; perhaps this type of behavior would also be observed when interacting with a CNT bundle, whether on its surface or in the interstitial sites (or grooves) of a bundle. Additionally, the methodology outlined in this chapter could be also be used in the study of the adsorption doping of other elements on carbon nanotubes.

This work was limited to the study of the interaction of iodine molecules on individual carbon nanotubes. In order to understand the effect of iodine doping (or other dopants for that matter) on a CNT bundle or even wire, it would be needed to simulate a carbon nanotube surface at a larger scale and with multiple iodine molecules interacting with one another and with the carbon atoms on the CNT bundle. Such a study could be done using molecular dynamics or Monte Carlo approach, using appropriate interatomic potentials (such as the ones developed in this work), and at iodine concentrations relevant to previous experimental studies.

It is also known that dopants can act as nanotube junctions [85], additional to their effect on the electronic properties of individual carbon nanotubes. A stochastic approach to the study of dopants as junctions, such as iodine or others, in order to find its interaction with the tube surface of two nearby CNTs, could be used. Such a study could use some of the methodology outlined in this chapter in order to find ideal junction sites on the tube side wall or even the end cap.

References

[1] S. Iijima, *Nature* **1991**, *354*, 56.

[2] S. Tans, A. Verschueren, C. Dekker, *Nature* **1998**, *672*, 669.

[3] R. Pfeiffer, T. Pichler, Y. A. Kim, H. Kuzmany, in *Carbon Nanotub.* (Eds.: A. Jorio, G. Dresselhaus, M.S. Dresselhaus), Springer-Verlag, Berlin Heidelberg, **2008**, pp. 495–530.

[4] S. Zhang, W. K. Liu, R. S. Ruoff, *Nano Lett.* **2004**, *4*, 293.

[5] D. Tománek, A. Jorio, M. S. Dresselhaus, G. Dresselhaus, in *Carbon Nanotub. Adv. Top. Synth. Struct. Prop. Appl.* (Eds.: A. Jorio, G. Dresselhaus, M.S. Dresselhaus), Springer-Verlag, Berlin Heidelberg, **2008**, pp. 1–12.

[6] L. M. Ericson, H. Fan, V. A. Davis, *Science (80-.).* **2004**, *305*, 1447.

[7] "NT Basics," can be found under http://ipn2.epfl.ch/CHBU/NTbasics1.htm, **n.d.**

[8] R. Saito, M. Fujita, G. Dresselhaus, M. S. Dresselhaus, *Phys. Rev. B* **1992**, *46*, 1804.

[9] M. S. Dresselhaus, G. Dresselhaus, R. Saito, *Carbon N. Y.* **1995**, *33*, 883.

[10] J. W. Mintmire, C. T. White, *Carbon N. Y.* **1995**, *33*, 893.

[11] T. W. Odom, J. Huang, P. Kim, C. M. Lieber, *Nature* **1998**, *391*, 62.

[12] N. Hamada, S. I. Sawada, A. Oshiyama, *Phys. Rev. Lett.* **1992**, *68*, 1579.

[13] X. Blase, L. X. Benedict, E. L. Shirley, S. G. Louie, *Phys. Rev. Lett.* **1994**, *72*, 1878.

[14] V. Zólyomi, J. Kürti, *Phys. Rev. B* **2004**, *70*, 85403.

[15] W. Song, M. Ni, J. Lu, Z. Gao, S. Nagase, D. Yu, H. Ye, X. Zhang, *Chem. Phys. Lett.* **2005**, *414*, 429.

[16] N. Behabtu, C. C. Young, D. E. Tsentalovich, O. Kleinerman, X. Wang, A. W. K. Ma, E. A. Bengio, R. F. ter Waarbeek, J. J. de Jong, R. E. Hoogerwerf, S. B. Fairchild, J. B. Ferguson, B. Maruyama, J. Kono, Y. Talmon, Y. Cohen, M. J. Otto, M. Pasquali, *Science (80-.).* **2013**, *339*, 182.

[17] F. Xu, A. Sadrzadeh, Z. Xu, B. I. Yakobson, *J. Appl. Phys.* **2013**, *114*, 63714.

[18] J. R. Sanchez-Valencia, T. Dienel, O. Gröning, I. Shorubalko, A. Mueller, M. Jansen, K. Amsharov, P. Ruffieux, R. Fasel, *Nature* **2014**, *512*, 61.

[19] V. Zólyomi, J. Koltai, Á. Rusznyák, J. Kürti, Á. Gali, F. Simon, H. Kuzmany, Á. Szabados, P. R. Surján, *Phys. Rev. B - Condens. Matter Mater. Phys.* **2008**, *77*, 1.

[20] S. Okada, A. Oshiyama, *Phys. Rev. Lett.* **2003**, *91*, 216801.

[21] R. Saito, G. Dresselhaus, M. S. Dresselhaus, *J. Appl. Phys.* **1993**, *73*, 494.

[22] Y. Fan, B. R. Goldsmith, P. G. Collins, *Nat. Mater.* **2005**, *4*, 906.

[23] W. Orellana, P. Fuentealba, *Surf. Sci.* **2006**, *600*, 4305.

[24] J. C. Charlier, *Acc. Chem. Res.* **2002**, *35*, 1063.

[25] L. Grigorian, K. A. Williams, S. Fang, G. U. Sumanasekera, A. L. Loper, E. C. Dickey, S. J. Pennycook, P. C. Eklund, *Phys. Rev. Lett.* **1998**, *80*, 5560.

[26] C. Hayakawa, K. Urita, T. Ohba, H. Kanoh, K. Kaneko, *Langmuir* **2009**, 1795.

[27] A. A. Tonkikh, V. I. Tsebro, E. A. Obraztsova, K. Suenaga, H. Kataura, A. G. Nasibulin, E. I. Kauppinen, E. D. Obraztsova, *Carbon N. Y.* **2015**, *94*, 768.

[28] Y. Zhao, J. Wei, R. Vajtai, P. M. Ajayan, E. V Barrera, *Sci. Rep.* **2011**, *1*, 83.

[29] S. Ghosh, S. R. K. C. S. Yamijala, S. K. Pati, C. N. R. Rao, *RSC Adv.* **2012**, *2*, 1181.

[30] W. I. Choi, J. Ihm, G. Kim, *Appl. Phys. Lett.* **2008**, *92*, 19.

[31] J. M. Wernik, S. a. Meguid, *Appl. Mech. Rev.* **2010**, *63*, 50801.

[32] P. M. Ajayan, S. Lijima, *Nature* **1992**, *358*, 23.

[33] C. Kiang, *J. Phys. Chem. A* **2000**, *104*, 2454.

[34] K. Kato, T. Koretsune, S. Saito, *J. Phys. Conf. Ser.* **2011**, *302*, 12007.

[35] J. M. Soler, E. Artacho, J. D. Gale, A. Garcìa, J. Junquera, P. Ordejòn, D. Sànchez-Portal, *J. Phys. Condens. Matter* **2002**, *14*, 2745.

[36] P. Hohengerg, W. Kohn, *Phys. Rev.* **1964**, *136*, 864.

[37] W. Kohn, L. J. Sham, *Phys. Rev.* **1965**, *140*, 1133.

[38] E. Artacho, J. M. Cela, J. D. Gale, A. Garcia, J. Junquera, R. M. Martin, P. Ordejon, D. Sanchez-Portal, J. M. Soler, *SIESTA 3.2 User's Guide*, Fundacion General Universidad Autonoma De Madrid, **2013**.

[39] S. Reich, C. Thomsen, P. Ordejon, *Phys. Rev. B - Condens. Matter Mater. Phys.* **2002**, *65*, 155411.

[40] J. Klimes, D. R. Bowler, A. Michaelides, *Phys. Rev. B - Condens. Matter Mater. Phys.* **2011**, *83*, 1.

[41] S. Grimme, *J. Comput. Chem.* **2006**, *27*, 1787.

[42] SIESTA, "LDA Pseudopotential Database," can be found under https://departments.icmab.es/leem/siesta//Databases/Pseudopotentials/periodictable-lda-abinit.html, **n.d.**

[43] SIESTA, "Basis Set Database," can be found under https://departments.icmab.es/leem/siesta//Databases/BasisSets/periodictable-bases.html, **n.d.**

[44] E. Artacho, E. Anglada, O. Diéguez, J. D. Gale, A. García, J. Junquera, R. M. Martin, P. Ordejón, J. M. Pruneda, D. Sánchez-Portal, J. M. Soler, *J. physics. Condens. matter.* **2008**, *20*, 64208.

[45] JCrystalSoft, **2016**.

[46] gnuplot, **2015**.

[47] K. Kanamitsu, S. Saito, *J. Phys. Soc. Japan* **2002**, *71*, 483.

[48] I. Cabria, J. Mintmire, C. White, *Phys. Rev. B* **2003**, *67*, 4.

[49] O. Dubay, G. Kresse, *Phys. Rev. B* **2003**, *67*, 35401.

[50] M. Ouyang, J. L. Huang, C. L. Cheung, C. M. Lieber, *Science (80-.).* **2001**, *292*, 702.

[51] R. W. Godby, M. Schlüter, L. J. Sham, *Phys. Rev. B* **1988**, *37*, 10159.

[52] R. W. Godby, M. Schlüter, L. J. Sham, *Phys. Rev. Lett.* **1986**, *56*, 2415.

[53] W. Mintmire, C. T. White, *Phys. Rev. B* **1987**, *35*, 4180.

[54] O. Gülseren, T. Yildirim, S. Ciraci, *Phys. Rev. B* **2002**, *65*, 153405.

[55] G. Sun, *J. Phys. Chem. B* **2003**, *107*, 6924.

[56] R. Demichelis, Y. Noël, P. D'Arco, M. Rérat, C. M. Zicovich-Wilson, R. Dovesi, *J. Phys. Chem. C* **2011**, *115*, 8876.

[57] R. Wan, J. H. Peng, X. Zhang, C. Leng, *Phys. B Condens. Matter* **2013**, *417*, 1.

[58] Y. Matsuda, J. Tahir-Kheli, W. a. Goddard, *J. Phys. Chem. Lett.* **2010**, *1*, 2946.

[59] S.-D. Liang, *Phys. B Condens. Matter* **2004**, *352*, 305.

[60] J. C. Charlier, J. P. Michenaud, *Phys. Rev. Lett.* **1993**, *70*, 1858.

[61] M. Endo, H. Muramatsu, T. Hayashi, Y. A. Kim, M. Terrones, M. S. Dresselhaus, *Nature* **2005**, *433*, 476.

[62] M. Soto, T. A. Boyer, S. Biradar, L. Ge, R. Vajtai, A. Elías-Zúñiga, P. M. Ajayan,

E. V Barrera, *Nanotechnology* **2015**, *26*, 165201.

[63] Y. Hu, I. Jang, S. B. Sinnott, *Compos. Sci. Technol.* **2003**, *63*, 1663.

[64] C. A. Cooper, S. R. Cohen, A. H. Barber, H. D. Wagner, *Appl. Phys. Lett.* **2002**, *81*, 3873.

[65] B. Ni, S. Sinnott, *Phys. Rev. B* **2000**, *61*, R16343.

[66] B. Ni, R. Andrews, D. Jacques, D. Qian, M. B. J. Wijesundara, Y. Choi, L. Hanley, S. B. Sinnott, *J. Phys. Chem. B* **2001**, *105*, 12719.

[67] M. Huhtala, A. V. Krasheninnikov, J. Aittoniemi, S. J. Stuart, K. Nordlund, K. Kaski, *Phys. Rev. B - Condens. Matter Mater. Phys.* **2004**, *70*, 1.

[68] M. Terrones, F. Banhart, N. Grobert, J.-C. Charlier, H. Terrones, P. M. Ajayan, *Phys. Rev. Lett.* **2002**, *89*, 75505.

[69] N. Pierard, A. Fonseca, Z. Konya, I. Willems, G. Van Tendeloo, J. B. Nagy, *Chem. Phys. Lett.* **2001**, *335*, 1.

[70] R. Andrews, D. Jacques, D. Qian, E. C. Dickey, *Carbon N. Y.* **2001**, *39*, 1681.

[71] D. B. Mawhinney, V. Naumenko, A. Kuznetsova, J. T. Yates, J. Liu, R. E. Smalley, *Chem. Phys. Lett.* **2000**, *324*, 213.

[72] M. Sammalkorpi, A. Krasheninnikov, A. Kuronen, K. Nordlund, K. Kaski, *Phys. Rev. B - Condens. Matter Mater. Phys.* **2004**, *70*, 1.

[73] A. Kis, G. Csányi, J.-P. Salvetat, T.-N. Lee, E. Couteau, A. J. Kulik, W. Benoit, J. Brugger, L. Forró, *Nat. Mater.* **2004**, *3*, 153.

[74] P. Ajayan, V. Ravikumar, J.-C. Charlier, *Phys. Rev. Lett.* **1998**, *81*, 1437.

[75] L. Chico, L. Benedict, S. Louie, M. Cohen, *Phys. Rev. B* **1996**, *54*, 2600.

[76] M. Soto, M. Esteva, O. Martínez-Romero, J. Baez, A. Elías-Zúñiga, *Materials (Basel).* **2015**, *8*, DOI 10.3390/ma8105334.

[77] G. Dominguez-Rodriguez, A. Tapia, G. D. Seidel, F. Aviles, *Adv. Eng. Mater.* **2016**, *18*, 1897.

[78] S. H. Jhi, S. G. Louie, M. L. Cohen, *Solid State Commun.* **2002**, *123*, 495.

[79] T. Kim, G. Kim, W. I. Choi, Y. K. Kwon, J. M. Zuo, *Appl. Phys. Lett.* **2010**, *96*, 16.

[80] N. Park, Y. Miyamoto, K. Lee, W. Ih Choi, J. Ihm, J. Yu, S. Han, *Chem. Phys. Lett.* **2005**, *403*, 135.

[81] J. Zhao, A. Buldum, J. Han, J. P. Lu, *Nanotechnology* **2002**, *13*, 195.

[82] E. Durgun, S. Dag, V. Bagci, O. Gülseren, T. Yildirim, S. Ciraci, *Phys. Rev. B* **2003**, *67*, 1.

[83] X. Guo, J. P. Small, J. E. Klare, Y. Wang, M. S. Purewal, I. W. Tam, B. H. Hong, R. Caldwell, L. Huang, S. O. Brien, J. Yan, R. Breslow, S. J. Wind, J. Hone, P. Kim, C. Nuckolls, *Science (80-.).* **2006**, *311*, 356.

[84] D. Wei, Y. Liu, L. Cao, Y. Wang, H. Zhang, G. Yu, *Nano Lett.* **2008**, *8*, 1625.

[85] E. Y. Li, N. Marzari, *ACS Nano* **2011**, *5*, 9726.

[86] F. Khoerunnisa, T. Fujimori, T. Itoh, H. Kanoh, T. Ohba, M. Yudasaka, S. Iijima, K. Kaneko, *Chem. Phys. Lett.* **2011**, *501*, 485.

[87] X. Fan, E. Dickey, P. Eklund, K. Williams, L. Grigorian, R. Buczko, S. Pantelides, S. Pennycook, *Phys. Rev. Lett.* **2000**, *84*, 4621.

[88] J. Cambedouzou, J.-L. Sauvajol, A. Rahmani, E. Flahaut, A. Peigney, C. Laurent, *Phys. Rev. B* **2004**, *69*, 235422.

[89] W. Zhou, S. Xie, L. Sun, D. Tang, Y. Li, Z. Liu, L. Ci, X. Zou, G. Wang, P. Tan, X. Dong, B. Xu, B. Zhao, *Appl. Phys. Lett.* **2002**, *80*, 2553.

[90] T. Michel, L. Alvarez, J. L. Sauvajol, R. Almairac, R. Aznar, O. Mathon, J. L. Bantignies, E. Flahaut, *J. Phys. Chem. Solids* **2006**, *67*, 1190.

[91] N. Bendiab, R. Almairac, S. Rols, R. Aznar, J.-L. Sauvajol, I. Mirebeau, *Phys. Rev. B* **2004**, *69*, 1.

[92] S. L. Hsu, a. J. Signorelli, G. P. Pez, R. H. Baughman, *J. Chem. Phys.* **1978**, *69*, 106.

[93] S. Gotovac, H. Honda, Y. Hattori, K. Takahashi, H. Kanoh, K. Kaneko, *Nano Lett.* **2007**, *7*, 583.

[94] S. Gotovac-Atlagic, T. Hosokai, T. Ohba, Y. Ochiai, H. Kanoh, N. Ueno, K. Kaneko, *Phys. Rev. B* **2010**, *82*, 1.

[95] S. Kazaoui, N. Minami, R. Jacquemin, H. Kataura, Y. Achiba, *Phys. Rev. B* **1999**, *60*, 13339.

[96] K. R. Kissell, K. B. Hartman, P. A. W. Van Der Heide, L. J. Wilson, *J. Phys. Chem. B* **2006**, *110*, 17425.

[97] Y. Jung, S. J. Hwang, S. J. Kim, *J. Phys. Chem. C* **2007**, *111*, 10181.

[98] D. Rybkovskiy, A. Osadchy, E. Obraztsova, *Phys. Status Solidi Basic Res.* **2012**, *249*, 2608.

[99] L. Guan, K. Suenaga, Z. Shi, Z. Gu, S. Iijima, *Nano Lett.* **2007**, *7*, 1532.

[100] M. Allen, *Comput. Soft Matter From Synth. Polym. to …* **2004**, *23*, 1.

[101] K. Chenoweth, A. C. T. van Duin, W. A. Goddard, *J. Phys. Chem. A* **2008**, *112*, 1040.

[102] S. Corporation, "pair_style reax/c command," can be found under http://lammps.sandia.gov/doc/pair_reax_c.html#chenoweth-20082, **2013**.

[103] S. Plimpton, *J. Comput. Phys.* **1995**, *117*, 1.

[104] S. Corporation, **2016**.

[105] S. Corporation, "atom_style command," can be found under http://lammps.sandia.gov/doc/atom_style.html, **2013**.

[106] S. Corporation, "fix qeq/reax command," can be found under http://lammps.sandia.gov/doc/fix_qeq_reax.html, **2013**.

[107] S. Corporation, "neighbor command," can be found under http://lammps.sandia.gov/doc/neighbor.html, **2013**.

[108] S. Corporation, "minimize command," can be found under http://lammps.sandia.gov/doc/minimize.html, **2013**.

[109] S. Corporation, "min_style command," can be found under http://lammps.sandia.gov/doc/min_style.html, **2013**.

Appendix A

Input file (knows as FDF file) used for the energy minimization in SIESTA of a (8,0) SWCNT:

```
# (8,0) nanotube
#
SystemName        (8,0)SWCNT
SystemLabel       tube8-0

NumberOfAtoms     32
NumberOfSpecies   1

%block ChemicalSpeciesLabel
    1    6  C
%endblock ChemicalSpeciesLabel

PAO.EnergyShift             0.0036749 Ry

%block kgrid_Monkhorst_Pack
  1   0   0    0.5
  0   1   0    0.5
  0   0  25    0.5
%endblock kgrid_Monkhorst_Pack

MD.TypeOfRun                CG
MD.NumCGsteps               200
MD.VariableCell             false
WriteCoorStep               true
MD.MaxForceTol              0.04 eV/Ang

MeshCutoff                  300. Ry
SolutionMethod              diagon
MaxSCFIterations            200
DM.MixingWeight             0.01
DM.Tolerance                1.d-4
DM.NumberPulay              4
ElectronicTemperature       300 K
DM.UseSaveDM                true
UseSaveData                 true
SaveRho                     true
WriteDenchar                true

SpinPolarized         false
xc.functional         LDA
xc.authors            CA

WriteMullikenPop       1
```

```
%block BandLines
  1   0.000000   0.000000  0.0000   \Gamma
 20   0.000000   0.000000  1.0000   X
%endblock BandLines

LatticeConstant 4.257 Ang
%block LatticeVectors
   7.000   0.000   0.000
   0.000   7.000   0.000
   0.000   0.000   1.000
%endblock LatticeVectors

AtomicCoordinatesFormat NotScaledCartesianAng
%block AtomicCoordinatesAndAtomicSpecies
3.1338     0.0000     0.0000     1
2.8952     1.1992     2.1315     1
3.1338     0.0000     1.4210     1
2.8952     1.1992     3.5525     1
2.2159     2.2159     0.0000     1
1.1992     2.8952     2.1315     1
2.2159     2.2159     1.4210     1
1.1992     2.8952     3.5525     1
0.0000     3.1338     0.0000     1
-1.1992    2.8952     2.1315     1
0.0000     3.1338     1.4210     1
-1.1992    2.8952     3.5525     1
-2.2159    2.2159     0.0000     1
-2.8952    1.1992     2.1315     1
-2.2159    2.2159     1.4210     1
-2.8952    1.1992     3.5525     1
-3.1338    0.0000     0.0000     1
-2.8952    -1.1992    2.1315     1
-3.1338    0.0000     1.4210     1
-2.8952    -1.1992    3.5525     1
-2.2159    -2.2159    0.0000     1
-1.1992    -2.8952    2.1315     1
-2.2159    -2.2159    1.4210     1
-1.1992    -2.8952    3.5525     1
0.0000     -3.1338    0.0000     1
1.1992     -2.8952    2.1315     1
0.0000     -3.1338    1.4210     1
1.1992     -2.8952    3.5525     1
2.2159     -2.2159    0.0000     1
2.8952     -1.1992    2.1315     1
2.2159     -2.2159    1.4210     1
2.8952     -1.1992    3.5525     1
%endblock AtomicCoordinatesAndAtomicSpecies
```

Appendix B

Band structure of all SWCNTs considered in this work for energies ±3 eV with respect to the Fermi level:

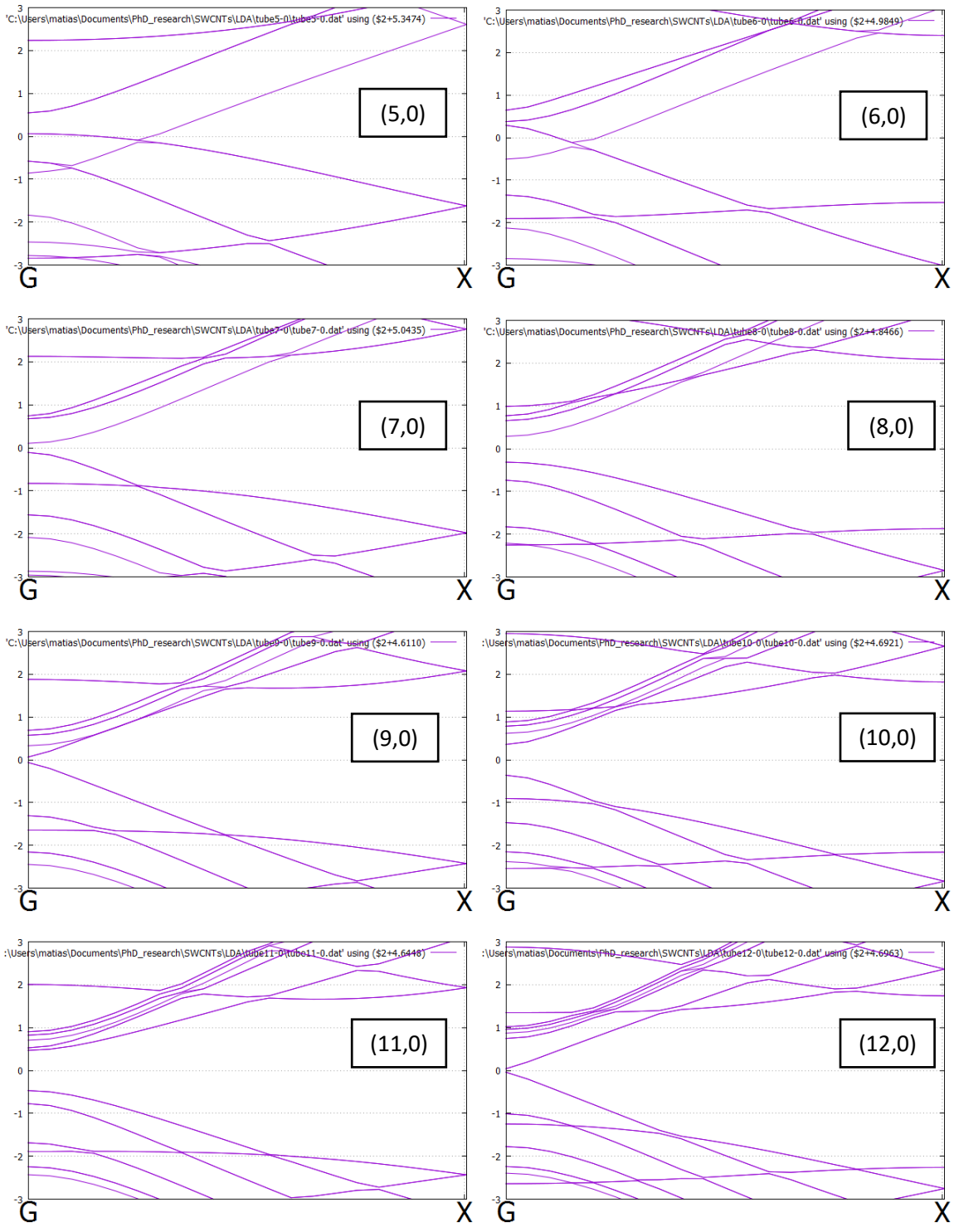

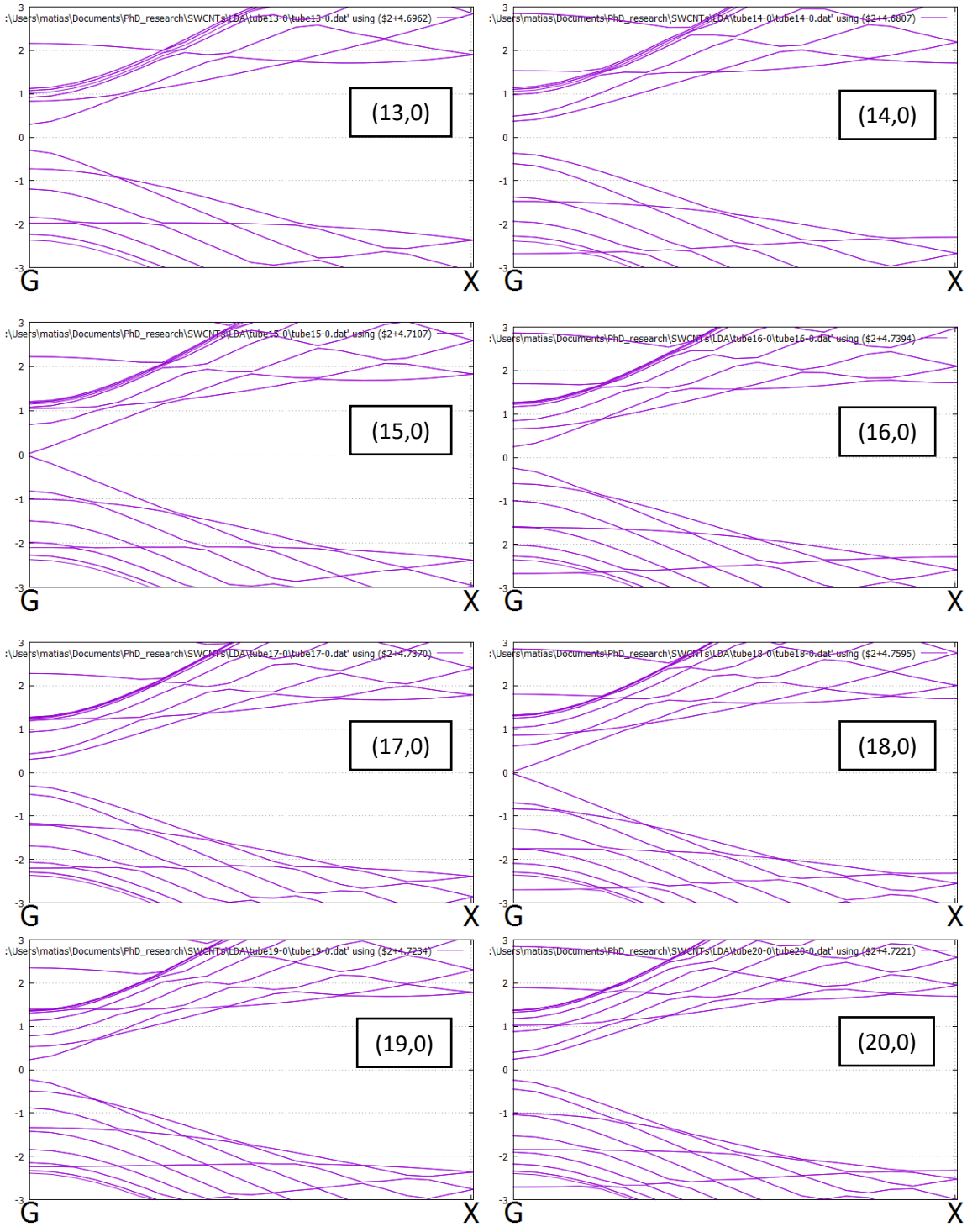
(13,0)
(14,0)
(15,0)
(16,0)
(17,0)
(18,0)
(19,0)
(20,0)
G
X

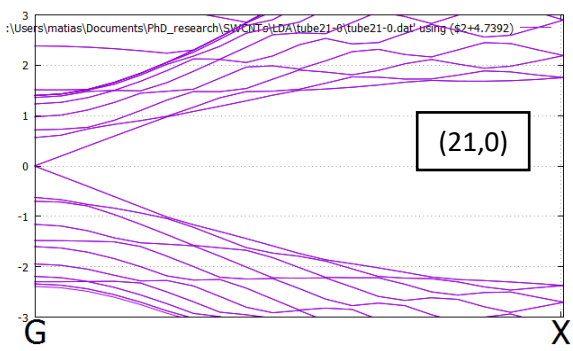
:\Users\matias\Documents\PhD_research\SWCNTs\LDA\tube21-0\tube21-0.dat' using ($2+4.7392)
(21,0)
G
X

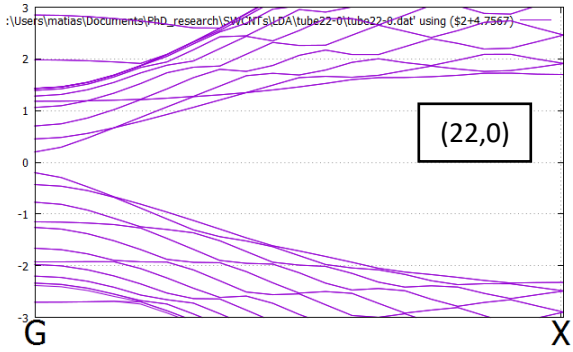
:\Users\matias\Documents\PhD_research\SWCNTs\LDA\tube22-0\tube22-0.dat' using ($2+4.7567)
(22,0)
G
X

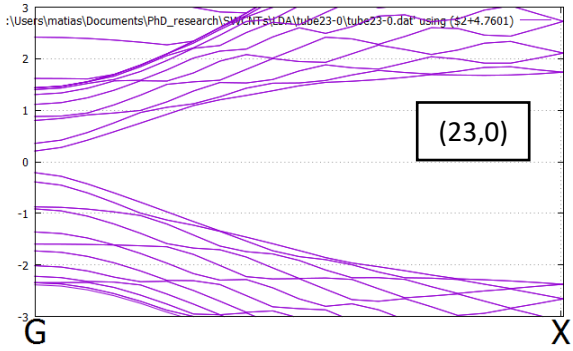
:\Users\matias\Documents\PhD_research\SWCNTs\LDA\tube23-0\tube23-0.dat' using ($2+4.7601)
(23,0)
G
X

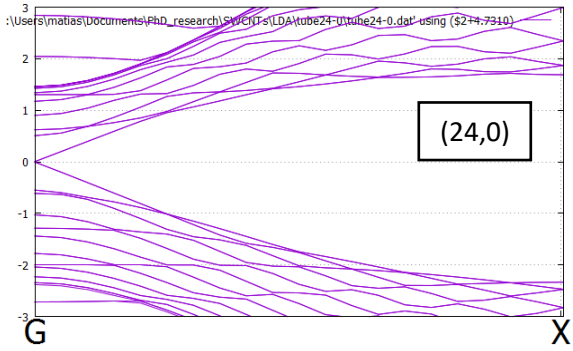
:\Users\matias\Documents\PhD_research\SWCNTs\LDA\tube24-0\tube24-0.dat' using ($2+4.7310)
(24,0)
G
X

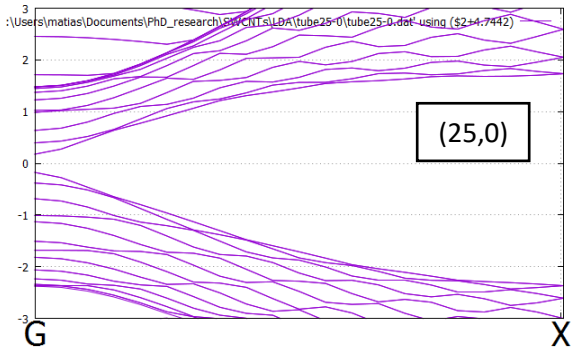
:\Users\matias\Documents\PhD_research\SWCNTs\LDA\tube25-0\tube25-0.dat' using ($2+4.7442)
(25,0)
G
X

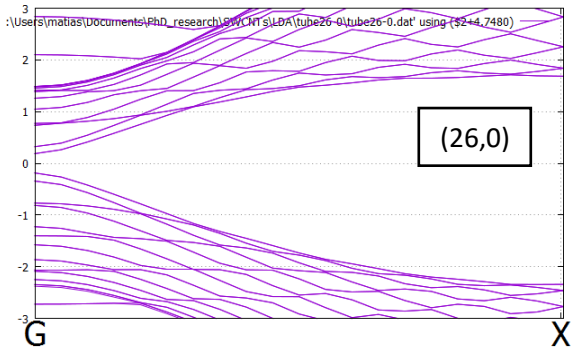
:\Users\matias\Documents\PhD_research\SWCNTs\LDA\tube26-0\tube26-0.dat' using ($2+4.7480)
(26,0)
G
X

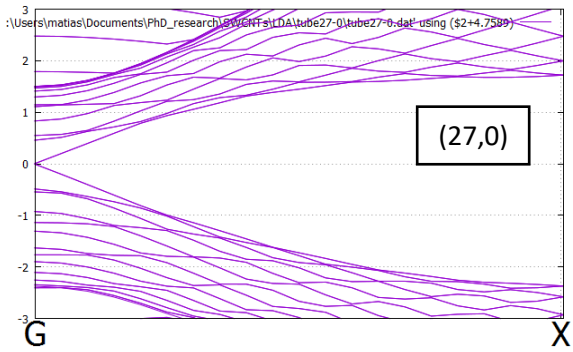
:\Users\matias\Documents\PhD_research\SWCNTs\LDA\tube27-0\tube27-0.dat' using ($2+4.7589)
(27,0)
G
X

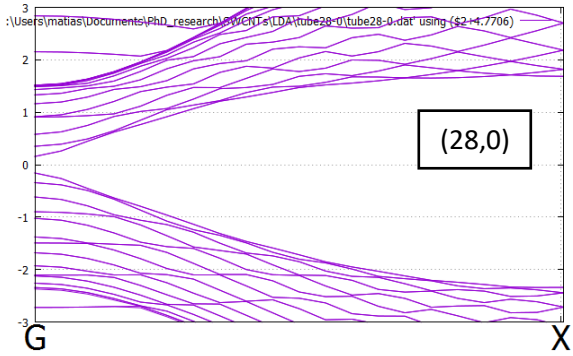
:\Users\matias\Documents\PhD_research\SWCNTs\LDA\tube28-0\tube28-0.dat' using ($2+4.7706)
(28,0)
G
X

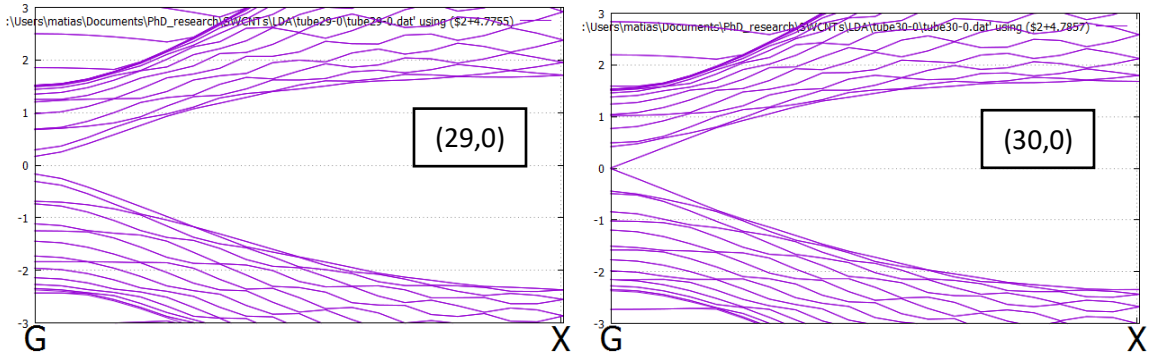
:\Users\matias\Documents\PhD_research\3WCNTs\LDA\tube29-0\tube29-0.dat' using ($2+4.7755)
(29,0)
G
X
:\Users\matias\Documents\PhD_research\3WCNTs\LDA\tube30-0\tube30-0.dat' using ($2+4.7857)
(30,0)
G
X

Appendix C

Input file (knows as FDF file) used for the energy minimization in SIESTA of a (8,0)@(16,0) DWCNT:

```
# (8,0),(16,0) double-walled nanotube
#
SystemName        (8,0),(16,0)DWCNT
SystemLabel       tube8-0-16-0

NumberOfAtoms     96
NumberOfSpecies   1

%block ChemicalSpeciesLabel
    1    6  C
%endblock ChemicalSpeciesLabel

PAO.EnergyShift             0.0036749 Ry

%block kgrid_Monkhorst_Pack
  1   0   0    0.5
  0   1   0    0.5
  0   0  40    0.5
%endblock kgrid_Monkhorst_Pack

Diag.Memory                 5.0

MD.TypeOfRun                CG
MD.NumCGsteps               200
MD.VariableCell             false
WriteCoorStep               true
MD.MaxForceTol              0.02 eV/Ang

MeshCutoff                  400. Ry
SolutionMethod              diagon
MaxSCFIterations            200
DM.MixingWeight             0.01
DM.Tolerance                1.d-4
DM.NumberPulay              4
ElectronicTemperature       200 K
DM.UseSaveDM                true
UseSaveData                 true
SaveRho                     true
WriteDenchar                true

SpinPolarized               false
xc.functional               LDA
xc.authors                  CA
```

```
WriteMullikenPop           1

%block BandLines
  1   0.000000   0.000000  0.0000   \Gamma
 45   0.000000   0.000000  1.0000   X
%endblock BandLines

LatticeConstant 4.257 Ang
%block LatticeVectors
   8.000   0.000   0.000
   0.000   8.000   0.000
   0.000   0.000   1.000
%endblock LatticeVectors

AtomicCoordinatesFormat NotScaledCartesianAng
%block AtomicCoordinatesAndAtomicSpecies
3.1338     0.0000     0.0000     1
2.8952     1.1992     2.1315     1
3.1338     0.0000     1.4210     1
2.8952     1.1992     3.5525     1
2.2159     2.2159     0.0000     1
1.1992     2.8952     2.1315     1
2.2159     2.2159     1.4210     1
1.1992     2.8952     3.5525     1
0.0000     3.1338     0.0000     1
-1.1992    2.8952     2.1315     1
0.0000     3.1338     1.4210     1
-1.1992    2.8952     3.5525     1
-2.2159    2.2159     0.0000     1
-2.8952    1.1992     2.1315     1
-2.2159    2.2159     1.4210     1
-2.8952    1.1992     3.5525     1
-3.1338    0.0000     0.0000     1
-2.8952    -1.1992    2.1315     1
-3.1338    0.0000     1.4210     1
-2.8952    -1.1992    3.5525     1
-2.2159    -2.2159    0.0000     1
-1.1992    -2.8952    2.1315     1
-2.2159    -2.2159    1.4210     1
-1.1992    -2.8952    3.5525     1
0.0000     -3.1338    0.0000     1
1.1992     -2.8952    2.1315     1
0.0000     -3.1338    1.4210     1
1.1992     -2.8952    3.5525     1
2.2159     -2.2159    0.0000     1
2.8952     -1.1992    2.1315     1
2.2159     -2.2159    1.4210     1
2.8952     -1.1992    3.5525     1
6.2675     0.0000     0.0000     1
6.1471     1.2227     2.1315     1
6.2675     0.0000     1.4210     1
6.1471     1.2227     3.5525     1
```

5.7904	2.3985	0.0000	1
5.2112	3.4820	2.1315	1
5.7904	2.3985	1.4210	1
5.2112	3.4820	3.5525	1
4.4318	4.4318	0.0000	1
3.4820	5.2112	2.1315	1
4.4318	4.4318	1.4210	1
3.4820	5.2112	3.5525	1
2.3985	5.7904	0.0000	1
1.2227	6.1471	2.1315	1
2.3985	5.7904	1.4210	1
1.2227	6.1471	3.5525	1
0.0000	6.2675	0.0000	1
-1.2227	6.1471	2.1315	1
0.0000	6.2675	1.4210	1
-1.2227	6.1471	3.5525	1
-2.3985	5.7904	0.0000	1
-3.4820	5.2112	2.1315	1
-2.3985	5.7904	1.4210	1
-3.4820	5.2112	3.5525	1
-4.4318	4.4318	0.0000	1
-5.2112	3.4820	2.1315	1
-4.4318	4.4318	1.4210	1
-5.2112	3.4820	3.5525	1
-5.7904	2.3985	0.0000	1
-6.1471	1.2227	2.1315	1
-5.7904	2.3985	1.4210	1
-6.1471	1.2227	3.5525	1
-6.2675	0.0000	0.0000	1
-6.1471	-1.2227	2.1315	1
-6.2675	0.0000	1.4210	1
-6.1471	-1.2227	3.5525	1
-5.7904	-2.3985	0.0000	1
-5.2112	-3.4820	2.1315	1
-5.7904	-2.3985	1.4210	1
-5.2112	-3.4820	3.5525	1
-4.4318	-4.4318	0.0000	1
-3.4820	-5.2112	2.1315	1
-4.4318	-4.4318	1.4210	1
-3.4820	-5.2112	3.5525	1
-2.3985	-5.7904	0.0000	1
-1.2227	-6.1471	2.1315	1
-2.3985	-5.7904	1.4210	1
-1.2227	-6.1471	3.5525	1
0.0000	-6.2675	0.0000	1
1.2227	-6.1471	2.1315	1
0.0000	-6.2675	1.4210	1
1.2227	-6.1471	3.5525	1
2.3985	-5.7904	0.0000	1
3.4820	-5.2112	2.1315	1
2.3985	-5.7904	1.4210	1
3.4820	-5.2112	3.5525	1

```
4.4318     -4.4318    0.0000     1
5.2112     -3.4820    2.1315     1
4.4318     -4.4318    1.4210     1
5.2112     -3.4820    3.5525     1
5.7904     -2.3985    0.0000     1
6.1471     -1.2227    2.1315     1
5.7904     -2.3985    1.4210     1
6.1471     -1.2227    3.5525     1
%endblock AtomicCoordinatesAndAtomicSpecies
```

Appendix D

Band structure of all DWCNTs considered in this work for energies ±3 eV with respect to the Fermi level. All labels for the X point should be placed at the end of the x axis.

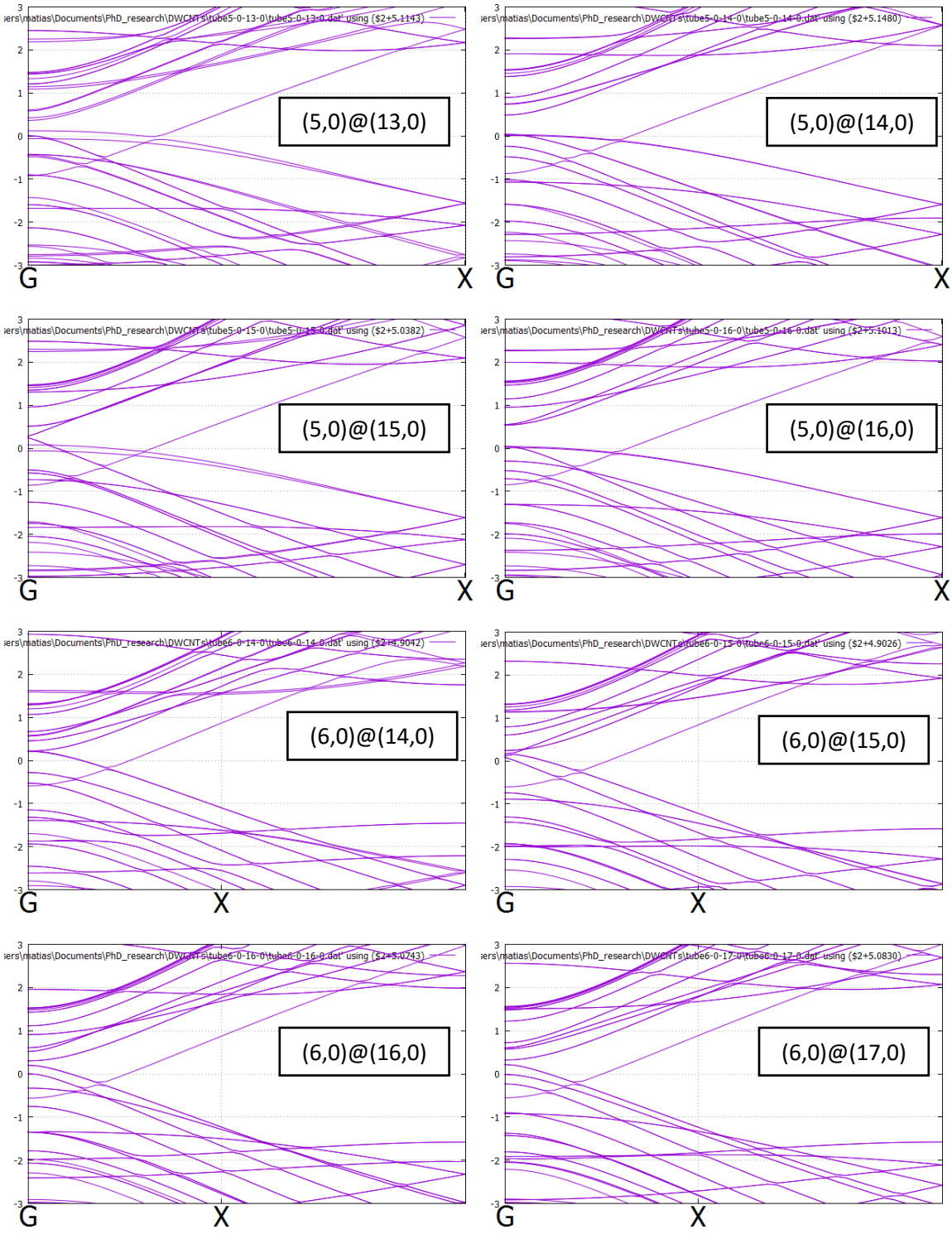

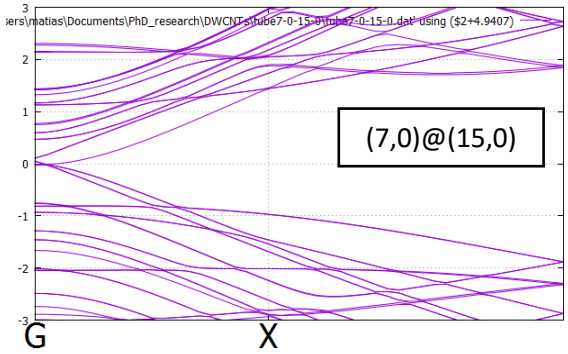
(7,0)@(15,0)
G
X

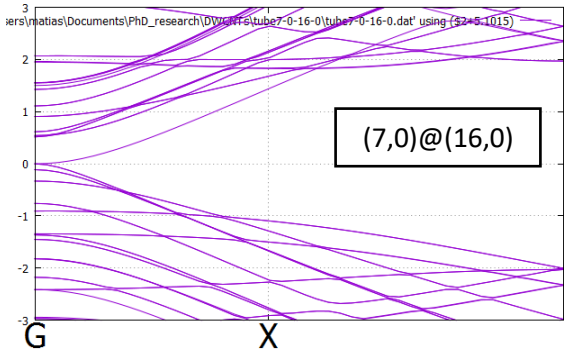
(7,0)@(16,0)
G
X

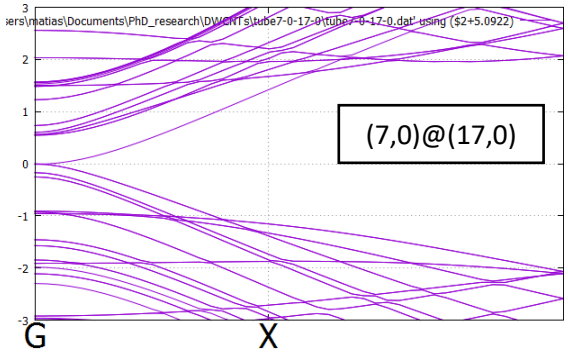
(7,0)@(17,0)
G
X

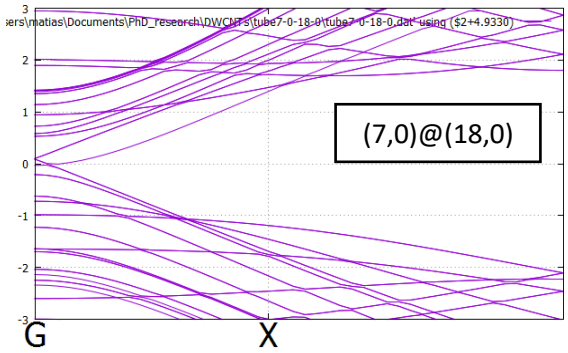
(7,0)@(18,0)
G
X

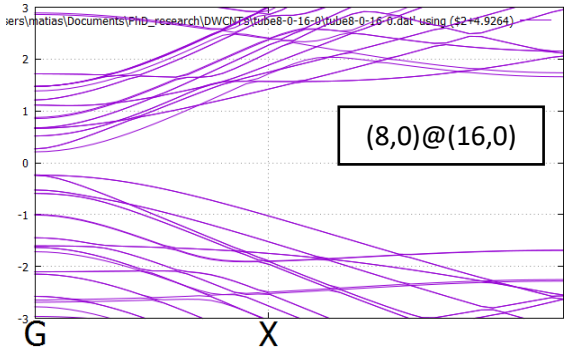
(8,0)@(16,0)
G
X

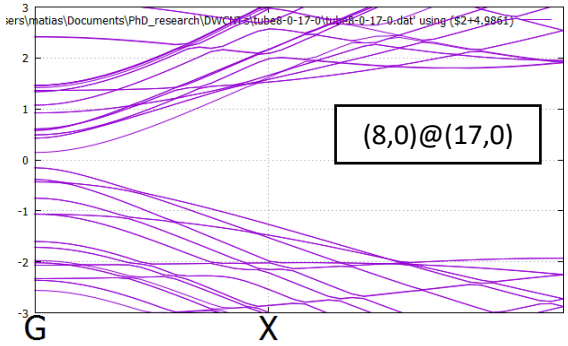
(8,0)@(17,0)
G
X

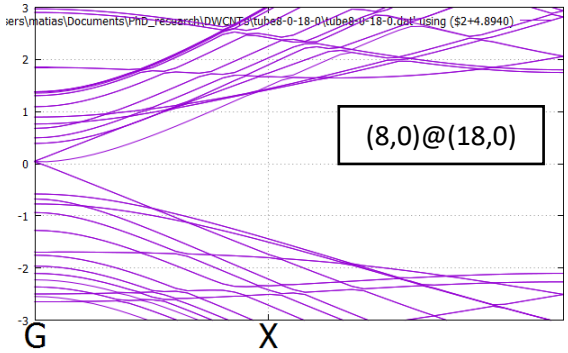
(8,0)@(18,0)
G
X

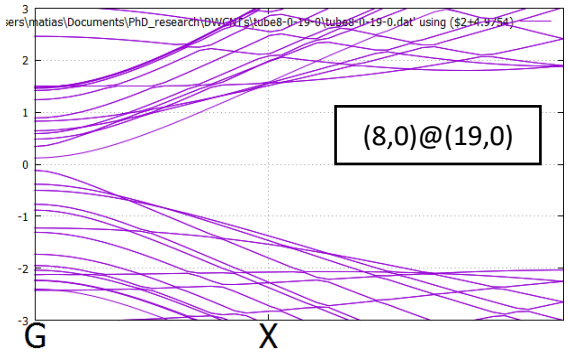
(8,0)@(19,0)
G
X

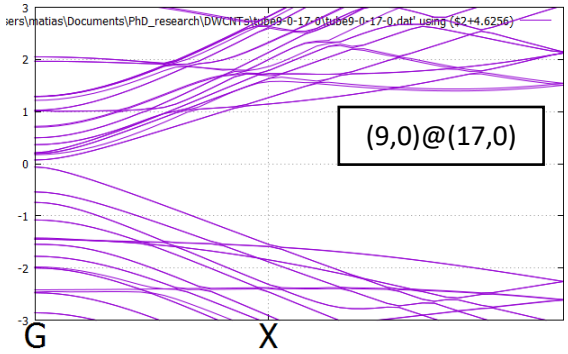
(9,0)@(17,0)
G
X

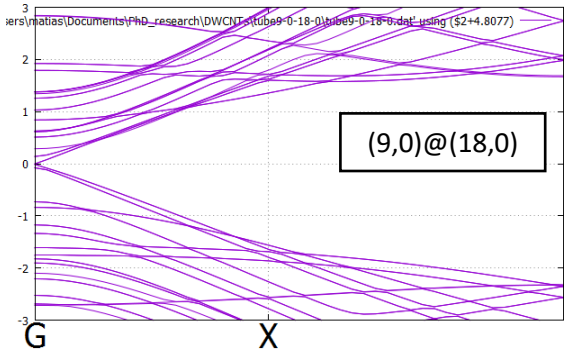
(9,0)@(18,0)
G
X

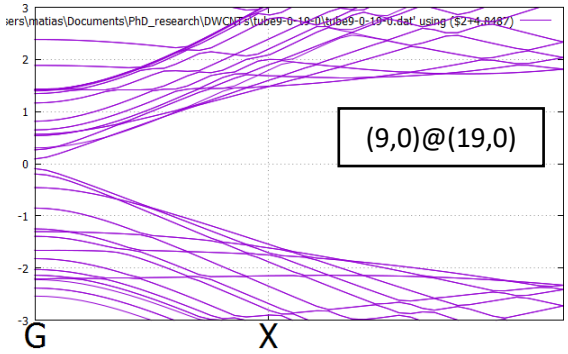
(9,0)@(19,0)
G
X

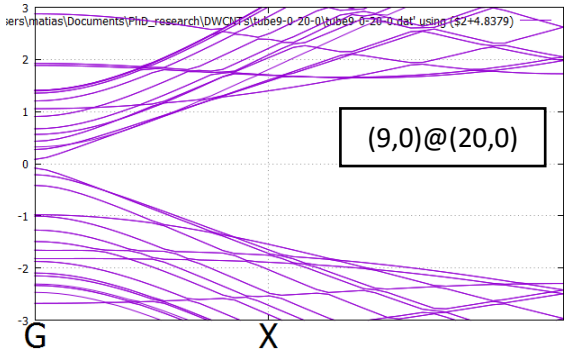
(9,0)@(20,0)
G
X

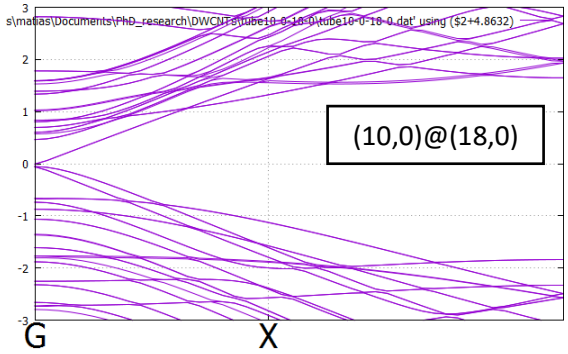
(10,0)@(18,0)
G
X

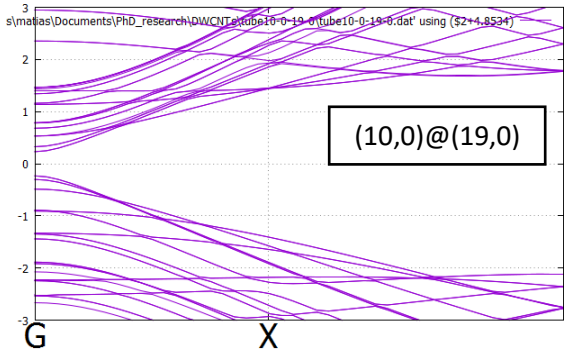
(10,0)@(19,0)
G
X

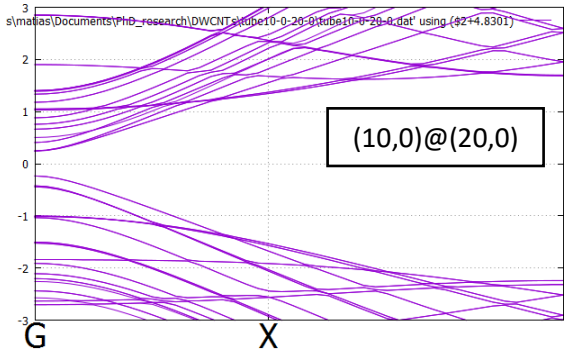
(10,0)@(20,0)
G
X

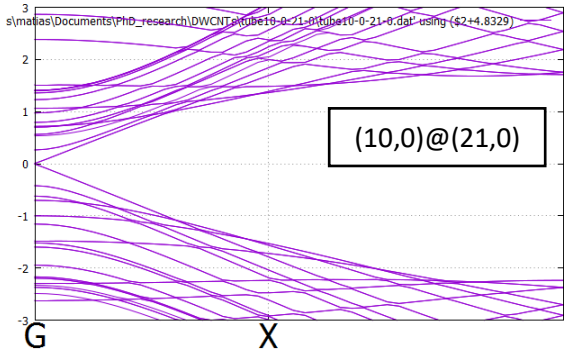
(10,0)@(21,0)
G
X

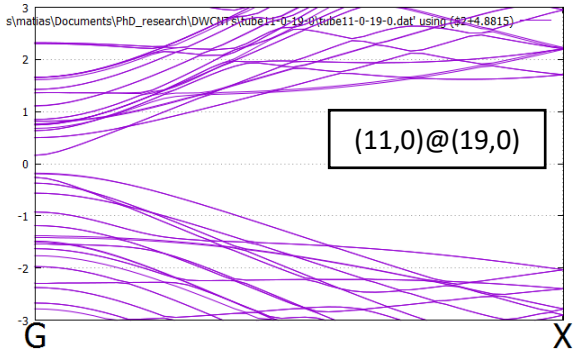
(11,0)@(19,0)
G
X

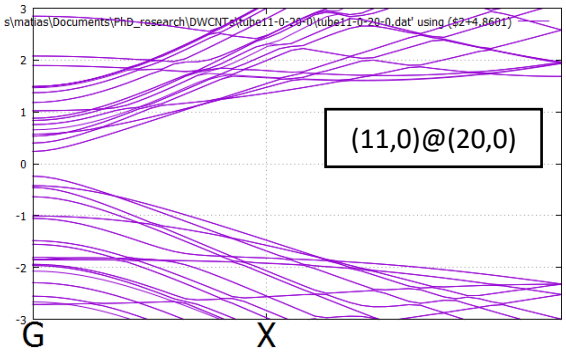
(11,0)@(20,0)
G
X

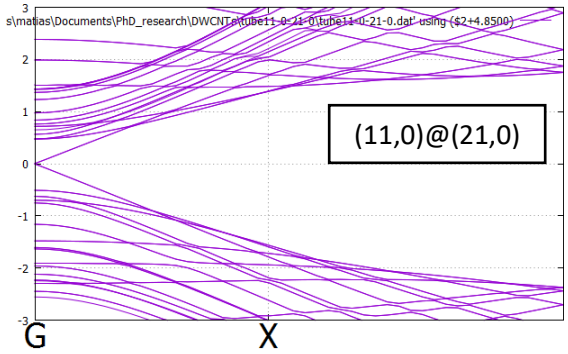
(11,0)@(21,0)
G
X

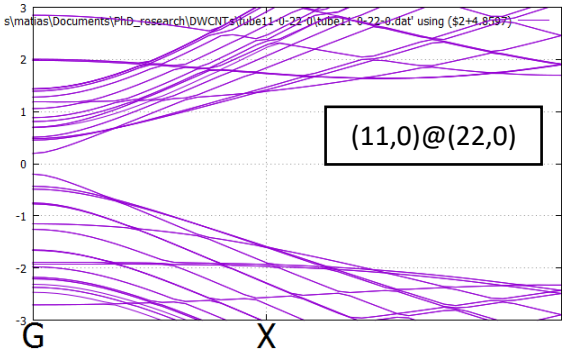
(11,0)@(22,0)
G
X

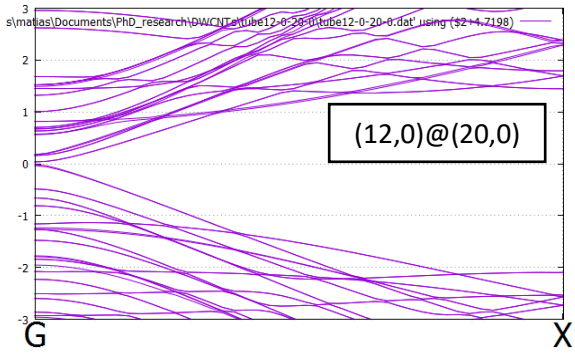
(12,0)@(20,0)
G
X

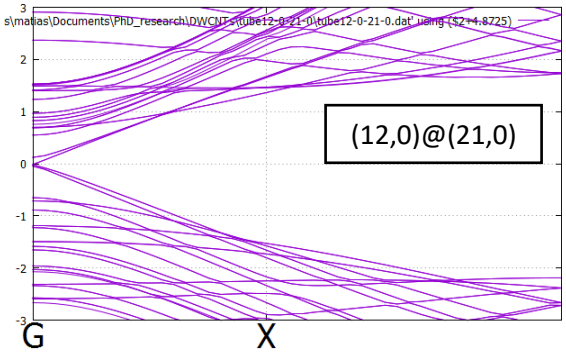
(12,0)@(21,0)
G
X

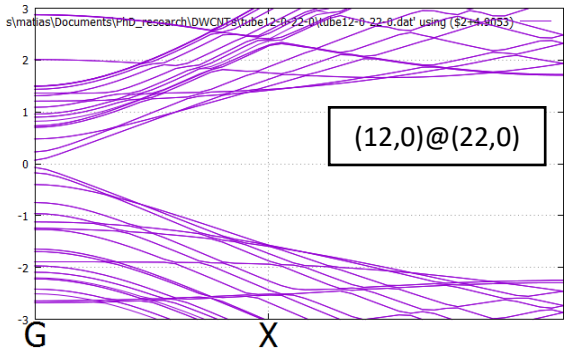
(12,0)@(22,0)
G
X

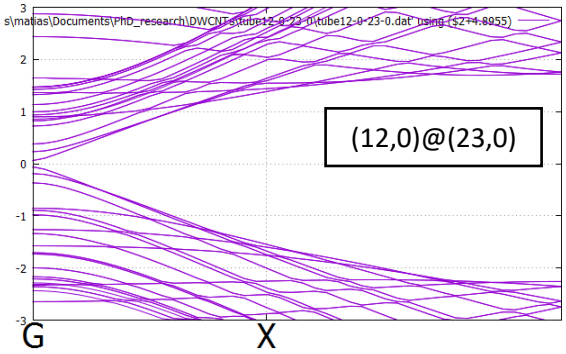
(12,0)@(23,0)
G
X

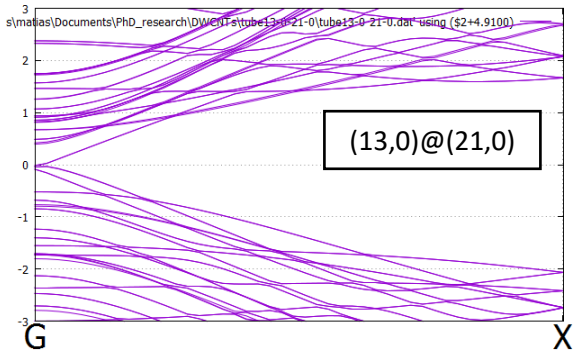
(13,0)@(21,0)
G
X

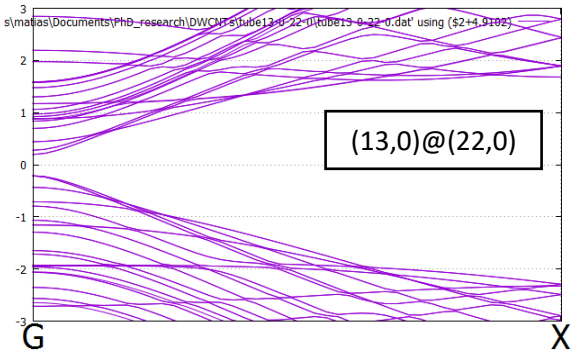
(13,0)@(22,0)
G
X

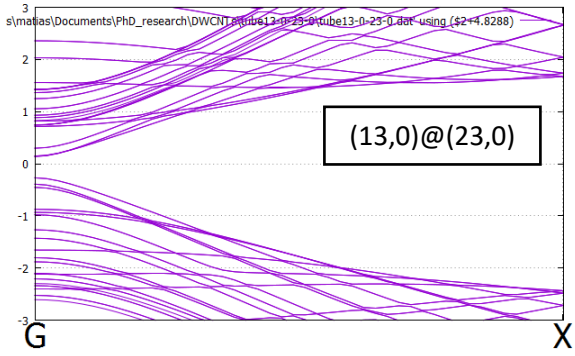
(13,0)@(23,0)
G
X

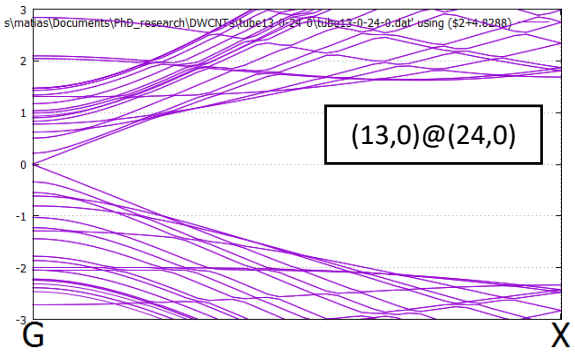
(13,0)@(24,0)
G
X

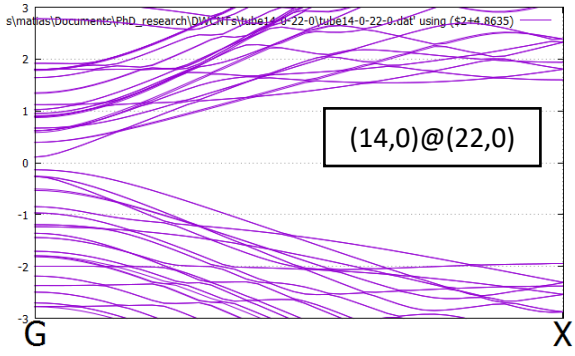
(14,0)@(22,0)
G
X

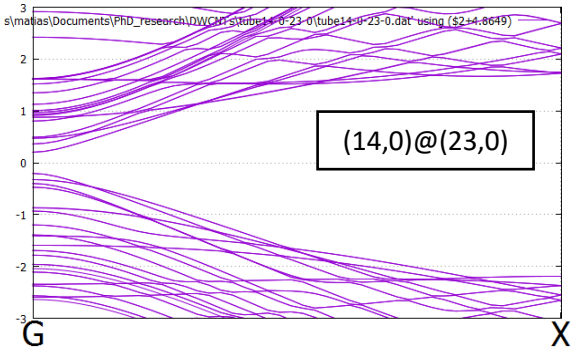
(14,0)@(23,0)
G
X

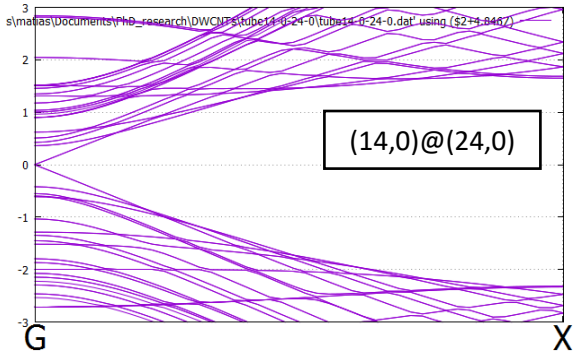
(14,0)@(24,0)
G
X

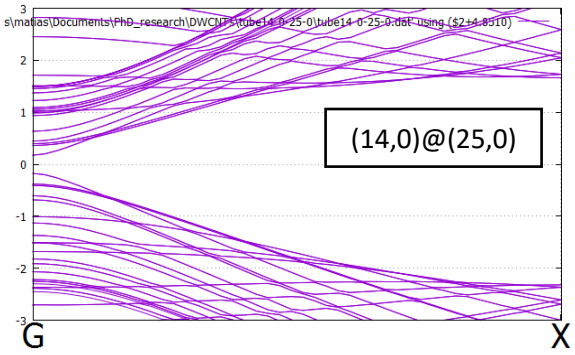
(14,0)@(25,0)
G
X

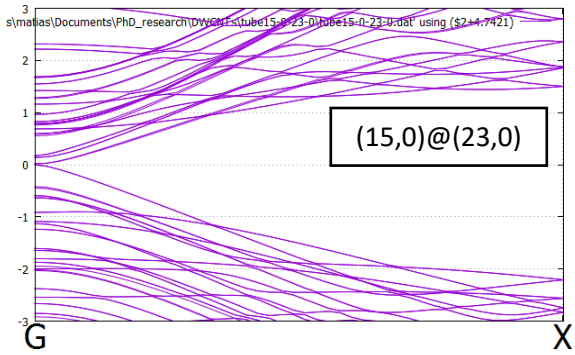
(15,0)@(23,0)
G
X

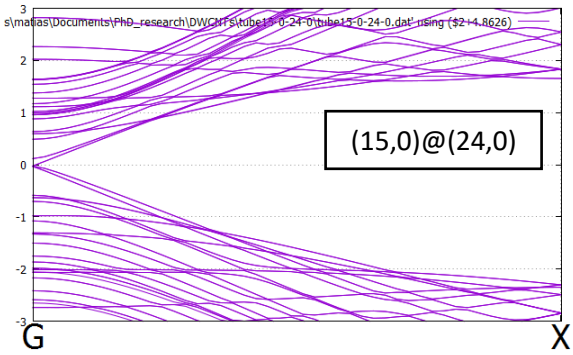
(15,0)@(24,0)
G
X

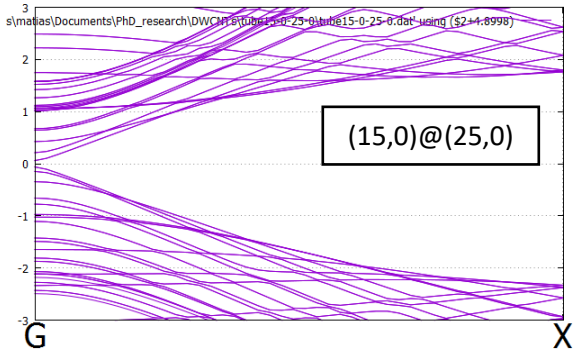
(15,0)@(25,0)
G
X

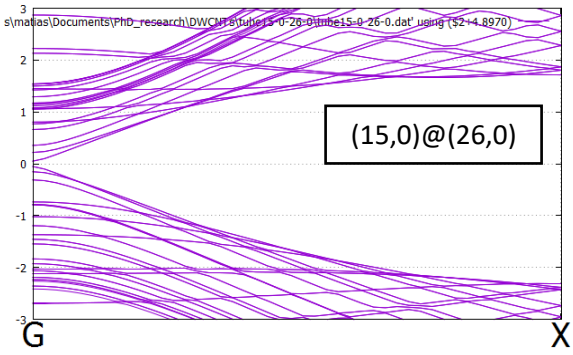
(15,0)@(26,0)
G
X

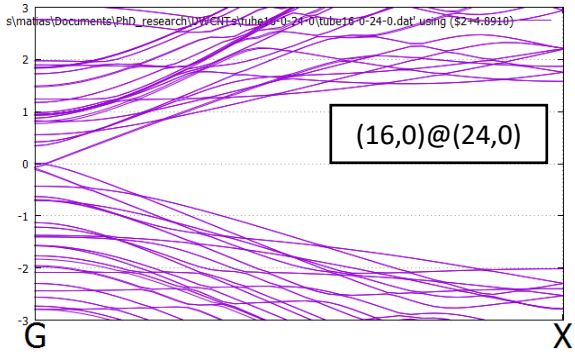
(16,0)@(24,0)
G
X

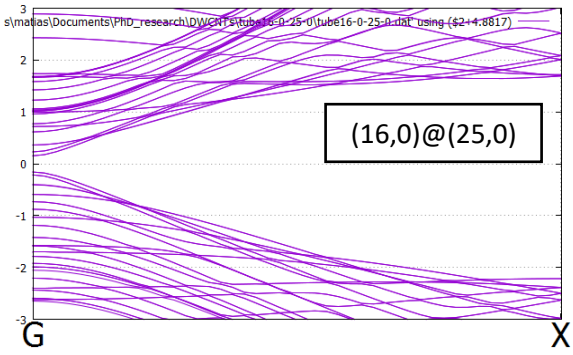
(16,0)@(25,0)
G
X

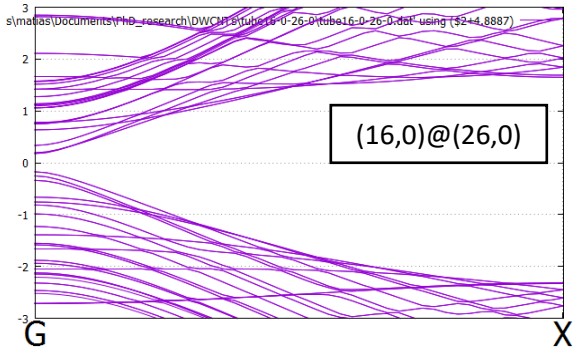
(16,0)@(26,0)
G
X

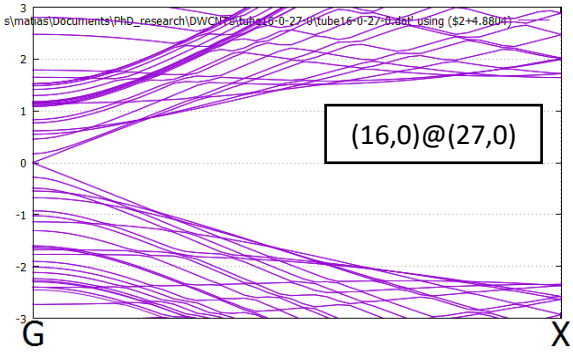
(16,0)@(27,0)
G
X

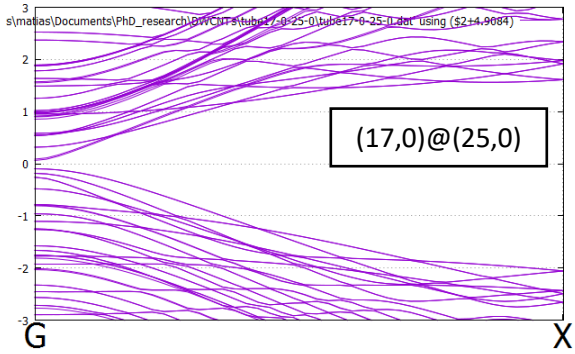
(17,0)@(25,0)
G
X


(17,0)@(26,0)
G
X

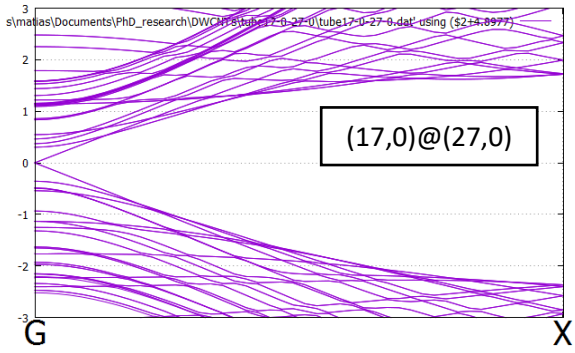
(17,0)@(27,0)
G
X

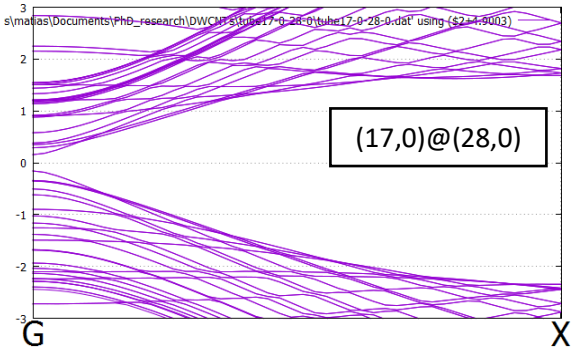
(17,0)@(28,0)
G
X

Appendix E

Input file used for the energy minimization runs in LAMMPS:

```
# Perform energy minimization of CNT system
# << Initialization >>

units metal                         #dist=Ang,energy=eV,force=eV/A
                                    #temp=K,time=picosec,mass=g/mole
atom_style charge                   #stores coords, vel, IDs, types
dimension 3
boundary f f p                      #periodic in z direction only

# << Atom Definition >>
read_data data.txt                  #set coords, IDs, types of atoms
mass 1 12.0107                      #molar mass of C in g/mol
mass 2 126.905                      #molar mass of I in g/mol
group iodine id 129:130


#<< Interactions >>
pair_style hybrid reax/c NULL morse/smooth/linear 8 lj/cut 10
#potential, cutoff
pair_coeff * * reax/c ffield.reax.mattsson C NULL
pair_coeff 2 2 morse/smooth/linear 3.092 1.432 2.578 8
                                    #I J, D0, alpha, r0, cutoff
pair_coeff 1 2 lj/cut 0.0109 3.4 10
                      #I J, eps, sigma, cutoff

fix 1 all qeq/reax 50 0.0 5.0 1.0e-8 reax/c #ID, group-ID,
                                    #qeq/reax, Nevery, cutlo, cuthi
                                    #tol, params
neighbor 3.0 bin                    #extra dist beyond force #cutoff
                                    #dist units; bin style

# << Post-processing >>
#dump data all custom 10 dump.xyz x y z
dump dopants iodine custom 100000 dump_I.xyz x y z
#dump image all image 20 image.*.png type type
#dump movie all movie 1 movie.avi type type

# << Minimization Run >>
minimize 0.0 0.1 10000 100000       #etol ftol maxiter maxeval
min_style cg                        #minimization algorithm
```

Appendix F

Data.txt file used for LAMMPS energy minimization runs:

```
LAMMPS data file for nanotube atom positions
130 atoms
2 atom types
-15 15 xlo xhi
-15 15 ylo yhi
0.0 17.052 zlo zhi
0.0 17.052 zlo zhi

Atoms

  1 1 0 3.45218000 -0.00006930 -0.01672730
  2 1 0 3.18935000 1.31818000 2.11483000
  3 1 0 3.45219000 -0.00006890 1.43797000
  4 1 0 3.18928000 1.31821000 3.56953000
  5 1 0 3.45199000 -0.00006650 4.24639000
  6 1 0 3.18884000 1.31833000 6.37766000
  7 1 0 3.45167000 -0.00006170 5.70109000
  8 1 0 3.18783000 1.31856000 7.83237000
  9 1 0 2.44128000 2.43499000 -0.01673670
 10 1 0 1.32271000 3.18049000 2.11470000
 11 1 0 2.44128000 2.43499000 1.43798000
 12 1 0 1.32270000 3.18062000 3.56944000
 13 1 0 2.44129000 2.43518000 4.24622000
 14 1 0 1.32271000 3.18118000 6.37766000
 15 1 0 2.44118000 2.43547000 5.70094000
 16 1 0 1.32246000 3.18174000 7.83240000
 17 1 0 0.00415458 3.44202000 -0.01675370
 18 1 0 -1.31435000 3.18039000 2.11472000
 19 1 0 0.00416066 3.44201000 1.43800000
 20 1 0 -1.31432000 3.18044000 3.56946000
 21 1 0 0.00417971 3.44218000 4.24617000
 22 1 0 -1.31432000 3.18070000 6.37772000
 23 1 0 0.00413594 3.44242000 5.70093000
 24 1 0 -1.31441000 3.18091000 7.83247000
 25 1 0 -2.43294000 2.43493000 -0.01674540
 26 1 0 -3.18112000 1.31818000 2.11479000
 27 1 0 -2.43294000 2.43493000 1.43798000
 28 1 0 -3.18104000 1.31819000 3.56949000
 29 1 0 -2.43285000 2.43495000 4.24626000
 30 1 0 -3.18083000 1.31820000 6.37780000
 31 1 0 -2.43276000 2.43502000 5.70099000
 32 1 0 -3.18074000 1.31823000 7.83250000
 33 1 0 -3.44409000 -0.00007210 -0.01673150
 34 1 0 -3.18118000 -1.31833000 2.11479000
 35 1 0 -3.44409000 -0.00007200 1.43796000
 36 1 0 -3.18111000 -1.31835000 3.56949000
```

```
37 1 0 -3.44393000 -0.00007260 4.24632000
38 1 0 -3.18089000 -1.31836000 6.37780000
39 1 0 -3.44379000 -0.00007290 5.70101000
40 1 0 -3.18081000 -1.31839000 7.83250000
41 1 0 -2.43303000 -2.43511000 -0.01674500
42 1 0 -1.31445000 -3.18056000 2.11472000
43 1 0 -2.43303000 -2.43511000 1.43798000
44 1 0 -1.31441000 -3.18062000 3.56946000
45 1 0 -2.43294000 -2.43513000 4.24626000
46 1 0 -1.31442000 -3.18088000 6.37772000
47 1 0 -2.43286000 -2.43521000 5.70099000
48 1 0 -1.31451000 -3.18109000 7.83247000
49 1 0 0.00407031 -3.44216000 -0.01675360
50 1 0 1.32262000 -3.18060000 2.11470000
51 1 0 0.00407624 -3.44215000 1.43800000
52 1 0 1.32261000 -3.18073000 3.56944000
53 1 0 0.00409327 -3.44233000 4.24617000
54 1 0 1.32261000 -3.18128000 6.37766000
55 1 0 0.00404588 -3.44257000 5.70093000
56 1 0 1.32235000 -3.18184000 7.83240000
57 1 0 2.44118000 -2.43510000 -0.01673700
58 1 0 3.18928000 -1.31830000 2.11483000
59 1 0 2.44119000 -2.43509000 1.43798000
60 1 0 3.18921000 -1.31833000 3.56954000
61 1 0 2.44119000 -2.43528000 4.24622000
62 1 0 3.18876000 -1.31844000 6.37766000
63 1 0 2.44107000 -2.43557000 5.70094000
64 1 0 3.18773000 -1.31865000 7.83237000
65 1 0 3.44853000 -0.00005790 8.50923000
66 1 0 3.18771000 1.31855000 10.64090000
67 1 0 3.44840000 -0.00006080 9.96402000
68 1 0 3.18876000 1.31833000 12.09560000
69 1 0 3.45161000 -0.00006410 12.77220000
70 1 0 3.18925000 1.31822000 14.90370000
71 1 0 3.45195000 -0.00006780 14.22690000
72 1 0 3.18934000 1.31818000 16.35840000
73 1 0 2.44084000 2.43611000 8.50928000
74 1 0 1.32243000 3.18178000 10.64080000
75 1 0 2.44080000 2.43614000 9.96395000
76 1 0 1.32269000 3.18122000 12.09560000
77 1 0 2.44114000 2.43551000 12.77230000
78 1 0 1.32269000 3.18065000 14.90380000
79 1 0 2.44127000 2.43520000 14.22700000
80 1 0 1.32271000 3.18050000 16.35850000
81 1 0 0.00395003 3.44310000 8.50924000
82 1 0 -1.31443000 3.18094000 10.64080000
83 1 0 0.00392863 3.44313000 9.96399000
84 1 0 -1.31434000 3.18073000 12.09550000
85 1 0 0.00411117 3.44246000 12.77230000
86 1 0 -1.31433000 3.18046000 14.90380000
87 1 0 0.00416683 3.44221000 14.22710000
88 1 0 -1.31436000 3.18039000 16.35850000
```

```
 89 1 0 -2.43276000 2.43515000 8.50925000
 90 1 0 -3.18074000 1.31823000 10.64070000
 91 1 0 -2.43277000 2.43516000 9.96398000
 92 1 0 -3.18082000 1.31820000 12.09540000
 93 1 0 -2.43277000 2.43504000 12.77220000
 94 1 0 -3.18103000 1.31819000 14.90370000
 95 1 0 -2.43285000 2.43496000 14.22700000
 96 1 0 -3.18112000 1.31818000 16.35840000
 97 1 0 -3.44359000 -0.00007340 8.50927000
 98 1 0 -3.18081000 -1.31839000 10.64070000
 99 1 0 -3.44359000 -0.00007340 9.96396000
100 1 0 -3.18089000 -1.31836000 12.09540000
101 1 0 -3.44378000 -0.00007310 12.77220000
102 1 0 -3.18110000 -1.31835000 14.90370000
103 1 0 -3.44392000 -0.00007260 14.22690000
104 1 0 -3.18118000 -1.31833000 16.35840000
105 1 0 -2.43286000 -2.43533000 8.50925000
106 1 0 -1.31453000 -3.18112000 10.64080000
107 1 0 -2.43287000 -2.43534000 9.96398000
108 1 0 -1.31444000 -3.18091000 12.09550000
109 1 0 -2.43286000 -2.43522000 12.77220000
110 1 0 -1.31442000 -3.18063000 14.90380000
111 1 0 -2.43294000 -2.43514000 14.22700000
112 1 0 -1.31445000 -3.18057000 16.35850000
113 1 0 0.00385741 -3.44325000 8.50924000
114 1 0 1.32233000 -3.18188000 10.64080000
115 1 0 0.00383656 -3.44327000 9.96399000
116 1 0 1.32259000 -3.18133000 12.09560000
117 1 0 0.00402216 -3.44261000 12.77230000
118 1 0 1.32259000 -3.18076000 14.90380000
119 1 0 0.00408094 -3.44236000 14.22710000
120 1 0 1.32262000 -3.18061000 16.35850000
121 1 0 2.44073000 -2.43619000 8.50928000
122 1 0 3.18761000 -1.31865000 10.64090000
123 1 0 2.44069000 -2.43622000 9.96395000
124 1 0 3.18868000 -1.31844000 12.09560000
125 1 0 2.44103000 -2.43560000 12.77230000
126 1 0 3.18918000 -1.31834000 14.90370000
127 1 0 2.44118000 -2.43530000 14.22700000
128 1 0 3.18927000 -1.31831000 16.35840000
129 2 0 0.76322499 7.16231432 6.02665706
130 2 0 1.31809012 8.57458141 8.12563928
```